Karlsruhe Institute of Technology

NLO QCD corrections to WH + jet production at the LHC

Diplomarbeit
von

Robin Roth

An der Fakultät für Physik
Institut für Theoretische Physik

Referent: Prof. Dr. D. Zeppenfeld
Korreferent: Prof. Dr. M. Steinhauser

Bearbeitungszeit: 31. Oktober 2012 – 30. Oktober 2013

Ich versichere, dass ich diese Arbeit selbstständig verfasst und ausschließlich die angegebenen Hilfsmittel verwendet habe.

Robin Roth
Karlsruhe, den 30. Oktober 2013

Als Diplomarbeit anerkannt.

Prof. Dr. D. Zeppenfeld
Karlsruhe, den 30. Oktober 2013

CONTENTS

CHAPTER 1

INTRODUCTION

Particle physics studies the fundamental building blocks of the universe and their interactions on very small scales. The Standard Model (SM) of particle physics is a relativistic quantum field theory, which was developed in the 1960s and 70s. Since then it has been successfully used to predict both precision experiment outcomes as well as new particles. Recently, a new particle was discovered. The resonance observed so far resembles the SM Higgs boson, however the measurements of its properties still have to be completed. The particle was detected by ATLAS and CMS [1, 2], two experiments situated at the Large Hadron Collider (LHC) at CERN, Geneva. The LHC is the latest in a series of collider experiments. It was built to search for new particles and probe our understanding of particle physics. It was designed not only to search for the Higgs boson, but also to study theories going beyond the SM. The discovery of the Higgs boson is the verge to a new generation of SM precision measurements and particles at the TeV scale.

Despite the SM success, we now know that the SM is not able to describe all phenomena. There are issues related to the theoretical construction of the SM. In the SM (nearly) all masses are free parameters and they stretch over several orders of magnitude. The traditional SM does not include neutrino masses which must be non-zero due to the measurement of neutrino oscillations. Several experiments are trying to measure the neutrino mass, but so far only limits were imposed. While it is possible to add a massive neutrino sector to the SM, their masses have to be below 1 eV. There is no explanation of the mass difference between charged leptons and neutrinos within the SM. On the other hand, the top quark, the heaviest of the elementary particles, has a mass which is six orders of magnitude bigger. Currently, there is not a satisfactory explanation of the broad mass spectrum covered in the SM.

Some open problems of the SM are related to observations in astronomy. Firstly, gravity is not described by the SM. The theory of general relativity provides a well proven formulation of gravity, but no successful formulation of a combined theory of general relativity and the SM has been achieved.

Astronomical observations show two interesting features that have so far not been explained: Dark Matter and Dark Energy. The movement of stars in galaxies can not be explained just based on the visible, baryonic matter. This can be solved by assuming additional (dark) matter being distributed around the galaxy, but the SM does not provide a natural candidate

for dark matter. Dark Energy is related to the accelerating expansion of the visible universe, which is unexpected and not fully understood.

The early development of the universe is described by Big Bang nucleosynthesis. This theory can not explain why the unbalance between matter and anti-matter is as large as observed in the universe today. The SM has mechanisms violating $\mathcal{CP}$, but they can not explain the observed difference.

Because the SM does not describe gravity, it can at most be valid up to the Planck scale of about $10 \cdot 10^{19}\,\mathrm{GeV}$. The SM then is assumed to be a low-energy effective theory of an unknown theory at the Planck scale. When calculating higher-order corrections to masses of particles, the corrections are of the same order as the scale of the theory. Because of the observed mass, those corrections of a high-energy theory must be small. While the other particles are protected from large corrections by mechanism like custodial symmetries, there is no such mechanism for the Higgs boson. If there is no new theory up to the Planck scale, fine-tuning of the theoretical parameters would be required to explain the observed mass. This issue is called the *hierarchy problem*.

While the SM has proven successful in describing many particle physics phenomena to high precision, hints on physics beyond the SM were recently found in precision experiments. The g-factor of the muon, which relates spin and magnetic moment, is the most precise measured physical quantity. While there are calculations with sufficient accuracy, they show a deviation from the measured value [3].

The SM is based on the gauge group $\mathrm{SU(3)_C} \times \mathrm{SU(2)_L} \times \mathrm{U(1)_Y}$. The factor $\mathrm{SU(2)_L} \times \mathrm{U(1)_Y}$ describes the electroweak (EW) sector. The weak force is mediated by W and Z boson. The W boson is among others responsible for radioactive β-decay.

$\mathrm{SU(2)_L} \times \mathrm{U(1)_Y}$ is broken via spontaneous symmetry breaking by the Higgs mechanism to the group $\mathrm{U(1)_{em}}$. This group describes quantum electrodynamics (QED) – the interaction of electrically charged particles via photons. The Higgs mechanism generates the masses of the gauge bosons and fermions.

The group $\mathrm{SU(3)_C}$ describes quantum chromodynamics (QCD), which is the theory of the strong interaction. It acts on particles with color charge, which are quarks and gluons. The two sectors of the SM are often referred to by their coupling constants: α for the EW sector and α_s for the strong sector.

Despite the great success of calculations performed in lattice QCD in the last decades, predictions of the SM are mostly calculated using perturbation theory. This means that observables are expanded as a series in coupling constants. The first term of such an expansion is called leading order (LO), followed by the next-to-leading order (NLO) and the next-to-next-to-leading order (NNLO). Because α_s is an order of magnitude larger than α, this expansion is often only done in α_s. A calculation including NLO terms in α_s is called NLO QCD.

Except for direct searches for new particles or processes, possible theories beyond the SM can be studied by comparing the SM prediction to data and then setting limits on general extensions of the SM. For the newly discovered Higgs boson, this means to investigate the different production and decay mechanisms.

The main production mechanisms for the Higgs boson in the SM are shown in chapter 1. The production mode with the largest cross section is called Gluon Fusion. There two gluons produce the Higgs boson via a fermion loop. Another interesting production mechanism is

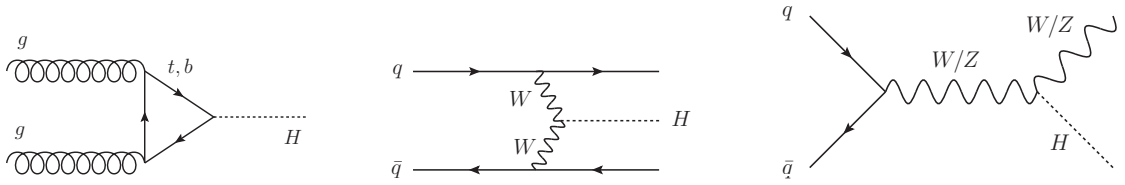

(a) Gluon Fusion **(b)** Vector Boson Fusion **(c)** Higgsstrahlung (VH)

Figure 1.1: Feynman diagrams for the three most important Higgs boson production channels are shown. In this thesis the production of WH and WHj is calculated at NLO QCD.

Vector Boson Fusion, which has the second highest cross section and a good signal/background ratio. The Higgs boson can also be produced in association with a weak boson or top quarks. The production with a weak boson (VH) is also called Higgsstrahlung, because the corresponding Feynman diagram has the Higgs boson "radiating" off a W or Z.

This set of production mechanisms is interesting, because they allow to measure the couplings of the Higgs boson to different SM particles. In the SM, these couplings are not independent but fixed by a small number of parameters, so possible inconsistencies can be studied with high precision.

The Higgs boson is unstable and decays immediately. There are many possible decay channels. Detecting a Higgs boson through one of the possible decays is challenging, because for each of them there are other SM processes yielding the same final state. These are called background processes and need to be known accurately to allow the extraction of the signal. Thus, NLO QCD corrections are important for both background and signal processes.

The LHC experiments searched for WH production considering the decay of the H to $b\bar{b}$ [4, 5] and WW [6]. In these channels there is no established signal, but the measurement is still consistent with the SM prediction. WH production was also used in searches for physics beyond the Standard Model [7].

The NLO QCD corrections for WH production are large and phase space dependent, demonstrating the importance of NLO calculations. A large fraction of the WH events comes accompanied of additional jets. In this thesis, WHj production at NLO QCD is computed. In WH production at NLO, at most one jet computed at LO is included, so WHj production at NLO can be used to estimate higher order corrections to the WH production mechanism. Leptonic decays of the W are included as well as decays of the Higgs boson (previous results involved on-shell W). As a by product also the NLO corrections of W, WH and WJ production are calculated. This thesis is organized as follows:

In chapter 2, the theoretical background will be discussed. A short introduction to the SM and the physics of hadron colliders is given. The Higgs boson is discussed in more detail, including the different production and decay modes. This leads to the introduction of the WH production process with its features. It follows a description of the fundamental techniques used for the numerical calculation: Monte Carlo integration with importance sampling and automatic optimization using VEGAS. The NLO QCD calculation requires special treatment to allow numerical integration. The Catani Seymour method is applied for that purpose.

Based on the methods discussed, the calculation of WH and WHj is described in chapter 3. The calculation is implemented in the program VBFNLO, which is introduced. The different parts of the calculation are discussed, starting from the phase space integration, leading to

the matrix element at LO and NLO QCD. Two special aspects of the calculation are discussed in more detail: the treatment of the CKM matrix and the choice of flavour scheme.

Chapter 4 describes the checks performed to guarantee the correctness of the calculation. These checks start with the LO matrix elements and the LO cross section, but also cover the NLO QCD correction. This includes the virtual contributions, which were checked using internal consistency checks as well as comparisons with external codes, and subtraction terms which are constructed using the Catani Seymour method. Finally, the NLO cross section is compared with existing calculations for WH and Wj, as well as a previous calculation of WHj for on-shell W and Higgs boson.

Using the checked implementation of WH(j), the phenomenology of this process is studied in chapter 5. This study discusses the effects and properties of the NLO calculation, which has an influence on the scale dependence of the process. A common analysis technique requiring a boosted W and/or Higgs boson is studied and the effect of anomalous couplings on this process is discussed.

In the final chapter 6, conclusions are given as well as an outlook on further related calculations and possible studies.

CHAPTER 2

THEORETICAL ESSENTIALS

In this chapter, a brief introduction to several essential theoretical aspects is given. The Standard Model is presented in section 2.1. Anomalous couplings entering in a general extension of the Standard Model are discussed in section 2.2. The fundamental building blocks of a next-to-leading order calculation are introduced in section 2.3. Section 2.4 describes particle colliders and the general approach used to describe hadronic collisions. Production and Decay of the Higgs boson and the production process used in this thesis are introduced in section 2.5. Section 2.6 describes the method used for numerical integration.

2.1. The Standard Model

The Standard Model (SM) is a relativistic quantum field theory. Since its development in the 1970s, it has been very successful in describing particle physics, both in new phenomena as well as in precision measurements. The SM consists of two sectors. The electroweak sector covers the electromagnetic interaction, mediated by the photon, and weak interaction, mediated by the W and Z boson. The strong sector is described by quantum chromodynamics (QCD), where the gluon mediates the strong force. These interactions can be described by gauge theories which are identified with symmetry groups. The overall gauge group of the SM is

$$\mathrm{SU(3)_C} \times \mathrm{SU(2)_L} \times \mathrm{U(1)_Y}. \tag{2.1}$$

The group $\mathrm{SU(3)_C}$ corresponds to QCD, while the group $\mathrm{SU(2)_L} \times \mathrm{U(1)_Y}$ describes the EW sector, both of them will be described in the following. This thesis will closely follow the notation and convention of Ref. [8], where a more detailed introduction to quantum field theories can be found.

2.1.1. Quantum chromodynamics

The Lagrangian of quantum chromodynamics is

$$\mathcal{L} = \sum_{\text{quark flavours}} \Psi_i \left(i \not{D}_{ij} - m_q \delta_{ij} \right) \Psi_j - \frac{1}{4} \left(G^a_{\mu\nu} \right)^2 - \frac{1}{2\xi} \left(\partial^\mu A^a_\mu \right)^2 + \bar{c}^a \left(-\partial^\mu D^{ac}_\mu \right) c^c. \tag{2.2}$$

QCD is described by the group $\mathrm{SU(3)_C}$. The quark fields Ψ_i transform under the fundamental representation of $\mathrm{SU(3)_C}$ and the gauge field of this theory, the gluon field G^a_μ, is in the adjoint representation. This gives 3 quark colors and 8 gluons. The gluon field strength tensor is

$$G^a_{\mu\nu} = \partial_\mu G^a_\nu - \partial_\nu G^a_\mu + g_s f^{abc} G^b_\mu G^c_\nu, \tag{2.3}$$

with the strong coupling g_s and the structure constants f^{abc} of $\mathrm{SU(3)_C}$. Using the Faddeev-Popov method for quantization gives additional ghost fields, called c^a. Those are anticommuting fields in the adjoint representation and are introduced to formulate a consistent Lagrangian, where unphysical degrees of freedom are removed.

The strong coupling is in general expressed in terms of $\alpha_\mathrm{s} \equiv {g_s^2}/{4\pi}$. It is scale dependent and the running used for the calculation is given by the two-loop level as

$$\alpha_\mathrm{s}(Q^2) = \frac{4\pi}{b_0}\left[\frac{1}{\ln(Q^2/\Lambda^2_\mathrm{QCD})} - \frac{b_1}{b_0^2}\frac{\ln\ln(Q^2/\Lambda^2_\mathrm{QCD})}{(\ln(Q^2/\Lambda^2_\mathrm{QCD}))^2}\right], \tag{2.4}$$

with $b_0 = 11 - {2}/{3}\, n_\mathrm{f}$, $b_1 = 51 - {19}/{3}\, n_\mathrm{f}$ and Λ_QCD dependent of the order of perturbation theory and fit used, in this calculation $\Lambda_\mathrm{QCD} = 226\,\mathrm{GeV}$. Instead of using Λ_QCD, the running could also be expressed based on α_s at a fixed scale μ. The one-loop running can be written as

$$\alpha_\mathrm{s}(Q^2) = \frac{\alpha_\mathrm{s}(\mu^2)}{1 + \frac{\alpha_\mathrm{s}(\mu^2)}{4\pi} b_0 \ln\left(\frac{Q^2}{\mu^2}\right)}. \tag{2.5}$$

This scale dependence is the reason for two fundamental properties of QCD: asymptotic freedom and confinement. For $Q^2 \to \infty$, the coupling α_s vanishes, which means that at large scales, the coupling is small and the interaction between quarks and gluons is weak. In that energy regime they behave like free particles. This feature is called "asymptotic freedom". Thus, at high energies the QCD interaction can be described well using perturbation theory.

On the opposite side of the energy spectrum for $Q^2 \to \Lambda_\mathrm{QCD}$, the coupling diverges. This makes bound states (corresponding to the low scale) very stable. When trying to separate two quarks, the strong potential will build up enough energy to produce a quark-antiquark pair and, thereby, two bound states instead of giving up the first binding.

2.1.2. The Electroweak sector

The EW sector covers electromagnetic and weak interactions. The theory was developed by Glashow, Salam and Weinberg (and is therefore called GWS-theory) in Refs. [9, 10, 11].

It is described by the group $\mathrm{SU(2)_L} \times \mathrm{U(1)_Y}$. There are gauge fields corresponding to both groups,

$$\mathrm{SU(2)_L}: \quad W^a_\mu\,, \quad a = 1, 2, 3, \tag{2.6}$$

$$\mathrm{U(1)_Y}: \quad B_\mu\,. \tag{2.7}$$

Using these gauge fields, the interaction Lagrangian can be constructed. To do so, the covariant derivative is used, which includes the couplings g (and g') corresponding to $\mathrm{SU(2)_L}$ (and $\mathrm{U(1)_Y}$) and $T^a = \frac{\sigma^a}{2}$, with the Pauli matrices σ^a, which are the generators of SU(2). The covariant derivative is given by

$$D_\mu = \partial_\mu - igW^a_\mu T^a - ig' Y B_\mu\,. \tag{2.8}$$

The coupling of gauge fields (and thus the particles corresponding to them) to fermions can be written in a compact form using the covariant derivative as

$$\mathcal{L} = \sum_{L=E_\mathrm{L},Q_\mathrm{L}} i\overline{L}\not{D}L + \sum_{R=e_\mathrm{R},u_\mathrm{R},d_\mathrm{R}} i\overline{R}\not{D}R\,. \tag{2.9}$$

Left- and right-handed components of the fermion fields transform under different representations of $\mathrm{SU}(2)_\mathrm{L}$. Right-handed fields are singlets: $e_\mathrm{R}, u_\mathrm{R}, d_\mathrm{R}$. Left-handed fields transform as doublets

$$E_\mathrm{L} = \begin{pmatrix} \nu_e \\ e^- \end{pmatrix}_\mathrm{L}, \quad Q_\mathrm{L} = \begin{pmatrix} u \\ d \end{pmatrix}_\mathrm{L}. \tag{2.10}$$

Only doublets and, thus, the left-handed fields can couple to the $\mathrm{SU}(2)_\mathrm{L}$ gauge bosons. The Lagrangian given in equation (2.9) can be written in several forms. A convenient way is to give the interactions in terms of the mass eigenstates. In this way, the couplings of fermions to the W bosons can be written as

$$\mathcal{L} = g\left(W^+_\mu J^{\mu+}_W + W^-_\mu J^{\mu-}_W\right), \tag{2.11}$$

$$\text{where } J^{\mu+}_W = \frac{1}{\sqrt{2}}\overline{\nu}_\mathrm{L}\gamma^\mu e_\mathrm{L} + \frac{1}{\sqrt{2}}\overline{u}_\mathrm{L}\gamma^\mu d_\mathrm{L}\,, \tag{2.12}$$

$$J^{\mu-}_W = \frac{1}{\sqrt{2}}\overline{e}_\mathrm{L}\gamma^\mu \nu_\mathrm{L} + \frac{1}{\sqrt{2}}\overline{d}_\mathrm{L}\gamma^\mu u_\mathrm{L}\,. \tag{2.13}$$

2.1.2.1. Higgs Mechanism

Using the fermion fields, the usual mass term would be of the form $m\left(\overline{L}R + \overline{R}L\right)$. However, since L and R are in different representations, there is no direct mass term compatible with the symmetries. Nevertheless mass terms can be generated using spontaneous symmetry breaking. To accomplish this, a new $\mathrm{SU}(2)_\mathrm{L}$ doublet is introduced. Additionally, a potential is added to the Lagrangian which leads to a non-zero vacuum expectation value (vev) of that new doublet,

$$\mathcal{L} = |D_\mu\phi|^2 + \mu^2\phi^\dagger\phi - \lambda\left(\phi^\dagger\phi\right)^2\,. \tag{2.14}$$

For $\mu^2, \lambda > 0$, this potential has a Mexican hat shape and, therefore, a minimum that leads to a non-zero vev with absolute value

$$|\phi_0| = \sqrt{\frac{\mu^2}{2\lambda}} \equiv \frac{v}{\sqrt{2}}\,. \tag{2.15}$$

This vev breaks the $\mathrm{SU}(2)_\mathrm{L} \times \mathrm{U}(1)_\mathrm{Y}$ symmetry down to a $\mathrm{U}(1)_\mathrm{em}$ symmetry. The remaining symmetry leaves an (unphysical) freedom of choice for the minimum of the potential. The conventional choice is to have the vev in the second component. This breaking of $\mathrm{SU}(2)_\mathrm{L}$ fixes the left handed fields and the convention to have a real vev in the second component is implied in equation (2.10). Particles in this doublet can be understood as excitations around the minimum. There are four possible directions. Three of them correspond to Goldstone bosons which are absorbed by the masses of the W and Z bosons. The other direction can be associated with a new physical particle. This mechanism was developed by Brout, Englert and Higgs [12, 13, 14]. The new particle predicted is usually named after the latter and thus called Higgs boson.

The Higgs field h is a scalar field and with the vev, the doublet is

$$\phi(x) = \frac{1}{\sqrt{2}} \begin{pmatrix} 0 \\ v + h(x) \end{pmatrix} . \tag{2.16}$$

The Lagrangian for the Higgs coupling to the EW bosons naturally leads to mass terms for the W, Z and Higgs boson,

$$\mathcal{L}_{Higgs} = \frac{1}{2} (\partial_\mu H)^2 - \frac{1}{2} m_H^2 H^2 + \left[m_W^2 W_\mu^+ W^{-\mu} + \frac{1}{2} m_Z^2 Z_\mu Z^\mu \right] \left(1 + \frac{H}{v} \right)^2 . \tag{2.17}$$

The masses depend on the vev and the couplings as

$$m_W = g\frac{v}{2}, \quad m_Z^2 = \sqrt{g^2 + g'^2}\frac{v}{2}, \quad m_H = \sqrt{2\lambda} v \, . \tag{2.18}$$

Here the EW bosons were written as mass eigenstates. These are related to the interaction eigenstates W_μ^a and B_μ used earlier via

$$W_\mu^\pm = \frac{1}{\sqrt{2}} \left(W_\mu^1 \mp i W_\mu^2 \right) \text{ and} \tag{2.19}$$

$$\begin{pmatrix} Z_\mu \\ A_\mu \end{pmatrix} = \begin{pmatrix} \cos\theta_W & -\sin\theta_W \\ \sin\theta_W & \cos\theta_W \end{pmatrix} \begin{pmatrix} W_\mu^3 \\ B_\mu \end{pmatrix} . \tag{2.20}$$

The weak mixing angle θ_W is defined by

$$\cos\theta_W = \frac{g}{\sqrt{g^2 + g'^2}} \, . \tag{2.21}$$

The mass basis corresponds to the $\mathrm{U}(1)_{\mathrm{em}}$ eigenbasis so that the particles have well defined em charges.

The Higgs doublet can also generate mass terms for the fermions, both leptons and quarks, because it allows to write gauge invariant terms for the Lagrangian which contain left- and right-handed fields simultaneously,

$$\mathcal{L}_{\text{lepton masses}} = -\lambda_e \overline{E}_\mathrm{L} \cdot \phi e_\mathrm{R} + \text{h.c.} = -\frac{1}{\sqrt{2}} \lambda_e v \bar{e}_L e_R + \text{h.c.} \, , \tag{2.22}$$

$$\mathcal{L}_{\text{quark masses}} = -\frac{1}{\sqrt{2}} \lambda_d v \bar{d}_L d_R - \frac{1}{\sqrt{2}} \lambda_u v \bar{u}_L u_R + \text{h.c.} \, . \tag{2.23}$$

In the SM, there are 3 generations of quarks and leptons,

$$u_\mathrm{L}^i = (u_\mathrm{L}, c_\mathrm{L}, t_\mathrm{L}) \, , \quad d_\mathrm{L}^i = (d_\mathrm{L}, s_\mathrm{L}, b_\mathrm{L}) \, , \quad l_\mathrm{L}^i = (e_\mathrm{L}, \mu_\mathrm{L}, \tau_\mathrm{L}) \, . \tag{2.24}$$

The interaction and mass eigenstates can also differ and are in general related by a unitary transformation

$$u_\mathrm{L}^i = U_u^{ij} u'^j_\mathrm{L}, \quad d_\mathrm{L}^i = U_d^{ij} d'^j_\mathrm{L}. \tag{2.25}$$

The coupling of quarks to the W boson as introduced in equation (2.13) acts only within one generation. When more generations are added, they are independent in the interaction basis. Rotating to the mass basis by substituting equation (2.25) in equation (2.13), leads to couplings involving quarks of different generations,

$$J_W^{\mu+} = \frac{1}{\sqrt{2}}\overline{u}_{\mathrm{L}}^{i}\gamma^{\mu}d_{\mathrm{L}}^{i} = \frac{1}{\sqrt{2}}\overline{u}'^{i}_{\mathrm{L}}\gamma^{\mu}\underbrace{\left(U_u^{\dagger}U_d\right)_{ij}}_{V_{ij}}d'^{j}_{\mathrm{L}}\,. \tag{2.26}$$

The new matrix V_{ij} is the Cabibbo-Kobayashi-Maskawa (CKM) matrix, which allows transitions of quarks to different generations (or flavours). The effect of the CKM matrix for WH(j) production will be discussed in section 3.5.

2.2. Anomalous couplings and effective field theories

Anomalous couplings are a general extension of the SM couplings. They are described by an effective field theory (EFT). The idea of EFTs is to take a theory at a high scale Λ and consider its low energy limit. Operators are written in terms of the low-energy fields while the high-energy theory enters in the form of additional derivatives in these operators. Effective field theories are useful to describe and parametrize effects of (high scale) new physics with minimal additional assumptions. The Lagrangian of an EFT is in general non-renormalizable, which manifests in dimensionful couplings,

$$\mathcal{L}_{\mathrm{EFT}} = \sum_i \frac{f_i}{\Lambda^{d-4}}\mathcal{O}_i^{(d)}\,. \tag{2.27}$$

In equation (2.27), the general structure of an EFT Lagrangian is shown. As it is valid at a certain low-energy regime, the operators $\mathcal{O}_i^{(d)}$ must respect the symmetries at that scale. The overall mass dimension of a term in the Lagrangian is 4 to make the action $S = \int \mathrm{d}^4x\mathcal{L}$ dimensionless. Therefore, an operator $\mathcal{O}_i^{(d)}$ of mass dimension d requires a coupling of the form f_i/Λ^{d-4}. While there is no inherent limit on the dimensionality of these operators, the low-energy limit corresponds to an expansion in $(E/\Lambda)^d$, so that typically only the lowest order operators are considered.

The classic example of an EFT is the description of weak interactions by Fermi [15]. This theory describes β-decay using a vertex connecting four particles directly. The Lagrangian for this interaction can be written as

$$\mathcal{L} = -\frac{G_{\mathrm{F}}}{\sqrt{2}}\bar{p}\gamma^{\alpha}(1-\gamma_5)n\ \bar{e}\gamma_{\alpha}(1-\gamma_5)\nu_e\,. \tag{2.28}$$

This formulation already makes use of the vector minus axial vector structure of the weak interaction. The dimensionality of the operator requires the coupling to have mass dimension -2. Experimentally the coupling is well studied and the value is known precisely: $G_{\mathrm{F}} = 1.63371(6)\cdot 10^{-5}\,\mathrm{GeV}^{-2}$ [16].

As any EFT, this theory is only valid in a certain energy regime and the full theory must be used to give a correct description of the high energy region. In case of the Fermi interaction, at energies at the order of the weak scale, the W boson propagator can be resolved and the GWS theory introduced in section 2.1.2 needs to be used. As shown in figure 2.1 the four-fermion vertex is then replaced by two weak couplings and a propagator.

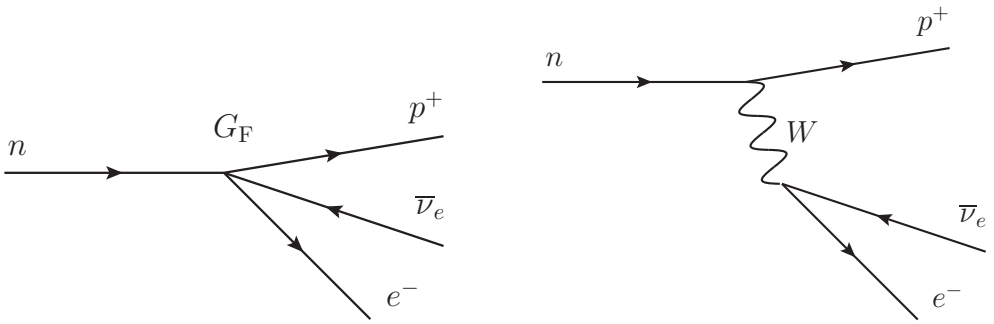

Figure 2.1: β-decay can be described in the low-energy limit by Fermi's interaction (left), while the description by the weak interaction (right) holds up the electroweak scale. In the low energy limit the intermediate W propagator is reduced to a vertex with a dimensionful coupling.

In the Lagrangian this replacement corresponds to

$$-\frac{G_\mathrm{F}}{\sqrt{2}} \leftrightarrow \frac{g^2}{8}\frac{1}{q^2 - m_\mathrm{W}^2}\,. \tag{2.29}$$

In the low energy limit the propagator is reduced to the mass,

$$\frac{1}{q^2 - m_\mathrm{W}^2} \overset{q^2\to 0}{\longrightarrow} -\frac{1}{m_\mathrm{W}^2}\,. \tag{2.30}$$

This relates the couplings as

$$\frac{G_\mathrm{F}}{\sqrt{2}} = \frac{g^2}{8m_\mathrm{W}^2}\,. \tag{2.31}$$

2.2.0.2. Anomalous couplings

Anomalous couplings as an extension of the SM enter in dimensionful operators added to the SM Lagrangian. Assuming a QFT at a higher scale, the SM would be the leading terms in the low-energy expansion and anomalous couplings appear in higher order terms.

Considering the EW bosons and the Higgs boson, terms in the Lagrangian can be written by using

$$\begin{aligned} \hat{W}_{\mu\nu} &= i\frac{g}{2}W^a_{\mu\nu}\sigma^a\,, & \hat{B}_{\mu\nu} &= i\frac{g'}{2}B_{\mu\nu}\,, \\ D_\mu &= \partial_\mu + igW^a_\mu\frac{\sigma^a}{2} + i\frac{g'}{2}B_\mu\,, & \Phi &= \frac{1}{\sqrt{2}}\begin{pmatrix} 0 \\ v+H \end{pmatrix}\,. \end{aligned} \tag{2.32}$$

With these "building blocks" operators can be constructed. New operators have to respect all symmetries of the theory, including gauge symmetries. With the given symmetries it is not possible to construct operators of odd dimension. The SM operators have dimension 4, so that anomalous couplings can enter as dimension 6 or dimension 8 operators. New terms are suppressed by Λ^{-d+4}, so the lowest possible dimensions should give the largest contribution. For the VVH vertex, all possible Lorentz structures are present in the dimension 6 operators. Therefore, dimension 8 operators only add additional couplings. While those could be used to fit several cross sections simultaneously, they do not provide additional information to WH(j) production and, hence, will not be discussed here.

The relevant dimension 6 operators are [3, 17]

$$\begin{aligned}
\mathcal{O}_W &= (D_\mu\Phi)^\dagger \hat{W}^{\mu\nu}(D_\nu\Phi)\,, \\
\mathcal{O}_B &= (D_\mu\Phi)^\dagger \hat{B}^{\mu\nu}(D_\nu\Phi)\,, \\
\mathcal{O}_{WWW} &= Tr\left[\hat{W}_{\mu\nu}\hat{W}^{\nu\rho}\hat{W}_\rho^\mu\right]\,, \\
\mathcal{O}_{WW} &= \Phi^\dagger \hat{W}_{\mu\nu}\hat{W}^{\mu\nu}\Phi\,, \\
\mathcal{O}_{BB} &= \Phi^\dagger \hat{B}_{\mu\nu}\hat{B}^{\mu\nu}\Phi\,, \\
\mathcal{O}_{\Phi,1} &= (D_\mu\Phi)^\dagger \Phi\Phi^\dagger (D^\mu\Phi)\,, \\
\mathcal{O}_{DW} &= Tr\left(\left[D_\mu, \hat{W}_{\nu\rho}\right]\left[D^\mu, \hat{W}^{\nu\rho}\right]\right)\,, \\
\mathcal{O}_{BW} &= \Phi^\dagger \hat{B}_{\mu\nu}\hat{W}^{\mu\nu}\Phi\,.
\end{aligned} \tag{2.33}$$

As discussed in Refs. [3, 18], the last 3 operators, $\mathcal{O}_{\Phi,1}$, $\mathcal{O}_{DW}$ and $\mathcal{O}_{BW}$ modify the gauge boson two-point functions. They are strongly restricted and including only the vertex corrections without modifying the propagators leads to inconsistencies. Therefore they are not considered in this thesis. Operators influencing only the Higgs boson self couplings are also ignored.

The operators in equation (2.33) are $\mathcal{CP}$-even. In analogy $\mathcal{CP}$-odd operators can be constructed using the dual field strength tensors,

$$\begin{aligned}
\hat{\widetilde{W}}_{\mu\nu} &= \frac{1}{2}\epsilon_{\mu\nu\rho\sigma}\hat{W}^{\rho\sigma}\,, \\
\hat{\widetilde{B}}_{\mu\nu} &= \frac{1}{2}\epsilon_{\mu\nu\rho\sigma}\hat{B}^{\rho\sigma}\,.
\end{aligned} \tag{2.34}$$

The possible dimension 6 $\mathcal{CP}$-odd operators are

$$\begin{aligned}
\mathcal{O}_{\widetilde{W}} &= (D_\mu\Phi)^\dagger \hat{\widetilde{W}}^{\mu\nu}(D_\nu\Phi)\,, \\
\mathcal{O}_{\widetilde{B}} &= (D_\mu\Phi)^\dagger \hat{\widetilde{B}}^{\mu\nu}(D_\nu\Phi)\,, \\
\mathcal{O}_{\widetilde{W}WW} &= Tr\left[\hat{\widetilde{W}}_{\mu\nu}\hat{W}^{\nu\rho}\hat{W}_\rho^\mu\right]\,, \\
\mathcal{O}_{\widetilde{W}W} &= \Phi^\dagger \hat{\widetilde{W}}_{\mu\nu}\hat{W}^{\mu\nu}\Phi\,, \\
\mathcal{O}_{\widetilde{B}B} &= \Phi^\dagger \hat{\widetilde{B}}_{\mu\nu}\hat{B}^{\mu\nu}\Phi\,.
\end{aligned} \tag{2.35}$$

For the production of WH(j), these operators do not lead to new Feynman diagrams, but only modify the WWH vertex. The operators contributing to this vertex are $\mathcal{O}_W, \mathcal{O}_{\widetilde{W}}, \mathcal{O}_{WW}$ and $\mathcal{O}_{\widetilde{W}W}$. The Feynman rules corresponding to these operators were calculated and implemented in Ref. [18]. The effect of anomalous couplings on differential cross sections will be discussed in section 5.5.

2.3. Next-to-Leading Order effects in QCD

The calculation of the cross section is performed within perturbation theory as an expansion in the coupling constants. This lowest order in this expansion is called *leading order* (LO). In the processes discussed here, LO occurs at *tree level* and therefore it does not contain loops.

The next-to-leading order contains all contributions with one additional factor of the coupling constant. There are two fundamental couplings involved: α_s for QCD and α for the EW interactions. $\alpha_s \approx 0.1$ is an order of magnitude larger than $\alpha \approx 0.008$, therefore the QCD corrections are in general dominating. In this thesis, EW corrections are not included in the calculation.

There are two contributions to the NLO cross section: The virtual corrections σ^V and the real emission σ^R, which are distinguished by the number of final state particles and therefore phase space dimension. Schematically this can be written as

$$\sigma^{NLO} = \int_m \mathrm{d}\sigma^V + \int_{m+1} \mathrm{d}\sigma^R. \tag{2.36}$$

For the real emission, the addition of a final state QCD particle adds one factor of the coupling, so that $|\mathcal{M}_{\mathrm{RE}}|^2$ has one more factor of α_s than the LO matrix element squared.

In case of the virtual corrections, an additional loop can be thought of as an additional gluon connected to a quark line in two places so that there are two couplings giving an overall factor of α_s. Therefore, the virtual contributions enter as interference terms in the form $2\,\mathrm{Re}\,[\mathcal{M}_{\mathrm{B}}\mathcal{M}_{\mathrm{V}}]$. For the NLO calculation also different PDFs have to be used, which absorb initial-state singularities.

2.3.1. Catani Seymour

When performing the numerical integration of equation (2.36) to calculate a NLO cross section, two integrals with different dimensionality have to be evaluated. These two integrals are individually divergent. These divergences occur when pairs of particles are soft or collinear.

Their divergence structure can be made apparent using *regularization*. There are different regularization schemes. A common choice is *dimensional regularization* which changes the space-time dimension to be $D = 4 - 2\varepsilon$. With ε, a small quantity which regularizes the divergences. The divergent parts show up as $1/\varepsilon$ and $1/\varepsilon^2$. The IR divergent poles in the virtual contribution should exactly cancel the poles in the real emission. This cancellation is stated in the Kinoshita-Lee-Nauenberg (KLN) theorem [19, 20].

The poles on the real emission only appear after the phase space integration. However, this would spoil the convergence of our MC program. To extract the poles prior integration, several methods exit in the literature. A common choice for NLO Monte Carlos was developed by Catani and Seymour [21, 22].

The subtraction term is constructed to reproduce the divergence structure of the real emission and be analytically integrable over a variable parametrizing the soft and collinear limit. Technically, in equation (2.36) the integrated version of the subtraction terms is added to the virtuals and the unintegrated version subtracted from the real emission. This makes both phase space integrals separately finite without modifying the sum. Including the subtraction terms the cross section is

$$\sigma^{NLO} = \int_m \left(\mathrm{d}\sigma^V + \int_1 \mathrm{d}\sigma^A\right) + \int_{m+1} \left(\mathrm{d}\sigma^R - \mathrm{d}\sigma^A\right). \tag{2.37}$$

There are not only terms resembling the divergence structure but also finite terms. These can be moved from the m to the $m+1$ dimensional integral, which can be used to cross check the consistency of the calculation.

Colliding particles	leptons electrons, muons	hadrons protons, anti-protons
particles in hard interaction	same as accelerated	partons inside the hadron
energy spread	narrow, known from acceleration	wide, partons carry momentum fraction
maximum energy	few hundred GeV limited by synchrotron radiation	several TeV synchrotron radiation smaller by $[m_e/m_p]^4$
final state	small number of additional particles	many hadron remnants and additional QCD interactions

Table 2.1: Lepton and hadron colliders are compared in several key aspects.

2.4. Particle colliders

There are many possible experiments for testing theories in particle physics. To produce heavy particles and study their properties, both high energies and a large number of events are needed. The most common experimental approach to achieve this is to study particle collisions. Collisions can either be produced by shooting particles on a fixed target or by a head-on collision of two particles. In the first case, the center-of-mass energy, $\sqrt{s}$, of the final state produced depends on the beam energy E and the mass m of the target particle: $s = 2mE$. For a particle collider with two approximately massless particles with the same energy E, the center-of-mass energy is given by $s = 2E^2$.

While the mass of accelerated particles m is of the order of a few GeV, E can reach hundreds of GeV or even a few TeV in modern colliders. Therefore, they offer a superior energy for experiments.

In general, accelerating particles is easiest if they are

- charged: such that a combination of electric and magnetic fields can be used to accelerate, deflect and focus them
- easily produced: so they are available in large quantities
- stable/long lived: so they do not decay before the collision

Typical combinations used were

- electron - positron (LEP, CERN),
- electron - proton (HERA, DESY),
- proton - antiproton (Tevatron, Ferminlab),
- proton - proton (LHC, CERN).

Other possibilities include muons [23] or heavy nuclei. The choice of particles to collide is critical for the design of the accelerator and detectors as well as the possible physical observations. An overview of key differences between lepton and hadron colliders is presented in table 2.1.

2.4.1. Hadron colliders

Hadrons are a stable bound of partons (quarks and gluons). When they collide at energies well above their mass, there is a hard interaction between one parton of each of the colliding particles. "After" this hard interaction, the resulting particles *hadronize* to form colour-neutral states, which can then be identified in detectors.

When predicting events at a hadron collider, the calculation is therefore divided into calculating a hard cross section using perturbation theory with partons and then modelling other effects at lower energies around that. In this thesis, only the hard interaction will be discussed.

2.4.2. Event rates and cross sections

In a collider experiment, *events* are recorded, which are a set of final state particles with their energies and momenta. The frequency with which events with a given property occur gives the *event rate*. This rate depends on the accelerator setup as well as the selection criteria of the event. The dependence on the accelerator setup can be factorized,

$$\underbrace{N}_{\text{event rate}} = \underbrace{\sigma}_{\text{cross section}} \cdot \underbrace{\mathcal{L}}_{\textit{luminosity}} . \tag{2.38}$$

Luminosity

$\mathcal{L}$ is the *luminosity*. Its units are $^1/_{\text{Area}\cdot\text{Time}}$. The luminosity measures the number of potential collisions a collider produces per unit of time. Frequently, the *integrated luminosity* is used, which is the integrated luminosity over time.

For a simplified model of two beams in a storage ring with several bunches, the luminosity is given by

$$\mathcal{L} = fn\frac{N^2}{A}, \tag{2.39}$$

where

- n is the number of particle bunches
- N the number of particles within one bunch
- f the frequency of a bunch going around the ring
- A the effective interaction area of two crossing bunches, which depends on the particle densities within a bunch and their shape

Integrated luminosity is typically given in barn, with $1\,\text{barn} = 1 \cdot 10^{-24}\,\text{cm}^{-2}$. In 2012 the proton-proton LHC delivered $\approx 23\,\text{fb}$.

Factoring out the luminosity, the *cross section* σ, which depends on type and energy of the particles colliding should be computed.

Cross section

The cross section can be calculated using the framework of QFT. As derived in Ref. [8], the cross section can be written as

$$d\sigma = \frac{1}{2\hat{\text{s}}} \left|\mathcal{M}\left(p_1, p_2 \to \{p_\text{f}\}\right)\right|^2 d\text{PS}, \tag{2.40}$$

where

- $\frac{1}{2\hat{s}}$ is the flux factor, which is written here in the case of massless/relativistic particles as the inverse of twice the invariant mass squared of the incoming particles
- $\mathcal{M}$ is the matrix element
- $d\mathrm{PS}$ is the phase space factor

The matrix element can be calculated using *Feynman Rules* derived from the underlying Theory. The phase space factor includes the integration over the possible final state momenta in a Lorentz invariant way,

$$d\mathrm{PS} = \left(\prod_{\mathrm{f}} \frac{\mathrm{d}^3 \mathrm{p_f}}{(2\pi)^3 \, 2\mathrm{E_f}} \right) (2\pi)^4 \, \delta^{(4)} \left(\mathrm{p_1} + \mathrm{p_2} - \sum \mathrm{p_f} \right) . \tag{2.41}$$

Details on how to perform the integral are described in section 2.6.

2.4.3. Parton distribution functions

When describing hadronic collisions, the hard interactions take place between the constituents of the hadron, the partons. Therefore, a hadronic cross section has to account for this by summing over the possible partons and integrating over the possible momentum fractions. Additionally, there is a factor that describes the probability that at a given energy scale, a specific parton with a certain momentum fraction will interact. This probability is given by the *parton distribution function* (PDF).

Using PDFs, the cross section for the interaction of two protons can be written,

$$\sigma = \int dx_1 dx_2 \sum_{\text{partonic subprocesses}} f_{q_1}\left(x_1, Q^2\right) f_{q_2}\left(x_2, Q^2\right) \sigma_{\text{partonic}}\left(q_1, x_1 P_1; q_2, x_2 P_2 \to \{p_\mathrm{f}\}\right) . \tag{2.42}$$

The sum includes all relevant combinations of partons q_1 and q_2 for the specific process and the integral folds the PDFs with the corresponding parton-level cross section. This cross section then only depends on the type of partons and the momenta of the parton, which is given by the momentum fraction x_i multiplied with the proton momentum P_i.

The dependence of the PDFs on the energy scale is known, so that they can be *evolved* to arbitrary scales starting from a given scale using the DGLAP equation [24, 25, 26]. There are several groups calculating PDFs by parametrizing a general shape and fitting it to existing data from scattering experiments. The PDFs used here are presented in Refs. [27, 28] and shown in figure 2.2. PDFs have to fulfill several constraints. The overall momentum of the proton should be conserved,

$$\int_0^1 \sum_{\text{partons}} x \, q(x) \, \mathrm{dx} = 1 \, . \tag{2.43}$$

At low scales, the total parton content of the proton should be *uud*. Therefore,

$$\begin{aligned} \int_0^1 u(x) - \bar{u}(x) \, \mathrm{dx} &= 2 \, , \\ \int_0^1 d(x) - \bar{d}(x) \, \mathrm{dx} &= 1 \, , \\ \int_0^1 q(x) - \bar{q}(x) \, \mathrm{dx} &= 0 \quad \forall q \notin \{u, d\} \, . \end{aligned} \tag{2.44}$$

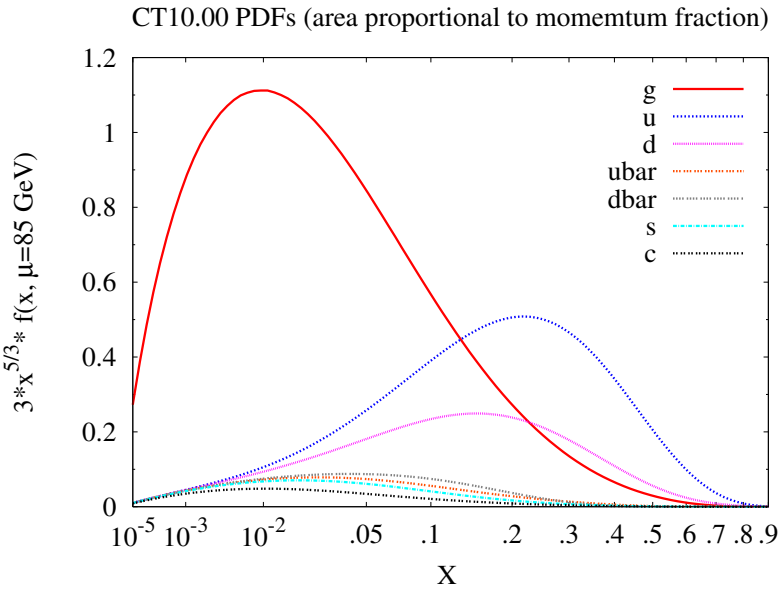

Figure 2.2: The PDFs from Refs. [27, 28] are used in this thesis. The gluon PDF is dominant for small x and the quark PDFs show the dominant valence quarks u and d as well as the sea quarks.

2.5. Higgs boson physics

In July 2012, a new particle was discovered by ATLAS [1] and CMS [2], which looks like the SM Higgs boson. This discovery is the beginning of a new series of studies of the properties of the discovered particle. The properties of the SM Higgs boson are theoretically well studied and many interesting production processes and decay channels are known, which will help to understand the properties of the new particle and compare it to the SM expectations.

2.5.1. Decays of the Higgs boson

Because the Higgs boson couples to all massive particles and is itself quite heavy, there are many possible decay channels. The Higgs boson does not carry colour or charge. These properties are conserved and, therefore, the final state of the decay also has to be electrically neutral and have no colour.

The Higgs boson coupling to fermions is proportional to their mass. The heaviest fermion is the top, which is heavier than the Higgs boson (173 GeV compared to 126 GeV). Therefore, the decay into of the Higgs boson in to two top quarks is not possible. A decay into a final state via two virtual tops is possible but heavily suppressed. The Higgs boson can decay via a top-loop, which makes use of the large coupling but is not kinematically restricted.

The most common decay channels for the Higgs boson are shown with their branching ratio in figure 2.3. The dependence of the branching ratios on the mass of the Higgs boson is shown. In the following, a Higgs mass of 126 GeV is assumed and numerical values from Ref. [29] are used.

$b\bar{b}$ The second heaviest fermion in the SM is the b quark. Therefore, the Higgs boson couples rather strongly to it. The decay to a b and anti-b ($\bar{b}$) quark is the most likely for the SM Higgs with a mass of 126 GeV: $BR(h \to b\bar{b}) = 56\%$.

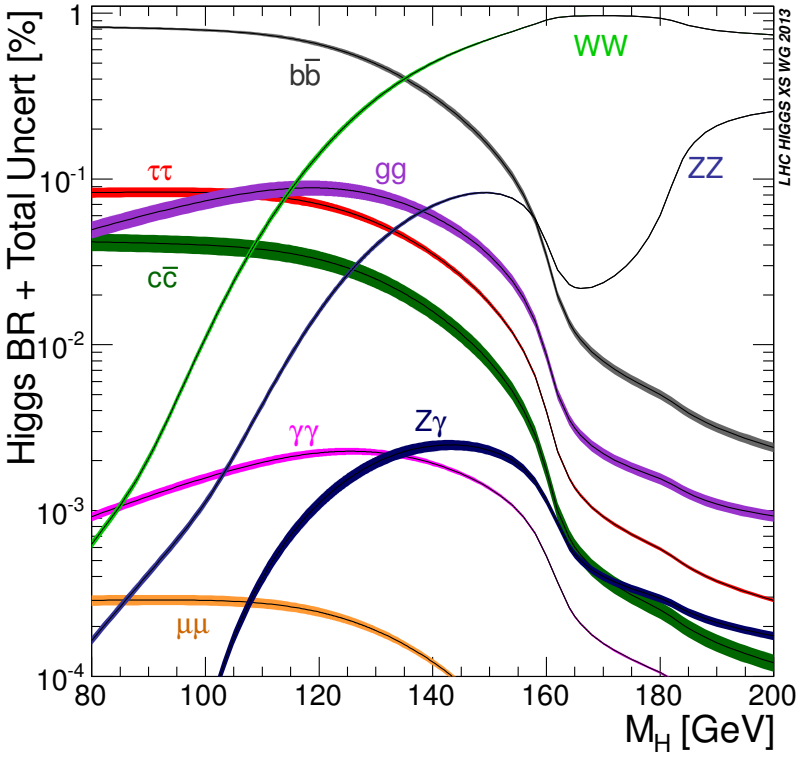

Figure 2.3: This plot from Ref. [29] shows the branching ratio of the Higgs boson in the main decay channels depending on the Higgs mass. The decays to WW and ZZ are dominant for large Higgs masses, though below their mass threshold the decay to $b\bar{b}$ is the dominant channel. The different decays and their properties are discussed in the text.

$\tau^+\tau^-$ The τ is the next heaviest fermion. It can decay leptonically, providing a good signature in the detector. This decay contains neutrinos, which limits the mass resolution of the reconstruction.

$\gamma\gamma$ The decay to photons is loop-induced, which reduces the branching ratio. The mass resolution in this channel is really good, so that the rather smooth background can be fitted in side-bins and subtracted. It is one of the discovery channels.

$ZZ \to 4l$ The decay via ZZ to 4 leptons is also called the Golden Channel. Leptons allow a precise mass reconstruction and especially muons provide a mass resolution comparable to photons. This channel is limited by the small branching ratio.

WW In comparison, WW has a relatively high rate, but because leptonic W decays produce neutrinos, the mass can not be reconstructed. A transverse mass can be reconstructed, which allows a mass fit to simulation data. Spin correlations of the decay favor the leptons in the same direction. This allows to use angular distributions to reduce backgrounds.

$Z\gamma$ This channel is similar to $\gamma\gamma$, but due to the $Z \to 2l$ branching ratio it has a smaller cross section. It is interesting for setting limits on decays to non-SM particles, as theories beyond the SM often allow parameter choices to explain the $\gamma\gamma$, WW and ZZ rate, but not at the same time the $Z\gamma$ rate.

$\mu\mu$ The decay to muons is the only possible channel to measure the Yukawa couplings of the second generation at the LHC. It has a good mass resolution but it is limited by the small branching ratio and a large background from muon pair production via a virtual Z or photon.

invisible The branching ratio of the Higgs boson to particles not visible in the detectors can be limited in production processes, which allows a tagging of associated particles, as in VBF or VH. Limiting this branching ratio allows to test beyond SM theories.

2.5.2. Higgs boson production

At the LHC there are several channels to produce a Higgs boson. As seen in figure 2.4, there are 4 relevant production channels at the LHC. The Feynman diagrams of these processes are shown in figure 2.5. In more detail the processes are:

Gluon Fusion (GF), gg $\rightarrow$ H GF has the largest cross section and, therefore, it is the dominant discovery channel. Corrections beyond NNLO have been calculated and they are large ($\approx 80\% - 100\%$, [30]). Additionally, there are accompanying jets radiated quite isotropically. This implies that there are huge backgrounds from X + multijet productions processes.

Vector Boson Fusion (VBF), qq $\rightarrow$ qqH VBF is the production process with the second largest cross section. While a naive estimate based on couplings would suggest this process is suppressed by α_{EW}^2, it is only a factor 10 smaller than GF. VBF has two additional jets in the final state which have the remarkable kinematical feature that they tend to be *forward*, allowing a clear tagging of these events. Additional radiation in the central part of the detector is highly suppressed, which helps to eliminated QCD backgrounds. VBF is related to Vector Boson Scattering, which is interesting for studying unitarity violations.

Higgsstrahlung (VH), q$\overline{\mathrm{q}}$ $\rightarrow$ WH The third highest cross section for producing a Higgs boson at the LHC is via the associated production with a vector boson. This is also known as *Higgsstrahlung*, which refers to the Feynman diagram that can be described as the production of a vector boson which then radiates off a Higgs boson. The vector boson can be either a W or Z, where the WH case is slightly larger than ZH. The vector boson in the final state can decay leptonically. This lepton can then be tagged, allowing a better discrimination against backgrounds.

In this thesis, Higgsstrahlung with a W boson is calculated as well as the production in association with an additional jet.

Associated production with heavy quarks The Higgs boson can also be produced in association with heavy quarks (top or bottom). This channel is interesting for studying models with enhanced bbH or ttH couplings. In the SM case there is a large QCD background which restricts the H $\rightarrow$ b$\overline{\mathrm{b}}$ decay channel while the others are restricted by the small cross section.

2.5.2.1. Higgs boson self couplings

Determining the decay widths and production cross sections of the different channels is an important check for the consistency of the observed particle with the SM Higgs boson. Another step is to measure the coefficients of the Higgs potential introduced in equation (2.14).

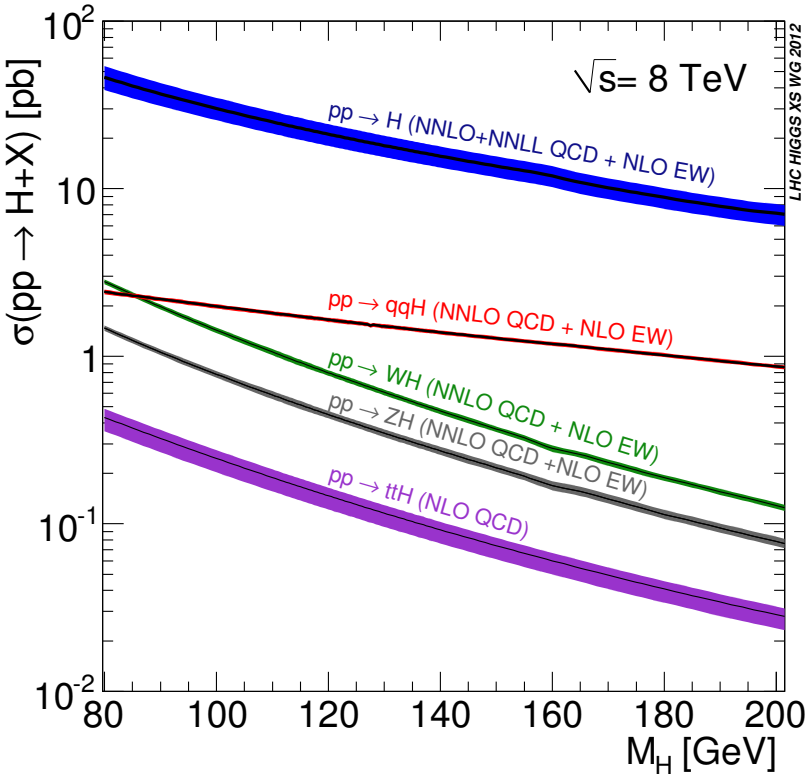

Figure 2.4: The cross sections of the main Higgs production modes at the LHC running at a center-of-mass energy of 8 TeV are shown. The dominant mode is Gluon Fusion, followed by Vector Boson Fusion and Higgsstrahlung.

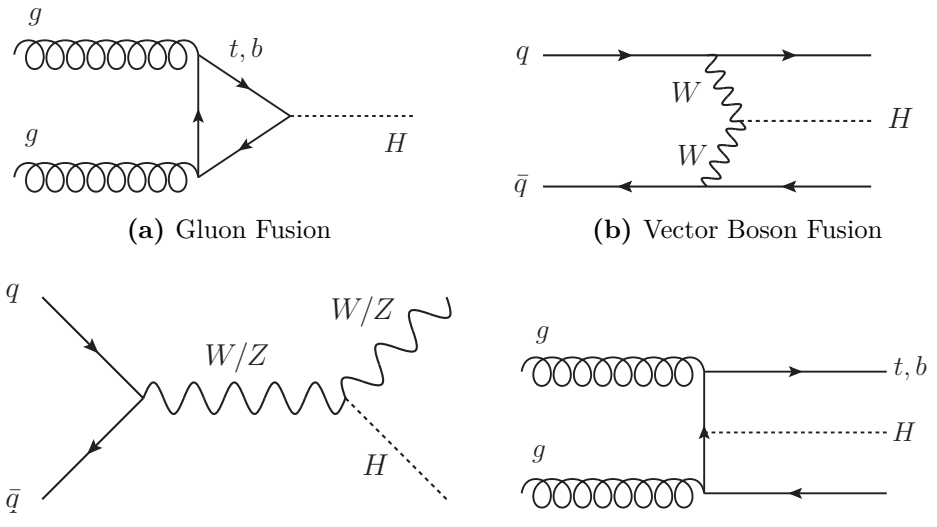

(a) Gluon Fusion

(b) Vector Boson Fusion

(c) Higgsstrahlung

(d) heavy quark associated production

Figure 2.5: Feynman diagrams for the different Higgs boson production channels at the LHC are shown. Gluon fusion has the largest cross section. The other processes produce the Higgs boson in association with additional final state particles which allow a tagging of the specific production mode.

This Higgs potential has two parameter, μ and λ. Together with the vev v they describe the Higgs sector of the SM. v can be expressed by G_f and $m_{\mathrm{W,Z}}$, which are measured in the EW sector. Together with the Higgs boson mass, μ can be derived. The quartic term in the Higgs potential leads to Higgs self couplings in the form of triple and quartic vertices. The effect of those vertices could be measured as corrections to other processes, but those are generally small. The production of two Higgs bosons would give access to the triple vertex, hence, to λ.

2.5.3. Higgsstrahlung – WH

For the production of a Higgs boson in association with a W boson, there are several interesting decay channels. Because of the rather small production cross section, the decays with a large branching ratio (BR) are more interesting.

The largest Higgs BR is $\mathrm{H} \to \mathrm{b\bar{b}}$, which leads to the final state $\mathrm{Wb\bar{b}}$. This final state has a large background from W + jets. This background can be reduced by applying subjet analysis in the boosted regime as suggest in Ref. [31]. Other decays like $\mathrm{H}\to\mathrm{WW}$ or $\mathrm{H}\to\gamma\gamma$ lead to triple EW boson final states, which are also studied to examine gauge boson interactions.

The leptonic decay of the additional vector boson can be tagged in the detector to identify events. This facilitates a search for invisible decays of the Higgs boson or decays to particles beyond the Standard Model in WH production. An example for such a search is presented by ATLAS in Ref. [7].

WH also gives access to the WWH coupling as well as the bbH coupling. For the decay $\mathrm{H}\to\mathrm{b\bar{b}}$, WH is expected to give a better signal than GF and VBF, due to the large backgrounds in those channels.

In the experimental searches for WH production at the 7 and 8 TeV LHC presented in Refs. [4, 5], there was no established signal yet, but a SM Higgs boson should be visible in WH production with increased luminosity.

2.6. Monte Carlo

When calculating a cross section, the integral over the available phase space has to be computed as discussed in section 2.4.2. This integration is difficult for several reasons:

high dimensionality Depending on the number of jets and the chosen Higgs boson decay channel, there are up to 21 integration variables. Therefore, a naive integration using a grid with equal spacing in each dimension is not feasible, since the number of function evaluations grows with the number of dimensions as N^d.

large variance The integrand (the matrix element) is not flat, but has many peaks and other features. Any approximation that assumes only small deviations from a flat distribution will therefore not give a good approximation.

non-diagonal boundaries when using general cuts The integral boundaries depend on the experimental cuts chosen. Those often combine several variables (e.g. in separation cuts) and can not be directly modelled by integration boundaries.

computing time For each phase space point evaluated, the corresponding matrix element has to be calculated. This calculation can be slow, especially in the case of loop integrals. Therefore, the number of integrand evaluations should be kept rather small.

A general introduction to Monte Carlo techniques is given in Ref. [32]. The idea of Monte Carlo integration is to choose random points in the phase space and use those to estimate the integral. For simplicity an integration over the unit hypercube $[0,1]^d$ is assumed,

$$I = \int f(x) d^d x. \tag{2.45}$$

Using N random points x_i, the Monte Carlo estimate of the integral is

$$E_N = \frac{1}{N} \sum_{i=1}^{N} f(x_i). \tag{2.46}$$

This estimate converges to the full integral for large N

$$\lim_{N\to\infty} \frac{1}{N} \sum_{i=1}^{N} f(x_i) = I. \tag{2.47}$$

Monte Carlo integration allows to give an error estimate for finite N. To do so, the variance σ_f^2 of a function f is used, which is defined as

$$\sigma^2(f) = \frac{1}{N-1} \sum_{i=1}^{N} \left(f(x_i) - E_N\right)^2. \tag{2.48}$$

The variance of the Monte Carlo integral is

$$\sigma^2_{E_N} = \frac{1}{N^2} \sum_{i=1}^{N} \sigma^2(f) = \frac{1}{N} \sigma^2(f). \tag{2.49}$$

The error of the estimate E_N will be of the same order as the variance. The function variance is a constant, such that the overall dependence on the number of phase space points used is $\sigma_{E_N} \propto 1/\sqrt{N}$. This does not depend on the dimensionality of the integral, which is an important advantage compared to traditional integration methods.

This variance can be calculated using the function values at the random points chosen and, thereby, allows to give a continuous estimate of the variation while performing the integration.

2.6.1. Importance sampling

Using properties of the integrand, the Monte Carlo integration can be improved. There are different methods available, which highly depend on the application at hand and can be automated to different degrees.. Manual improvements will be discussed in section 3.2.

The algorithm used for the calculations in this thesis is based on the idea of importance sampling, which is also discussed in Ref. [32]. The idea of importance sampling is to guess a function that approximates the integrand and use it to change the integration variables,

$$\int f(x)\mathrm{dx} = \int \frac{\mathrm{f(x)}}{\mathrm{p(x)}} \mathrm{p(x)dx} = \int \frac{\mathrm{f(x)}}{\mathrm{p(x)}} \mathrm{dP(x)}. \tag{2.50}$$

This requires the knowledge of $P(x)$ which is the integral of $p(x)$.

The statistical integration error then is $\sigma(f/p)/\sqrt{N}$. So if $p(x)$ is chosen to be proportional to $f(x)$ then $\sigma(f/p) = 0$. In any real situation $p(x)$ is only an approximation to $f(x)$ such that $\sigma(f/p)$ is non-zero but for a good choice of $p(x)$ it is significantly smaller than $\sigma(f)$.

2.6.2. VEGAS

VEGAS [33, 34] is an algorithm based on importance sampling. The integration is performed in several iterations which improve the importance sampling based on the calculated integrand values. The probability density p in equation (2.50) is factorized,

$$p(x_1, x_2, \ldots, x_d) = p_1(x_1) \cdot p_2(x_2) \cdot \ldots \cdot p_d(x_d). \tag{2.51}$$

Each p_i is considered individually and split into bins. The random sampling in uniform within each bin and all bins are used with the same probability. In the first iteration, those bins are of equal size. Using the function values of one iteration, the bin sizes in the next iteration are determined, such that each bin contains the same weight. By resizing the bins, integration regions with a larger contribution will get more points.

CHAPTER 3

WH AND WHJ PRODUCTION AT NLO

In this chapter, the calculation of the WH and WHj production cross sections, as well as those for W and Wj production, is discussed. The processes W^+H and W^-H are very similar and will be discussed simultaneously. For numerical examples in general the process W^+H is considered.

Cross sections calculated at LO have large uncertainties, which fails to fix the normalization of the cross section. They show up as scale dependencies. The calculation of NLO corrections reduces those uncertainties and is required to produce reliable predictions.

An overview of the program VBFNLO, into which the processes are implemented, is given in section 3.1. The phase space integration and the optimizations involved are described in section 3.2. Sections 3.3 and 3.4 discuss the calculation of processes at leading and next-to-leading order. Effects of the CKM matrix on the calculation are discussed in section 3.5. The choice of flavour scheme and its consistent treatment throughout the calculation are described in section 3.6.

3.1. VBFNLO

The calculated processes were implemented into the flexible Monte Carlo program VBFNLO [35, 36]. VBFNLO provides implementations of NLO QCD calculations for a variety of production processes including vector boson fusion and the production of two or three vector bosons, in several cases also with one or two additional jets. The implementations contain many reusable parts, including a framework for phase space generation and routines for the calculation of loops and subtraction terms.

3.1.1. New processes

In this thesis, four new production processes including NLO QCD corrections were implemented in VBFNLO: W, Wj, WH and WHj. Because they have a similar QCD structure to existing diboson and triboson processes, many aspects of the calculation could be reused. W and WH production are based on WA production[37], Wj and WHj production are based on WAAj production[38] as well as WZj production[39].

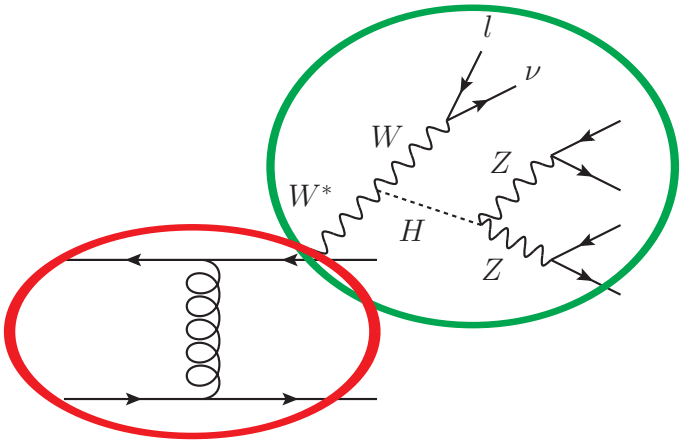

Figure 3.1: A Feynman diagram for WHjj with H → ZZ → 4*l* is shown as an example of the separation of EW (green) and QCD part of the diagram (red). The EW part is pre-calculated and attached to the QCD part in the form of an effective current.

3.1.2. Effective currents

Among the NLO parton level Monte Carlos, VBFNLO stands out especially as far as two aspects are concerned. First, for many processes, it is very fast. Secondly, anomalous couplings are implemented in most processes. One aspect that affects both features is the way Feynman diagrams are calculated. This is done by precalculating the electroweak (EW) parts including decays and also production of multiple particles via a resonance. These precalculated "effective currents" are then contracted with the QCD calculation in all necessary places. This separation is shown in figure 3.1. As an example, a LO diagram for WHjj with the Higgs boson decaying to 4 leptons is shown. This diagram can be separated into a QCD part, which only contains quarks and gluons interacting via the strong coupling, and into an EW part, which consists of W, Z, Higgs bosons and leptons, which are all connected via weak couplings. Both parts are joined by a W coupling to quarks.

The benefit of factoring EW and QCD parts is that extensions of one of them do not affect the other. This allows reusing the EW part of a LO calculation in a NLO QCD calculation, but also the EW part can be expanded with additional decays or anomalous couplings without modifying the QCD calculation. This allows to reuse the code that is checked and tested for more complex calculations.

The EW calculations in this thesis treat the W and the H as off-shell and include the leptonic decays of the W as well as many decays of the H, which are presented in section 3.3.1. Also anomalous couplings for the HWW vertex and the Higgs boson decays are included. WH production has the same QCD structure as W production including the NLO corrections. For WHJ, there are new diagram types at NLO in comparison with Wj, where the Higgs boson is not radiated off the W. They are discussed in section 3.4.2.2.

3.2. Phase space

As discussed in section 2.4.2, the computation of the cross section includes the calculation of matrix elements as well as the integration over the phase space. Here the phase space

integration will be discussed first, which is performed numerically. This is done by randomly generating phase space points. The matrix element is computed at each point and summed with the corresponding weight.

A point in phase space is generated in two steps. First a point gets generated using the knowledge of the LO diagrams. Then, this point is subjected to the user specified cuts and dropped if those are not satisfied. Having an efficient phase space generation is one of the key aspects for a fast and stable Monte Carlo. Phase space generation is difficult for several reasons.

The phase space integral has high dimensionality so that isolating independent variables is not trivial. The dimension of the integration depends on the multiplicity of the final state. For each final state particle, an integration $\int \mathrm{d}^3\mathrm{p_i}$ is added. There is an overall $\delta^4(\sum p_{\text{inital}} - \sum p_{\text{final}})$, which guarantees energy-momentum conservation and can be used to absorb 4 integrations. For the momenta fractions of partons in the protons, there are 2 integrations $\int \mathrm{dx_1 dx_2}$. An interaction in a particle collider has a rotational symmetry around the beam axis, so that one $\int \mathrm{d}\varphi$ can be saved. Overall, the number of integrations performed for a final state with n particles is

$$d_{\text{integration}} = 3n - 4 + 2 - 1 = 3n - 3\,. \tag{3.1}$$

The processes implemented have between 2 ($\mathrm{W} \to l\nu$) and 8 ($\mathrm{WHjj} \to l\nu 4ljj$) final state particles, leading to an integration with up to 21 integration variables. If no decay for the Higgs boson is chosen, then a general off-shell Higgs boson is produced with a Breit-Wigner shape factor. An additional integration is added for this parametrization of the Higgs boson mass.

To explain the difficulty of the task, a grid with 1000 points in each dimension will lead to 10^{63} matrix element evaluations. Therefore, a naive integration would be very time consuming. The Monte Carlo approach reduces this number to a more practical size. A general description of the Monte Carlo method is given in section 2.6.

Monte Carlo integration is optimal for a mostly flat integrand. However, the phase space dependence of the matrix elements is typically far from flat. Generating phase space points for a fast and stable convergence of the integration needs knowledge of the structure of the integrand – the matrix element. This includes propagators and angular correlations of interactions. Using the VBFNLO framework,[1] a basis for the integration is chosen that consists of variables covering independent structures. When such structures have a known shape and are parametrized by a single variable, they can be remapped to a more flat distribution. One recurring distribution is the Breit-Wigner resonance.

3.2.1. Breit-Wigner resonance – Tan mapping

If the shape of a distribution is approximately known, the technique discussed in section 2.6.1 can be used. A commonly recurring shape is the Breit-Wigner resonance which describes the invariant mass of an unstable intermediate particle. It corresponds to the squared absolute value of this particles propagator where the width is included in the convention of the complex mass scheme,

$$g(p^2) = \frac{M\Gamma}{\pi} \frac{1}{\left(p^2 - M^2\right)^2 + M^2\Gamma^2}\,. \tag{3.2}$$

[1] VBFNLO has a collection of helper functions in ps_tools.F

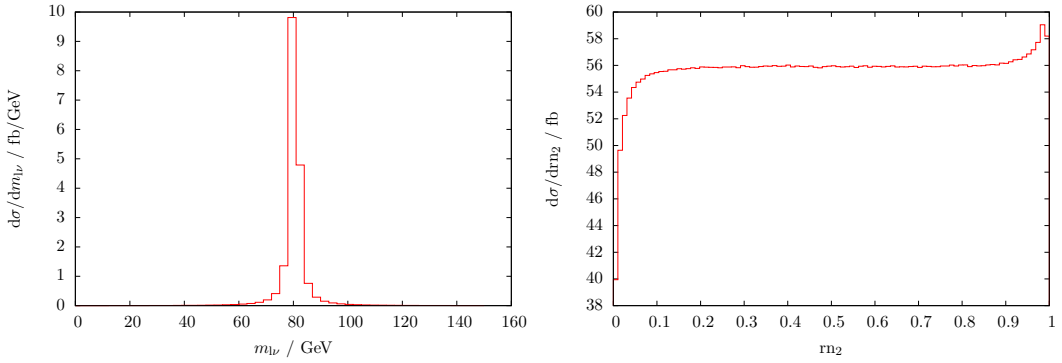

Figure 3.2: To show the effect of tan mapping as given in equation (3.4), for WH production, the invariant mass of the W (left) and random number describing it (right) are shown. While the mass follows a Breit-Wigner shape, the mappings leads to a nearly flat distribution of the corresponding random number. Hence, it is more suited for integration and optimization using VEGAS.

To get optimal sampling of this shape, a mapping for a uniformly distributed number can be derived. To do this, the inverse of the integral of the original function is required. Integrating $g(p^2)$ gives

$$G(x) = \int_{p_0^2}^{x} \mathrm{dp}^2\, \mathrm{g}(\mathrm{p}^2) = \frac{1}{\pi}\left(\arctan\left(\frac{\mathrm{M}^2 - \mathrm{p}_0^2}{\Gamma \mathrm{M}}\right) - \arctan\left(\frac{\mathrm{M}^2 - \mathrm{x}}{\Gamma \mathrm{M}}\right)\right). \tag{3.3}$$

The inverse of $G(x)$ then gives the optimal probability density for integrating this shape using a $[0,1]$ random number R. The invariant mass p^2 is then generated in the cutoff interval $[p_0^2, p_{\mathrm{max}}^2]$,

$$\begin{aligned} p^2 &= M\Gamma \tan(G_{\mathrm{min}} + (G_{\mathrm{max}} - G_{\mathrm{min}})R) + M^2, \\ &\text{where } G_{\mathrm{min}} = G(p_0^2), G_{\mathrm{max}} = G(p_{\mathrm{max}}^2)\,. \end{aligned} \tag{3.4}$$

This mapping is implemented in the *Resonance* function and allows general input values for M, Γ as well as upper and lower bounds on the invariant mass.

The effect of this mapping can be seen when considering the invariant mass p^2 of the final state W boson, which then decays into $l\nu$. In figure 3.2, the differential cross section in p^2 is shown, with the characteristic narrow peak at the W mass, as well as the differential cross section in the random number used. The tan mapping leads to a nearly flat distribution. Only the edges show a deviation, which corresponds to far off-shell production of the W boson. This also shows that the far off-shell region is stable.

3.2.2. WHj phase space

In WHj production, the leading order process consists of diagrams with a structure as shown in figure 3.3a. This structure is used to generate the phase space by choosing integration variables that are mostly independent and might have an (approximately) known shape.

The order in which the masses of off-shell particles and the momenta get chosen is designed to reflect typical variables used in experimental cuts, so that those cuts do not introduce correlations between those variables. The order is visualized in figure 3.3b. First the “central”

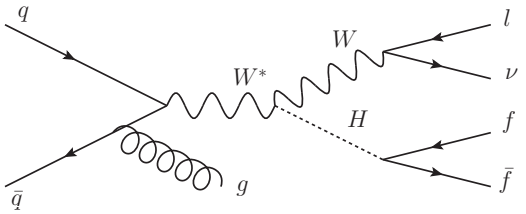

(a) Representative WHj LO diagram

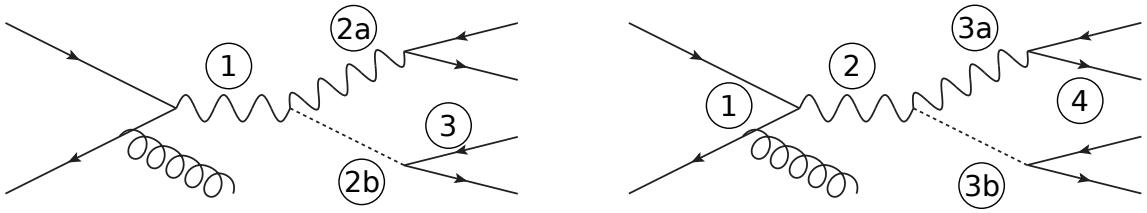

(b) Order of generation of a phase space point: In a first step, the invariant masses are generated in the order shown on the left side, then the momenta are generated in the order shown on the right side. A 2-particle Higgs boson decay is shown as an example. For the decay into 4 particles, the corresponding invariant masses and momenta are generated following the decay chain.

Figure 3.3: The generation of the phase space for WHj production is discussed based on a LO diagram.

element gets constructed, by generating the mass of the W* coupling to the quarks. This mass is mapped using the tail of a wide Breit-Wigner resonance. For large invariant masses, this corresponds to the propagator. Because of the small Higgs boson width, the intermediate W has an invariant mass larger than the on-shell mass, so that the invariant mass shows a wide peak around $m_{\mathrm{W}} + m_{\mathrm{H}}$.

In the next step, the masses of W and H get generated constraining them to have a sum below the W* mass, which is required for energy-momentum conservation in the WWH vertex. Depending on the H-decay channel, the decay particle masses are generated, fixing the masses of all massive particles.

With the masses fixed, the momenta are considered, starting with the QCD part by generating the momenta of the $2 \to \text{jets} + \mathrm{W}^*$ process. For real emission contributions, the generation of parton momenta cannot be easily restricted to values allowed by the cuts. Thus, first the momenta of the partons are generated and in a second step the jet algorithm is run and jet cuts are applied. The parton momenta give the proton momentum fractions x_1 and x_2 used in the PDFs.

Subsequently the W* momentum gets distributed to the final state particles. This is done following the cascade in the Feynman diagram figure 3.3b (right). On each $1 \to 2$ vertex, a boost into the restframe of the decaying particle is performed. In this reference frame, the energy components of the decaying particles momenta are fixed by their invariant masses. The direction of their momenta are generated using spherical coordinates. Thereby, both cuts on rapidity as well as angular correlations of the interactions are reflected in the integration variables. Distorting effects on angular distributions by boosts are mostly absorbed by this procedure so that the integration is stable. Each integration variable is mapped to a specific random number that is controlled by VEGAS to allow optimization as discussed in section 2.6.2.

Using the described method for the typical set of parameters used in chapter 5, approximately half of the generated phase space points pass all cuts and technical cutoffs. Additionally, the differential dependence of the cross section on the random numbers $\frac{\mathrm{d}\sigma}{\mathrm{d}rn}$ is rather flat. One example of this can be seen in figure 3.2. Also, the different distributions are flat in the sense that there are no variations over more than one order of magnitude and all variations are smooth. This behaviour facilities VEGAS to further optimize the integration.

This phase space gets used for all WH (j) processes, both at LO and NLO. The number of partons is adjusted as needed. For the real emission, one parton is added to the main $2 \to \text{jets} + \text{W}^*$ generation. At NLO, there is a new contribution: In the virtual amplitude, there are top-loops that couple the Higgs boson to a gluon instead of radiating it off a W. Those diagrams give only a small contribution as discussed in more detail in section 5.2.1. While the existing phase space generation does not map them perfectly, it is still sufficient to cover them well.

3.3. Leading order calculation

Counting the couplings of the electroweak sector (α) and strong sector (α_s), at LO the production of WH is $\mathcal{O}(\alpha^2)$ and WHj is $\mathcal{O}(\alpha^2\alpha_\mathrm{s})$. The inclusion of the leptonic decay of the W gives another factor α. The matrix element for WH and WHj is computed by separating the EW current and the QCD part of the diagram as described in section 3.1.2. Helicity amplitudes are used following the formalism of Ref. [40].

The EW current is calculated using HELAS routines [41] and code generated by MadGraph 4 [42], but modified to use a Cartesian polarization basis.

3.3.1. Higgs boson decays

For the Higgs boson several options were implemented. It can be produced as a final state particle, either on-shell (narrow width approximation) or off-shell with a Breit-Wigner shape factor.

The Higgs boson decays to $\mathrm{b\bar{b}}$, $\gamma\gamma$, $\tau\overline{\tau}$, $\mu\overline{\mu}$, $\mathrm{WW} \to l\nu\, l\nu$, $\mathrm{ZZ} \to ll\, ll$ and $\mathrm{ZZ} \to ll\, \nu\nu$ are also included. Because the Higgs boson is a scalar, the decays in its rest frame are isotropic. Two body decays can be calculated by multiplying the branching ratio on top of the production cross section of a stable Higgs boson. For the branching ratios the values implemented in the current VBFNLO version are used. Those reflect the current NLO and NNLO calculations.

For the decay to four leptons via two weak bosons, the full matrix element of the decay is calculated. Thereby, angular correlations are included. Also anomalous couplings are considered in those decays. The decay implementation is reused from VBF production in VBFNLO and was checked there.

User specific cuts can be used to restrict all final state particles in the different decay channels.

3.4. Next-to-leading order calculation

As discussed in section 2.3, the next-to-leading order calculation consists of two parts: the *virtual corrections* and the *real emission*. The following discussion is kept mostly general, but for the WHj process, specific parts are considered. The other implemented processes (W, Wj, WH) are simpler and use only a subset of the features of WHj so that all the possible issues are covered by WHj.

3.4.1. Renormalization and Counterterms

In the $\overline{\text{MS}}$ renormalization scheme the top-quark can be decoupled from the running of α_s. This leads to additional contributions to the counterterms for α_s and the wave function of the gluon. As shown explicitly in Ref. [43], those contributions cancel coincidentally for the case of one quark line with one external gluon attached.

3.4.2. Virtual amplitude

The virtual amplitude consists of all Feynman diagrams that are of one higher order in the coupling than the leading order contributions, but have the same number of external legs. Because the leading order diagrams are tree diagrams, the virtual contributions are one-loop diagrams. Two categories of diagrams are distinguished here. The first contains all diagrams where the Higgs boson is radiated off the W (figure 3.4). All those diagrams therefore share the same electroweak structure as the leading order diagrams. Because corrections appearing on the quark line go up to four-point functions (*boxes*), this category is called *boxline*.

The second category contains diagrams where the Higgs boson is attached to a top quark loop and therefore called *top-loop* (figure 3.6).

3.4.2.1. Boxline diagrams

The category *boxlineAbe* collects all virtual corrections to a quark line radiating a W boson and a gluon for a fixed order of the external legs. Thus, to build up the amplitude, the boxline routine is used twice with the different permutations of external particles. In addition, the *boxlineNoAbe* is used, which covers all diagrams with a triple gluon coupling. The names *boxlineNoAbe* and *boxlineAbe* refer to the fact that the latter case is also present in abelian gauge theories, while the former is not. The diagrams contributing to boxlineAbe and boxlineNoAbe are shown in figures 3.4 and 3.5, respectively. They include self-energy corrections, vertex corrections and box diagrams. Those contributions are calculated collectively using the boxline routines computed in Ref. [44]. The boxline routines were explicitly checked for several processes within VBFNLO.

The different colour structures in those diagrams can be explicitly extracted, such that gauge checks are implemented for terms $\propto C_A$ and $\propto C_F$ separately.

3.4.2.2. Top-loop diagrams

All virtual diagrams for WHj which have the Higgs boson attached to a top quark loop are classified here as *top-loops*. This top-loop mediates a gluon-gluon-Higgs (ggH) coupling, which can be thought of as the Higgs boson being radiated off the gluon instead of the W. In terms of the number of couplings, a WWH vertex is replaced by a same order of magnitude ttH vertex, which is given by the Yukawa coupling y_t. Examples of such diagrams are shown in figure 3.6. The gluon radiating the Higgs boson can be in either initial or final state.

The ggH coupling can be approximated by an effective vertex as often done in Gluon Fusion. Problems of this approximation are discussed in section 4.3.1. The top-loop diagrams were calculated using the routines for massive fermion loops from Ref. [45]. Bottom quark loops can also be included but are neglected by default as they contribute only at the level of $(m_b/m_t)^2 \lesssim 6 \cdot 10^{-4}$. Treating bottom quarks massive in this case would not directly conflict with the choice of n_f discussed in section 3.6, but bottom quarks should be treated overall consistently with the choice of n_f.

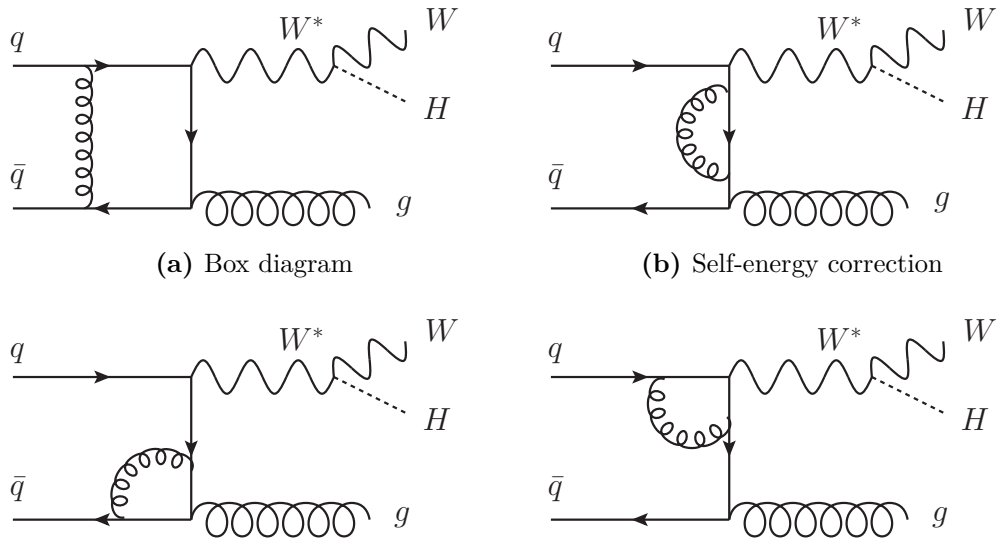

(a) Box diagram

(b) Self-energy correction

(c) Vertex corrections

Figure 3.4: The diagrams shown contribute to the virtual contribution of WHj (NLO) production and are calculated using the boxlineAbe routine. They always contain a quark line in the loop, such that the same diagram types would appear in a QED calculation.

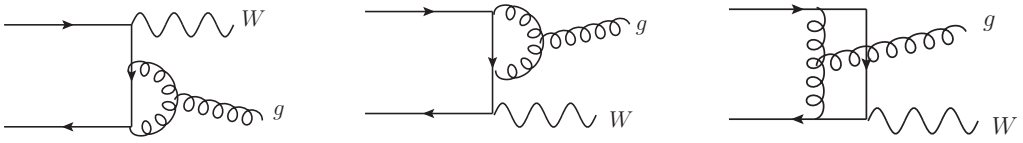

Figure 3.5: Diagrams with a triple gluon vertex are calculated with the boxlineNoAbe routine. They contain a triple gluon vertex and are thus specific to non-abelian gauge theories like QCD.

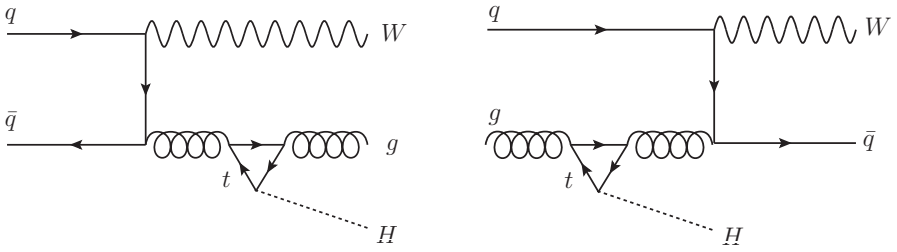

(a) Final state gluon

(b) Initial state gluon

Figure 3.6: The virtual contribution to WHj (NLO) production also contains diagrams, where the Higgs boson is not attached to the W boson, but attached to a top-loop. The Higgs boson is then not radiated off the W boson, but effectively off a gluon. This top-loop can appear for the gluon in both initial and final state.

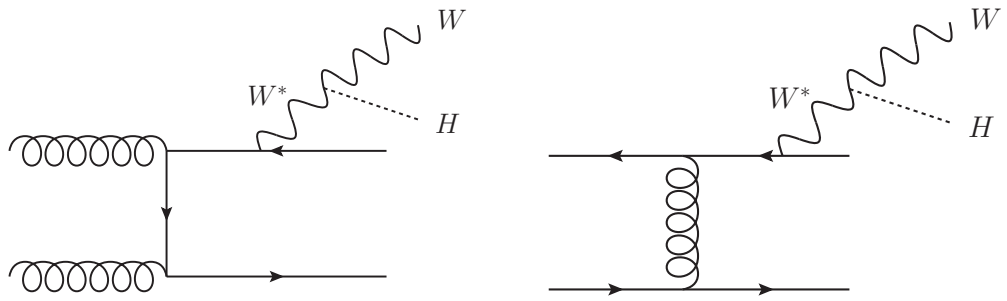

(a) *ggqq* type diagram **(b)** *qqqq* type diagram

Figure 3.7: The real emission for WHj production contains two classes of diagrams. Diagrams of with one quark line and thus two external gluons are called *ggqq* (left). With the gluons in the initial state this gives access to the large gluon PDFs. The *qqqq* diagram type consists of two quark lines (right).

3.4.3. Real emission and subtraction terms

As discussed in section 2.3, the real emission consists of all contributions with an additional QCD emission. Therefore, WHj (LO) gives the diagrams for the WH real emission and WHjj (LO) those for WHj.

For WHjj, there are two different types of diagrams depending on the type of the external QCD particles:

ggqq 2 gluons and 2 quarks connected by only one quark line

qqqq 4 quarks connected by two quark lines

The ggqq type allows a gluon-gluon initial state, which is favored by the PDFs in the low-energy regime, at small Feynman x. The ggqq contributions are about one order of magnitude larger than the qqqq ones. In the qqqq case there are some subtleties in including the CKM matrix, which are discussed in section 3.5.3.

In the Catani Seymour implementation using the method described in section 2.3.1, the *Real Emission* also includes the subtraction terms. The construction of subtraction terms is very general. They only depend on the QCD structure and, therefore, WH (+ n jets) can use the same subtraction terms as W (+ n jets). This allows to reuse already implemented subtraction terms from WA and WAAj.

The subtraction terms are constructed to smoothly approach the matrix element in the collinear and soft limit, thereby cancelling the divergences. This cancellation might become numerically unstable such that a technical cutoff is introduced. This cutoff requires all parton pairs to have an invariant mass above 0.1 GeV.

There are diagrams with the same final state as the real emission, but via an EW process instead of the QCD production. Example diagrams for this process are shown in figure 3.8. Those processes include Higgsstrahlung with an additional vector boson, as well as VBF Higgs boson production with another vector boson. While those diagrams formally replace one order of α_s with α, they could become large in special phase space regions. In this calculation, these diagrams are not included, as they are considered part of a different process, which includes an additional vector boson, which can decay hadronically..

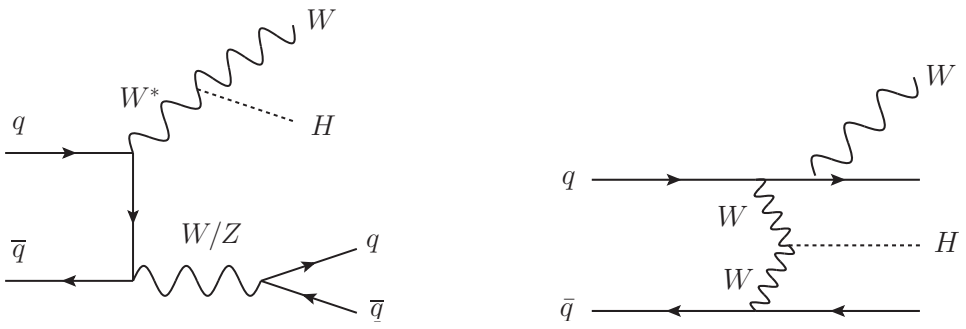

Figure 3.8: The WHjj final state can also be produced via an additional vector boson. Example diagrams for such a contribution are shown here. These diagrams are not included in this calculation.

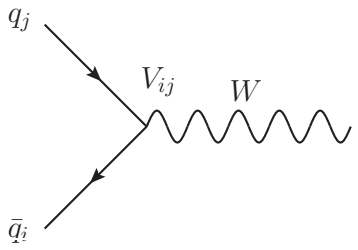

(a) CKM matrix element at Wqq vertex

$$\begin{pmatrix} V_{ud} & V_{us} & V_{ub} \\ V_{cd} & V_{cs} & V_{cb} \\ V_{td} & V_{ts} & V_{tb} \end{pmatrix}$$

(b) elements in the CKM matrix

Figure 3.9: The definition of the CKM matrix is given based on the Wqq vertex. Each matrix elements corresponds to a possible flavour combination.

3.5. CKM matrix effects

As introduced in section 2.1.2, in the EW sector of the Standard Model for quarks the interaction and mass basis do not coincide. They can be related by a unitary transformation, which is described by the Cabibbo-Kobayashi-Maskawa (CKM) matrix.

In calculations using Feynman diagrams and propagators, usually the mass eigenstates are chosen as a basis. Therefore, interactions with a W boson can change flavour. This is reflected in the Feynman rules that allow a W coupling to any combination of up- and down-type quarks and include the corresponding CKM matrix element. The CKM matrix and the vertex where its elements enter are shown in figure 3.9.

The CKM matrix is dominantly diagonal. This is best seen in the Wolfenstein parametrization [46]. In this parametrization, the existing hierarchies of the matrix elements are emphasised by expressing them in an expansion in $\lambda \approx \sin^2 \theta_c \approx 0.225$. The Wolfenstein parametrization and the current experimental values for the CKM are given in figure 3.10. Because the CKM matrix is mostly diagonal, the off-diagonal elements can be regarded as higher order effects and are often discarded in calculations.

When calculating Feynman diagrams separately for each flavour combination, there are 6 contributions (all up-down quark combinations of the first 5 flavours). Using a diagonal CKM matrix, those contributions reduce to two (generations), which are equal up to the PDFs used, such that only one matrix element has to be computed. Therefore, treating the CKM matrix diagonally not only reduces complexity but also CPU time.

$$\begin{pmatrix} 1-\lambda^2/2 & \lambda & A\lambda^3(\rho-i\eta) \\ -\lambda & 1-\lambda^2/2 & A\lambda^2 \\ A\lambda^3(1-\rho-i\eta) & -A\lambda^2 & 1 \end{pmatrix} \qquad \begin{pmatrix} 0.97427 & 0.22534 & 0.00351 \\ 0.22520 & 0.97344 & 0.0412 \\ 0.00867 & 0.0404 & 0.999146 \end{pmatrix}$$

(a) Wolfenstein parametrization

(b) current experimental values [47] (without complex phase)

Figure 3.10: The CKM matrix is mostly diagonal. This is exploited by the commonly used Wolfenstein parametrization, which expands the matrix elements in a small parameter λ. The currently known numerical values support the parametrization and show that the mixing between the first two generation is more than an order of magnitude larger than any mixing involving the third generation.

3.5.1. Including the CKM matrix using modified PDFs

The non-diagonal CKM matrix can be included in an efficient way that only requires minimal changes on an existing matrix element calculation, which so far does not include flavour information. This is done by moving the CKM matrix elements occurring in the calculation to the PDFs. This process will first be discussed on the basic case of one W boson coupling to one quark line and then expanded to Wj, WHj.

The collider cross section as discussed in 2.4.2 includes a sum over the quark flavours. The flavour dependence enters in the PDFs and the matrix element,

$$\sigma \propto \int_0^1 \mathrm{d}x_1 \int_0^1 \mathrm{d}x_2 \sum_{f_1,f_2} \mathrm{pdf}_{f_1,p}(x_1,Q) \cdot \mathrm{pdf}_{f_2,p}(x_2,Q) \left|\mathcal{M}(f_1,f_2,p_i)\right|^2 . \tag{3.5}$$

3.5.2. One quark line coupling to a W boson

For simplicity only the first two generations of quarks and diagrams with only one quark line with one W boson attached are considered. Effects of the third generation mixing are highly suppressed. The flavour dependence of the matrix element is only a factor of one CKM matrix element squared,

$$\left|\mathcal{M}(f_1,f_2,p_i)\right|^2 = V_{f_1 f_2}^2 \left|\mathcal{M}(p_i)\right|^2 . \tag{3.6}$$

This gives the full flavour dependence,

$$\sum_{f_1,f_2} \mathrm{pdf}_{f_1,p}(x_1,Q) \cdot \mathrm{pdf}_{f_2,p}(x_2,Q) \cdot V_{f_1 f_2}^2 . \tag{3.7}$$

This sum can be written explicitly. The shorthand $f_i \equiv \mathrm{pdf}_{f_i,p}(x_j,Q)$ is used, where f_i is one of the quark flavours u, c, t, d, s, b. For a general CKM matrix in the first two generations, this results in

$$\begin{aligned} & V_{ud}^2\, u\cdot\overline{d} + V_{us}^2\, u\cdot\overline{s} + V_{cd}^2\, c\cdot\overline{d} + V_{cs}^2\, c\cdot\overline{s} \\ &= u'\cdot\overline{d} + c'\cdot\overline{s} \qquad \text{with } u' = V_{ud}^2\, u + V_{cd}^2\, c, \qquad c' \text{ equivalently,} \\ &= u\cdot\overline{d}' + c\cdot\overline{s}' \qquad \text{with } \overline{d}' = V_{ud}^2\,\overline{d} + V_{us}^2\,\overline{s}, \qquad \overline{s}' \text{ equivalently.} \end{aligned} \tag{3.8}$$

Therefore, the CKM matrix factors can be absorbed into a rotation of the quark basis, effectively rotating the PDFs. There is a freedom in choosing whether up-type or down-type quarks are rotated. This freedom of choice will come in handy.

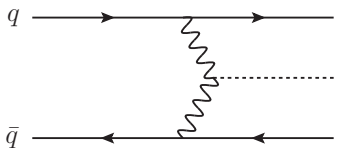

Figure 3.11: VBF diagrams only contain *initial-final* quark lines. They are therefore not affected by the transition from a diagonal to a non-diagonal CKM matrix, as discussed in the text.

Diagrams that have only one quark line can be organized in three categories, depending on whether the quarks are in the initial or final state: *initial-initial*, *initial-final*, *final-final*.

In the initial state, the matrix element is folded with the PDFs, so that the flavour information is important. In the final state, the quark flavour could be identified by flavour tagging in a detector, but for the four light flavours, this is generally not done.

Considering an *initial(f_1)-final(f_2)* diagram, the flavour dependence is

$$\sum_{f_1,f_2} \mathrm{pdf}_{f_1,p}(x_1, Q) \cdot V_{f_1 f_2}^2 \,. \tag{3.9}$$

The sum over f_2, using the unitarity property of the CKM matrix, collapses to a factor of 1 and reproduces the expression for a diagonal CKM matrix. The same effect can be made explicit by performing the basis rotation introduced in equation (3.8) and rotating the class of quark in the final state. This PDF is not used and therefore does not enter in the calculation but absorbs the CKM matrix element.

Analogously, the *final-final* diagrams are not affected by the CKM matrix. Thus, only one of the diagram categories is numerically affected by the CKM matrix: *initial-initial*. For the other two categories the CKM matrix does not have to be included.

This exclusion affects many processes and reduces the CKM matrix effect. For example, VBF processes as shown in figure 3.11 are independent of the CKM matrix. They only contain *initial-final* quark lines.

3.5.3. Effect on Wj and WHj production

The simple case of one quark line coupling to a W boson can be generalized to all diagrams occurring in WHj (NLO) production.

Diagrams with one quark line and one gluon are directly covered by the discussion above. Also the additional Higgs boson radiated off the W boson or the gluon does not affect the flavour dependence. Loop corrections do not introduce new external quarks, so that all virtual corrections effectively behave the same way as the Born case.

The only new issues appear in the real emission and subtraction. For the real emission, there are two types of diagrams as described in section 3.4.3: *qqqq* and *qqgg*. For the latter there is only one quark line, thus, it can be treated like the LO contributions. However, for the qqqq channel, there are two quark lines which need special treatment. Of these two, only the quark line with the W boson attached is relevant for the CKM matrix discussion, but with two quark lines there is the chance of interference between different diagrams. The potentially problematic interference terms are shown in figure 3.12.

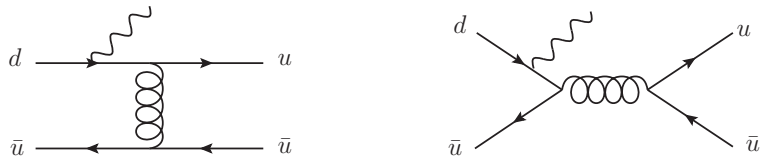

Figure 3.12: The real emission has interference terms between t-channel (left) and s-channel (right) diagrams. Those interference terms can lead to inconsistencies when flavour transitions are moved to the PDFs. For WHj production a consistent treatment using modified PDFs is nevertheless possible.

The s-channel diagram is of the *initial-initial* type and should use modified PDFs, while the t-channel only has *initial-final* quark lines and does not need modified PDFs. Just blindly using the rotated PDFs can also be problematic, because this can introduce spurious terms in the interference. In the flavour combination shown in figure 3.12, if the modified PDFs are used for the up-type quarks, the t-channel contains not only $d\overline{u} \to u\overline{u}$, but also some fraction of $d\overline{c} \to u\overline{c}$, while the s-channel gets $d\overline{c} \to u\overline{u}$, which has a different final state and therefore does not interfere.

These issues can be circumvented for the case of two quark lines with one W boson by using the modified PDFs for down-type quarks in the case of diagrams with 3 external up quarks and for up-type quarks in the case of 3 external down quarks. This preserves the separation of interfering and non-interfering diagrams, prevents CKM matrix element factors on diagrams that do not contribute and still allows factorizing the CKM matrix effects completely from the matrix element calculation, which only needs the quark charge information.

A similar procedure is in general also possible for other processes with more than one W boson coupling and a more complex QCD structure.

3.5.3.1. Numerical effect

To estimate the numerical effect, the case of mixing of the first two generations is considered. In that scenario the difference between one calculation including the cabibbo angle θ_c via $V_{ud} = \cos^2\theta_c, V_{us} = \sin^2\theta_c, \ldots$ another with the diagonal approximation is considered.

As described above the CKM matrix factors can be included in the PDFs which factorizes from the matrix element calculation. Therefore, the common matrix element is neglected and just the PDFs are considered. Then, the difference between the cross section with the CKM taken diagonally and one including CKM matrix effects is

$$\begin{aligned}
&\sigma_{\text{diag ckm}} - \sigma_{\text{with ckm}} \\
&\propto \left(u \cdot \overline{d} + c \cdot \overline{s}\right) - \left(\underbrace{V_{ud}^2}_{\cos^2\theta_c}\, u \cdot \overline{d} + \underbrace{V_{cd}^2}_{\sin^2\theta_c}\, c \cdot \overline{d} + \underbrace{V_{us}^2}_{\sin^2\theta_c}\, u \cdot \overline{s} + \underbrace{V_{cs}^2}_{\cos^2\theta_c}\, c \cdot \overline{s}\right) \\
&= \left(1 - \cos^2\theta_c\right) u \cdot \overline{d} + \left(1 - \cos^2\theta_c\right) c \cdot \overline{s} - \sin^2\theta_c c \cdot \overline{d} - \sin^2\theta_c u \cdot \overline{s} \\
&= \underbrace{\sin^2\theta_c}_{\approx 5\%} (u - c)\,(\overline{d} - \overline{s})\,.
\end{aligned} \tag{3.10}$$

So the effect of the CKM matrix is a pre-factor $\sin^2\theta_c \approx 5\%$ that is multiplied with two differences of PDFs. While the u PDF is significantly larger than the c PDF, both $\overline{d}$ and $\overline{s}$ are sea quarks and have similar (small) PDFs so that this factor gives an additional suppression.

Process	σ without ckm (fb)		σ with ckm (fb)		Rel. difference	
	LO	NLO	LO	NLO	LO	NLO
W^+H	55.72	76.28	55.27	76.00	-0.80%	-0.40%
W^+Hj	25.32	28.12	25.18	28.07	-0.50%	-0.20%

Table 3.1: The numerical effect on the cross section of including $V_{us} = V_{cd} = \sin\theta_c = 0.22535$ is shown. Following equation (3.10), the full calculation with off-diagonal matrix elements is smaller than the diagonal approximation. For all considered production processes, the cross section is changed by less then 1%.

This PDF suppression depends on the momentum fraction considered and therefore the phase space and is especially small for modest parton momenta at small Feynman x.

Effects involving the third generation of quarks will be proportional to the off-diagonal elements V_{qb}^2 and V_{tq}^2 which are smaller than 0.2% leading to an additional factor 20 suppression compared to the mixing of the first two generations. Therefore it is safe to neglect any third-generation CKM matrix effects.

The use of realistic input parameters and the cuts discussed in section 5.1 leads to a numerical effect on the total cross section below 1%. The effect on the LO and NLO cross section of WH and WHj is given in table 3.1.

Including the cabibbo angle therefore reduces the cross section between 0.8% for WH (LO) down to 2 ‰ for WHj (NLO). This effect is at the order of the above mentioned estimation. Because of the small size of the correction, the off-diagonal CKM matrix is not included in further numerical results if not stated explicitly.

3.5.3.2. Effect on distributions

The effect of including the CKM matrix on differential distribution in WHj is small. Within the phase space region dominating the cross section, the effect of the CKM matrix is rather flat and in general is smaller than other theory uncertainties. The effect of including the CKM matrix on several distributions is shown in figure 3.13. There, the ratio of the differential cross section with and without the inclusion of the CKM matrix is plotted. The values for the CKM are given in appendix A. There are regions where the CKM matrix effect is enhanced. Those correspond to large x in the PDFs. In figure 3.13 also the energy of the final state parton is plotted, which shows an increased CKM dependence in the high energy region, where the effect can reach 2-3%.

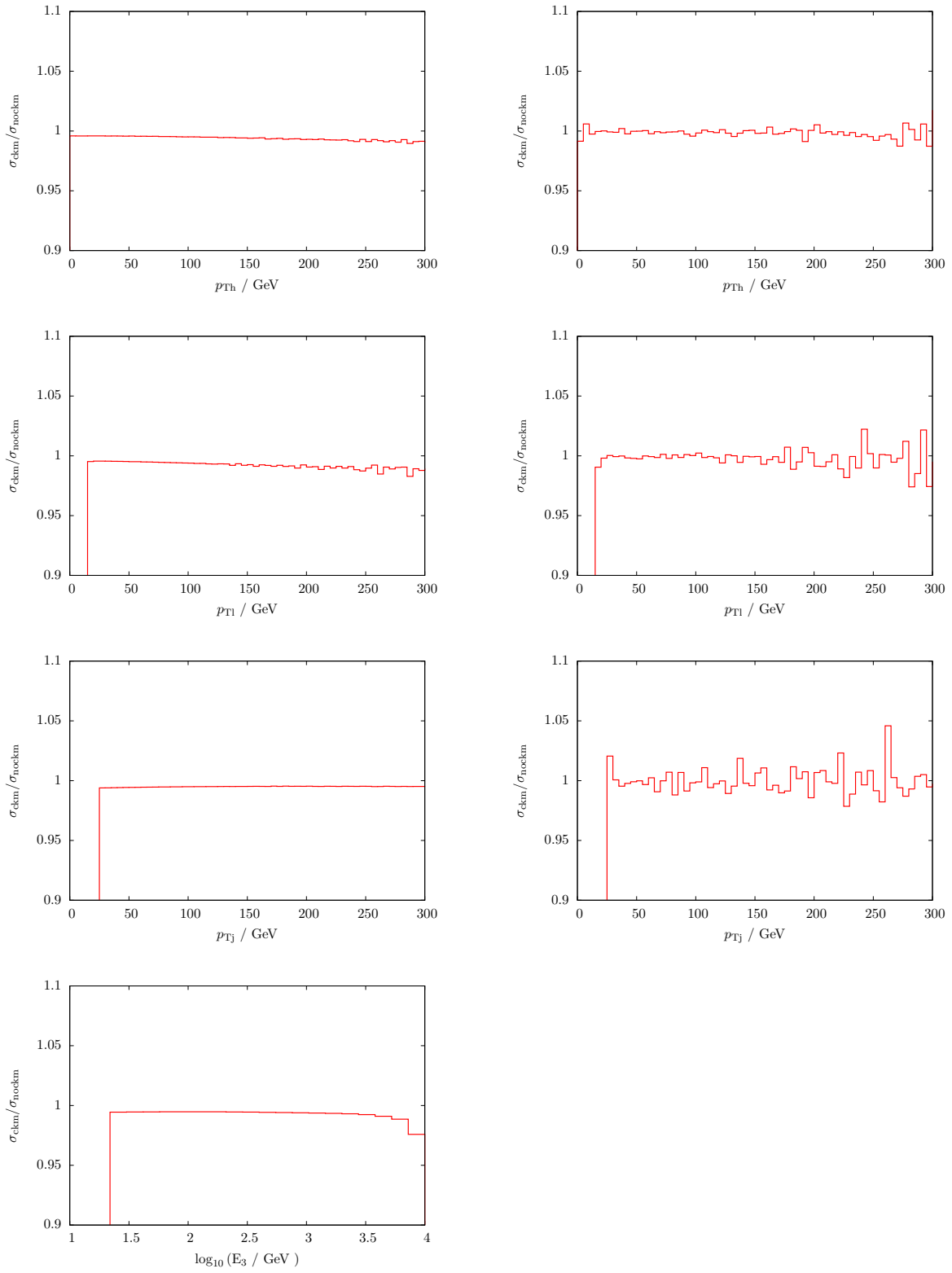

(a) LO **(b)** NLO

Figure 3.13: For several variables the effect of including a non-diagonal CKM matrix compared to the diagonal approximation is shown. The p_{T} distributions of the Higgs boson, the W decay lepton and the hardest jet are essentially flat. For very large final state parton energies, the effect of a non-diagonal CKM can increase to 2-3%.

3.5.4. Checks

Several checks were performed to verify the correct implementation of the CKM matrix. Only flavour changing interactions between the first two generations were considered for calculations and checks.

The following checks were performed:

- Disabling the CKM matrix input or choosing the identity restores the result without CKM.
- When setting the PDFs of all generations equal, random choices of orthogonal matrices for the CKM matrix lead to the same cross section.
- To check that non-symmetrical choices are treated correctly: When setting the c quark PDF to 0, introducing a small V_{us} raises the cross section, introducing a small V_{cd} does not.
- At the cross section level agreement was found with MCFM (WH NLO) and Sherpa (WH, WHj LO). This can also be seen in tables 4.1 and 4.2.

3.6. Flavour scheme – $n_\mathrm{f} = 4$ or 5

In QCD calculations, especially those involving loops, a common assumption is to treat quarks as massless particles. For all QCD interactions this creates a symmetry between the different quark flavours. Then a process is not defined for individual flavours, but on the basis of quarks or partons. The number of active flavours in the calculation is called n_f.

Treating massive particles massless is only a good approximation if their mass is small compared to the scale of the interaction. This scale is not a fixed value but only an order of magnitude so that there is a certain ambiguity in the cutoff. For the process at hand, deviations due to neglected masses would come as factors of m_q/μ depending on the process scale μ.

For usual events at the LHC, considering d,u,s and c massless is considered a good approximation ($m_\mathrm{q} \leq m_\mathrm{c} \approx 1.3\,\mathrm{GeV}$). The top quark ($m_\mathrm{t} \approx 173\,\mathrm{GeV}$) is too heavy and requires special treatment. Internal quark loops can be calculated using massive propagators. Often mass limits are used, like the heavy-top limit, which is discussed in section 3.4.2.2. In the initial state top quarks are neglected as due to their mass they are not relevant in PDFs. Final state top quarks decay and can be detected. They can be distinguished from a light jet so that processes with final top quarks can be separated from other final state partons.

This leaves two possible choices for n_f: 4 or 5. In other words, the only remaining choice is whether to treat the bottom quark as massive or massless.

There is no general best choice, but for most processes one of the two is favored.

3.6.1. Consistent choice of n_f

The dependence on n_f appears in:

- external quark lines (initial and final)
- PDF set, PDF counter terms
- running of α_s, counter terms

- quark loops
- Catani-Seymour: subtraction terms, I,P,K terms

All those occurrences are interrelated. Choosing n_f in one of them fixes all others. Using a different n_f will lead to inconsistencies, as one of the relations as discussed in the following will be broken.

At LO there are no b quarks present in the discussed processes because a top quark would appear. They can only enter at NLO. There, they are introduced in the splitting of a gluon in a $\mathrm{b\bar{b}}$ pair as part of the real emission. The real emission and the subtraction terms are calculated using the construction by Catani and Seymour, which relates the number of flavours in the real emission splitting to two parts of the calculation.

On the one hand, n_f appears in the I-operator in the splitting of a gluon into a quark pair. This is constructed to cancel the divergences in the virtual contribution, hence, n_f in quark loops is fixed. This also sets the counter terms, which are constructed based on loop diagrams and therefore the running of α_s.

On the other hand, the gluon splitting appears in the finite P, K terms of the Catani Seymour construction. The P operator also contains a part $\mathrm{d}\sigma_c$, which describes corrections to the PDFs. Thus, the PDF set has to match the n_f used in the real emission. The PDFs usually provide a running of α_s based on their fit, which relates back to the n_f in the virtual contribution.

Therefore, all occurrences of n_f are connected and choosing different values for n_f in different terms is inconsistent and leads to an over- or underestimation of the result.

3.6.2. Problems and features of four- and five-flavour scheme

With $n_\mathrm{f} = 4$, there are no initial state b quarks. In the final state there could be massive b quarks, but they would only be generated in pairs. Processes with an odd number of final state b quarks, thus, have unresolved additional b quarks. Processes which require final state b quarks might lead to large terms of the form $\log q^2/m_\mathrm{b}^2$ which are resummed in a five flavour calculation.

The default choice of n_f in current PDF sets (CTEQ, MSTW, ...) is 5. For a pure QCD calculation or one involving only neutral currents this is the common choice. With charged currents a W coupling to a b quark would lead to a top quark. Initial top quarks are not given by the PDFs and final top quarks can be tagged by their decay so that the process is not counted as a normal jet. Therefore, in processes with one W coupling the corresponding quark line should not include b quarks, but other quark lines in the diagram might.

In five-flavour calculations, external bottom quarks are often restricted. For example in Refs. [48, 49], b quarks in the initial state are neglected due to the "smallness of their PDFs" and b quarks in the final state are only included if a $\mathrm{b\bar{b}}$ pair is recombined into one jet. This procedure correctly treats all occurrences of n_f related to divergent structures, but neglects the contribution of b quarks in finite terms. Those terms are expected to be small and of comparable size as the difference between $n_\mathrm{f} = 4$ and $n_\mathrm{f} = 5$.

3.6.3. Implementing external b quarks

The existing code for WAAj only included four external quark flavours. Several changes were made to add external b quark. The only part affected is the real emission of WHj (and Wj). In that case there are diagrams with two quark lines (called qqqq in section 3.4.3). The quark

n_f	final state b quarks	cross section (fb)		deviation from full $n_f = 5$	
		LO	NLO	LO	NLO
4	none	26.410	28.891	−1.1%	−1.6%
5	all	26.724	29.359		
5	none	26.724	28.451		−3.1%
5	one jet	26.724	28.737		−2.1%

Table 3.2: The cross sections for W^+Hj production with $n_f = 4$ and $n_f = 5$ are shown. For the latter different simplifications for the real emission are shown, which either exclude all final state b quarks or only include them if they are recombines into one jet. The cuts given in equation (5.1) are used. The difference between $n_f = 4$ and $n_f = 5$ is 1.1% at LO and 1.6% at NLO. However, an inconsistent treatment of external b quarks enhances this difference at NLO to 2% or 3% respectively.

line which does not have a W attached can then also be a b quark, adding two external b quark legs.

There are also additional subtraction terms for b quark diagrams, where the corresponding Born diagram has the b legs recombined to a gluon. This can only be divergent (and therefore require a subtraction term) if at least one b leg is in the final state and a b leg can never be an observer parton. Additionally, finite collinear terms corresponding to the splitting of an initial b into b and gluon have to be included.

3.6.4. Comparing and merging four and five flavour schemes

When comparing four and five flavour scheme, it is important to use comparable setups. While one is required to use different PDF sets, they should come from the same family with the same assumptions and prerequisites for the fit, such that only the change due to n_f is considered. Some PDF sets (e.g. CTEQ6) only include a specific flavour version so that they are not suitable for comparisons.

On the PDF side, the state-of-the-art is no longer Fixed Flavour Number, but generalized schemes whose number of active flavours depends on the scale. An overview of the current schemes is given in Ref. [50].

In a calculation to all orders in perturbation theory both schemes should converge. Having both approaches allows for a comparison and an estimation of the remaining uncertainty. Calculating higher order corrections is usually easier in one of the schemes, such that calculations exist only in one scheme, e.g. four flavour for single top (NLO) [51], five flavour for $b\bar{b}h$ (NNLO) [52].

The cross section of W^+Hj (NLO) production for different versions of $n_f = 4$ and $n_f = 5$ are given in table 3.2. For this comparison the MSTW2008 PDF sets [53] were used. The full calculations in both flavour schemes only deviate by 1.1% at LO and 1.6% at NLO.. However, neglecting all external b quarks or only considering them if they are combined into one jet, can reduce the NLO cross section by 2-3% compared to the full $n_f = 5$ calculation. For the calculation without external b quarks, the corresponding subtraction terms are removed.

CHAPTER 4

CHECKS

In order to ensure the correctness of the implemented processes, several checks have been performed. They are documented in this chapter:

LO matrix element, section 4.1 At LO the matrix element was checked against the automatically generated MadGraph matrix element for individual phase space points.

LO cross section, section 4.2 The cross section for all LO processes was checked against Sherpa.

Virtual contributions, section 4.3 Several properties of the virtual amplitudes were used for checks. The NLO calculation allows to check for violations of gauge symmetry, as well as the reproduction of some analytical results. The top-loop type diagrams were checked against an external implementation.

Subtraction terms, section 4.4 Cancellations expected by the chosen subtraction mechanism can be checked explicitly.

NLO cross section, section 4.5 The NLO cross section for WH was checked against MCFM, as well as against VH@NNLO. The NLO cross section of Wj was also checked against MCFM.

previous NLO results, section 4.5.3 The results for WHj were compared to an existing calculation for on-shell WHj production.

The production of $W^+H(j)$ and $W^-H(j)$ are very similar and are in general referred to as WH(j). Checks were always performed for both cases, but for consistency numerical results in this chapter are by default given only for $W^+H(j)$.

Process	VBFNLO (fb)	Sherpa (fb)	rel. difference
W^+H (LO)	55.721	55.741	−0.03%
W^+Hj (LO)	25.322	25.312	+0.04%
W^+Hjj (LO)	10.718	10.713	+0.06%
W^+Hjj, H→WW (LO)	0.017208	0.017210	−0.01%
W^-Hj (LO)	14.502	14.503	−0.01%
W^+H (LO, ckm)	55.273	55.292	−0.04%
W^+Hj (LO, ckm)	25.182	25.180	+0.01%
W^+Hjj (LO, ckm)	10.685	10.678	+0.06%

Table 4.1: The LO cross sections are compared between Sherpa and the implementation into VBFNLO performed as part of this thesis. Agreement is found for all compared processes within the statistical accuracy below 1‰. Here a selection of representative processes is shown. The fundamental process discussed is W^+H with up to two jets. Additionally, Higgs boson decays are included and were checked. Also the implementation of the CKM matrix gives agreement at all implemented jet multiplicities, with deviations below 1 ‰.

4.1. LO matrix element

MadGraph [42] allows the generation of general LO matrix elements. Those can be computed for individual phase space points and compared to our implementation. The helicity basis used by MadGraph differs from the one used in VBFNLO. Therefore, the correct helicity combination has to be considered. The implementation of the matrix elements of W, Wj, WH, WHj were compared with the code generated by MadGraph. For all checked points the relative difference was below 10^{-10}. This check is independent of the phase space integration and the optimizations involved. This explains the high accuracy of the comparison.

4.2. LO cross section

At LO the cross section was checked against Sherpa [54]. Sherpa allows the automatic calculation of cross sections including cuts and particle decays. The calculation is based on the matrix element generators Amegic and Comix. Amegic was found to behave badly for high multiplicity final states and therefore Comix was used. A selection of the compared cross sections is given in table 4.1. Agreement better than 1‰ is found.

The Wjj (LO) cross section was checked against an implementation by Matthias Kerner [55]. This implementation allows runs with both $n_f = 4$ and $n_f = 5$. Agreement was found for both flavour schemes within the statistical uncertainty.

4.3. Virtual contributions

Comparing the NLO matrix element is less trivial than the LO one, because of the different existing subtraction schemes and some ambiguities about moving terms between *virtual* and *real* contribution. Thus, no check of the NLO matrix elements was performed. However, many internal checks as well as comparisons of the cross section as explained in the following sections were completed.

4.3.1. Top-loops

The top-loop diagrams were compared at the matrix element level against MadGraph. MadGraph automatically generates code for the matrix elements. This is possible not only for the SM but also for several other theories. MadGraph includes one extension of the SM which includes effective Hgg and H$\gamma\gamma$ vertices. These vertices are constructed by evaluating the loop integral in the limit of $m_\mathrm{t} \to \infty$ also called *heavy top limit*. The vertices are approximated by a Taylor series in q^2/m_t^2, which allows more accuracy than only the leading term for a Higgs boson mass below $2m_\mathrm{t}$.

This allows the automatic generation of both born and top-loop diagrams. Therefore, not only the top-loop contributions can be compared, but also the relative sign between born and top-loop diagrams can be checked. The heavy top limit assumes that the top mass is the highest scale in the calculation. This assumption is phase space dependent and breaks down easily.

As can be seen in figure 3.6 one of the gluons is off-shell. The q^2 can be of the order of the $\hat{s}$ of the process, which implies $|q^2| > m_\mathrm{t}^2$. In most regions of phase space, q^2 is at a few hundred GeV and therefore the heavy top limit no longer holds.

For a comparison with MadGraph several special parameter choices were considered to ensure the validity of the heavy top limit approximation and therefore the correctness of the MadGraph result:

- heavy top: Setting $m_\mathrm{t} = 1000 \cdot m_\mathrm{t,physical}$ restores the required scale hierarchy. In this limit the agreement between the implementation for this thesis and MadGraph is at the level of 10^{-6}. This test includes points of all regions of phase space.
- light gluon: Leaving the top mass at its physical value, one can limit the virtual gluon to be rather light. Requiring $\sqrt{q^2} < 150\,\mathrm{GeV}$ cuts away many points, but the remaining ones have m_t as the highest scale. Then, the agreement is at the level of 10%
- light Higgs boson: The gluon q^2 must be larger than m_h^2. Hence, to reduce it, a light Higgs boson with $m_\mathrm{h} = 20\,\mathrm{GeV}$ can be considered. This allows virtualities of $\sqrt{q^2} < 50\,\mathrm{GeV}$. For those, the agreement with MadGraph is at the level of 1%.

4.3.2. Gauge test and Ward identities

When checking the numerical result of a matrix element calculation, there are many symmetries and properties that can be exploited. One that is very useful is the gauge symmetry.

Gauge symmetries leave an unphysical degree of freedom in the theory on which no physical observable should depend. This can be used in analytical calculations by introducing a gauge fixing term and confirming that this choice of gauge cancels out in all calculated observables.

In a numerical calculation a set of identities called *Ward identities* are useful. For tree level amplitudes, those imply that the amplitude with the polarization vector of the gluon replaced by its momentum vanishes,

$$\mathcal{M}|_{\epsilon_\mu \to p_\mu} = 0\,. \tag{4.1}$$

This equality not only holds for the full matrix element, but also for gauge-invariant subsets of diagrams. Testing this equality therefore checks whether there is a mistake in the implementation that would violate gauge invariance.

For loop diagrams, there are related identities, that express an n-point function contracted with the momentum by a difference of $(n-1)$-point functions. In WHj production, box contributions can be reduced to a difference of vertex corrections.

The box diagram calculation involves a loop integral of the form

$$\begin{aligned}\mathcal{D}_{\mu_2\mu_3}(p_1,p_2,p_3,p_4) = \int \frac{d^dq}{(2\pi)^d}\frac{1}{q^2}\overline{u}(p_{13})\gamma^\alpha \frac{1}{\not{q}+\not{p}_{13}}\gamma_{\mu_3}\frac{1}{\not{q}+\not{p}_{12}}\gamma_{\mu_2}\frac{1}{\not{q}+\not{p}_1}\gamma_\alpha \overline{u}(p_1),\\ \text{where } p_{13}=p_1+p_2+p_3,\ p_{12}=p_1+p_2.\end{aligned} \tag{4.2}$$

For the matrix element calculation this has to be contracted with the polarization vectors. Instead contracting with the momentum allows to cancel propagators and rewrite the expression as

$$\begin{aligned}p_2^{\mu_2}\mathcal{D}_{\mu_2\mu_3}(p_1,p_2,p_3,p_4) =& \left[(p_2+p_1+q)^{\mu_2}-(p_1+q)^{\mu_2}\right]\mathcal{D}_{\mu_2\mu_3}(p_1,p_2,p_3,p_4)\\ =&\mathcal{C}_{\mu_3}(p_1,p_2+p_3,p_4)-\mathcal{C}_{\mu_3}(p_1+p_2,p_3,p_4)\end{aligned} \tag{4.3}$$

The vertex corrections $\mathcal{C}_{\mu_3}$ are proportional to the Born matrix element, which allows a comparison to the leading order calculation.

Furthermore, the different color structures of the gluon attached inside the loop $(C_F - C_A/2)$ and the gluon outside the loop (C_F) can be separated and checked individually. Those relations were explicitly calculated in Ref. [44].

The Ward identity also allows to control numerical instabilities. This can be done by constructing a "normalized zero". $\mathcal{M}$ is split in two parts of about similar size and the Ward identity is checked as

$$\begin{aligned}&\mathcal{M}|_{\epsilon_\mu\to p_\mu} = 0\\ \Leftrightarrow\quad &\mathcal{M}_1|_{\epsilon_\mu\to p_\mu} + \mathcal{M}_2|_{\epsilon_\mu\to p_\mu} = 0\\ \Leftrightarrow\quad &\frac{\mathcal{M}_1|_{\epsilon_\mu\to p_\mu}}{\mathcal{M}_2|_{\epsilon_\mu\to p_\mu}} + 1 = 0\end{aligned} \tag{4.4}$$

Using this *normalized zero* is useful because calculating the left-hand side of equation (4.4) gives the relative difference from zero compared to the size of the matrix element. In figure 4.1, a histogram of the accuracy of the gauge test is shown. Most points are calculated with 13 digits of accuracy. In the sample of 10^5 points none had less than 7 digits of accuracy and only 10 points were at the level of 8 digits. Since the NLO corrections are about 40% of the LO cross section, it is sufficient to require 2-3 digits of accuracy for the amplitude, to get a total cross section with a ‰ accuracy. For this setup no unstable points were found. For all processes implemented in this thesis the identities are fulfilled for the matrix elements used within the numerical accuracy.

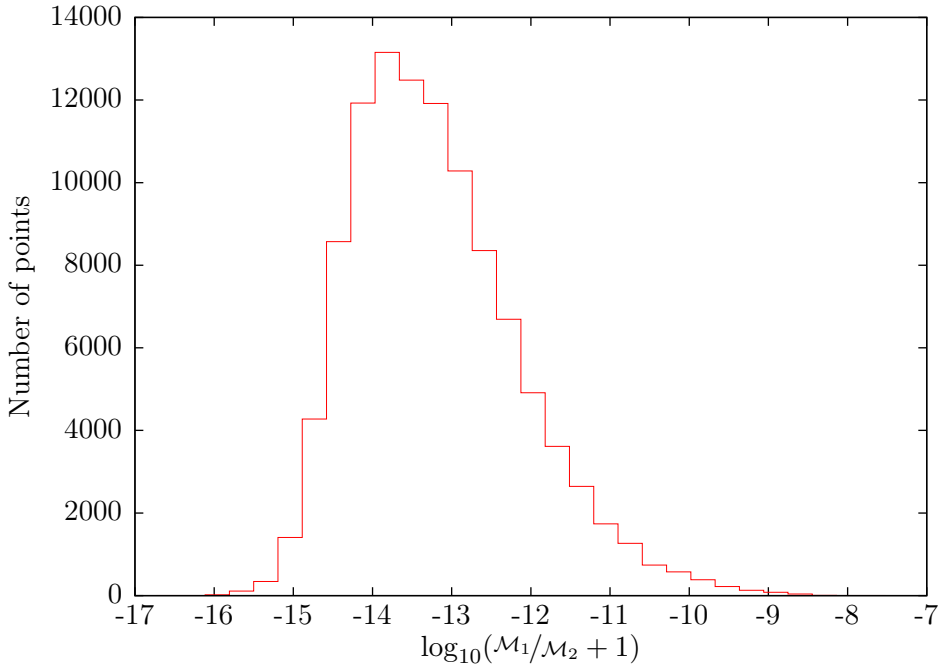

Figure 4.1: A histogram of the accuracy of the gauge test for the virtual amplitude in W^+Hj production is shown. Most phase space points fulfill the gauge test with an accuracy of 13 digits. All points in this sample have an accuracy of at least 7 digits, which is well below the level of 2-3 digits required for a stable result of the cross section at the ‰ level.

4.3.2.1. ϵ poles

The virtual contributions contain pole structures as discussed in section 2.3.1. Those can be expressed as terms proportional to $1/\varepsilon$ and $1/\varepsilon^2$. These divergent terms are known and they are proportional to the Born matrix element. The finite term is called $\widetilde{\mathcal{M}}$. Using this, the virtual matrix element can be written as

$$\mathcal{M}_{\mathrm{V}} = \text{couplings} \cdot \left(\widetilde{\mathcal{M}}_{\mathrm{V}} + \left(\frac{4\pi\mu_R^2}{-s} \right)^{\epsilon} \Gamma(1+\epsilon) \left[-\frac{a}{\epsilon^2} - \frac{b}{\epsilon} \right] \mathcal{M}_{\mathrm{V}}^{\mathrm{B}} \right), \quad s = (p_1 + p_2)^2. \tag{4.5}$$

The divergent terms can be checked using the known prefactor and $\mathcal{M}_{\mathrm{Born}}$. Agreement within the numerical accuracy is found. Additionally, this check tests whether both virtual and born amplitude use the same couplings and momenta.

4.3.2.2. Reparametrization invariance

The prefactor of the pole terms in equation (4.5) depends on s, the square of the center-of-mass energy. Considering $-s$ as an independent scale μ_0, ${\mu_0}^{\varepsilon}$ can be expanded in ε, which leads to an additional finite term proportional to the Born matrix element [44].

$$\widetilde{\mathcal{M}}'_V = \widetilde{\mathcal{M}}_V(\mu_0) + f(\mu_0)\, \mathcal{M}_V^{\mathrm{B}} \tag{4.6}$$

Then $\widetilde{\mathcal{M}}'_V$ is independent of μ_0. This can be checked by calculating the matrix element for the same phase space point with different choices of this scale μ_o and comparing the corresponding

$\widetilde{\mathcal{M}}'_V$. Checking with $\mu_0 = -s$ and $\mu_0 = 1\,\text{GeV}$ gives agreement at the order of 10^{-12}. This test is important as it directly checks the algebra for some finite terms in $\widetilde{\mathcal{M}}_V$.

4.4. Subtraction terms

The subtraction scheme described in section 2.3.1 was introduced to cancel the divergences in the collinear and soft regions of the phase space. These cancellations approach the limit smoothly, so that they can be seen in the respective regions. Interesting variables for the soft limit are the energy E_i of a final state parton and for the collinear limit $p_i \cdot p_j$, where at least one parton is in the final state. The cross section contains contributions from the real emission $\mathrm{d}\sigma^R$ and the subtraction terms $\mathrm{d}\sigma^A$,

$$\mathrm{d}\sigma_{m+1} = \mathrm{d}\sigma^R - \mathrm{d}\sigma^A\,. \tag{4.7}$$

The born kinematics of the subtraction terms are derived from the real emission kinematic by combining two partons. There are 11 possible kinematics for WHj. For this calculation the implementation of Ref. [39] is used.

The cancellation of real emission and subtraction terms can be seen in the histogram shown in figure 4.2. This histogram shows contributions to the total cross section in the collinear region of p_2 and p_4. In the limit of small $p_2 \cdot p_4$ the distribution smoothly vanishes. There is a technical cutoff to reduce numerical instabilities, requiring $m_{24} > 0.01\,\text{GeV}^2$. The difference between real emission and subtraction terms is negligible at that scale.

To test the cancellation of the real emission contribution, one can compare the subtracted with the unsubtracted result for phase space points in the infrared limit. With the real emission as normalization this difference is

$$R \equiv \frac{\mathrm{d}\sigma^R - \mathrm{d}\sigma^A}{\mathrm{d}\sigma^R}. \tag{4.8}$$

The ratio R given above is shown in figure 4.3 for the phase space region where p_1 and p_4 are collinear. Because the subtraction terms are also subject to phase space cuts, artifacts can appear in the cancellation. Requiring all subtraction kinematics and the real emission to pass the cuts, leads to the cancellation shown in figure 4.3a. If only the real emission has to pass the cuts, there might be points where all subtraction terms fail the cuts leading to $R = 1$. There are also points, for which only one of the two subtraction terms corresponding to this collinear region passes the cuts. This leads to lines at 1 and $1/2$, which can be seen in figure 4.3b. In the collinear limit the real emission and the subtraction terms grow and cancel each other. However, differences of two large terms can lead to numerical instabilities. Thus, a cutoff is introduced in the phase space generation as discussed in section 3.2.

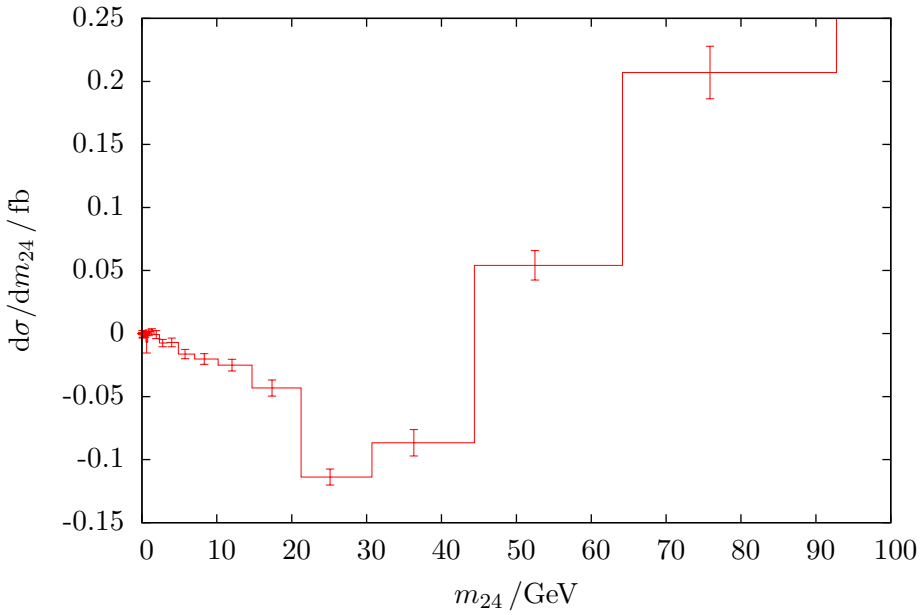

Figure 4.2: This histogram shows the cancellations between real emission and subtraction terms for W^+Hj production. The differential cross section for the invariant mass $m_{24} = 2p_2p_4$ between a final and initial state parton is shown. A small invariant corresponds to the partons being collinear. In this region the real emission approaches the subtraction terms, such that their sum smoothly goes to zero.

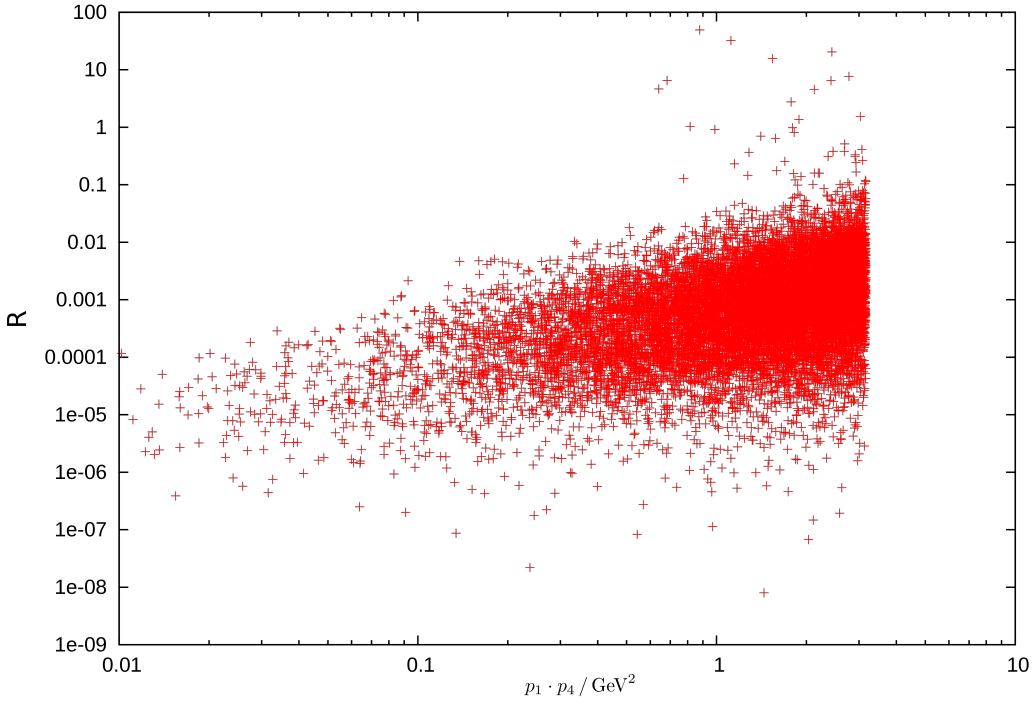

(a) Requiring all kinematics to be included

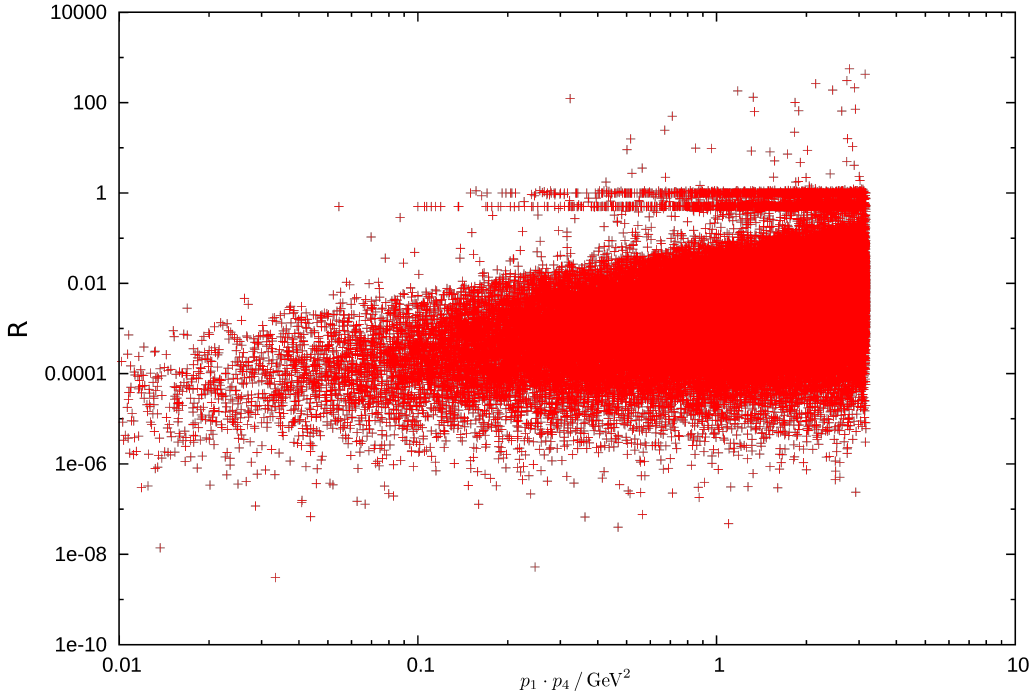

(b) Including also points where only some kinematics pass the cuts

Figure 4.3: The cancellation of real emission and subtraction terms in the collinear region is shown. The subtraction terms constructed following the method of Catani and Seymour leads to a smooth cancellation. When phase space points are included, which did not pass the cuts for some kinematical combination, artifacts appear, which are discussed in the text in more detail.

Process		VBFNLO (pb)	MCFM (pb)	Rel. difference
W^+ (LO)		5320.8	5320.9	-0.001%
W^+ (NLO)		6589.9	6588.6	-0.019%
W^+j (LO)		901.4	903.0	-0.17%
W^+j (NLO)		1221.4	1221.7	-0.023%
W^+j (LO)	$p_{\mathrm{T}j} > 50$	339.2	339.8	-0.17%
W^+j (NLO)	$p_{\mathrm{T}j} > 50$	426.0	426.0	-0.01%
W^+H (LO)	mcfmcuts	0.34126 / BR	0.34129 / BR	-0.01%
W^+H (NLO)	mcfmcuts	0.44601 / BR	0.44672 / BR	-0.16%

Table 4.2: The cross sections calculated are compared with MCFM. For Wj (NLO) and WH (NLO) production, agreement is found at the level of 2‰. For the WH comparison the default cuts used by MCFM were used, which are given in equation (4.9). For W^-j and W^-H production agreement is also found at the ‰ level.

4.5. NLO cross section

4.5.1. MCFM

MCFM provides NLO implementations of the production of a W boson with up to two jets as well as WH production [56]. Wj (NLO) production is the most interesting comparison as it checks the total NLO cross section and covers the majority of the code also used for WHj (NLO) production.

The cross sections are in general calculated using the parameters and cuts in section 5.1. For Wj production an additional run with $p_{\mathrm{T}j} > 50\,\mathrm{GeV}$ instead of 30 GeV is performed. The five flavour scheme is used. For the comparison of WH production with MCFM, their default cuts and EW parameters were used, which do not include cuts on leptons. The values used are

$$\begin{aligned} &\mathrm{R_{jj}} = 0.5, \text{anti-}k_T\text{-alg.}\,, \quad p_{T,j} = 15\,\mathrm{GeV}\,, \quad |\eta_j| < 3\,, \\ &\mu_R = \mu_F = 80\,\mathrm{GeV}\,, \qquad \sqrt{s} = 8\,\mathrm{TeV}\,. \end{aligned} \tag{4.9}$$

As shown in table 4.2 agreement is found with a relative difference below 2 ‰. While the statistical error claimed can be even smaller, the technical cutoffs and differences in the implementation might introduce differences at the ‰ level.

To test the implementation of Wj (NLO) production even in numerically difficult and unphysical regions, a comparison with MCFM for extreme scales (10 GeV and 1000 GeV) was performed. Both LO and NLO agree up to better than approximately 2 ‰. The numerical results are given in table 4.3. These extreme scales test all scale dependent parts of the calculation including especially finite terms of the NLO calculation. The WH implementation in MCFM also allows to include off-diagonal CKM matrix elements and agrees with this calculation at the ‰ level.

4.5.2. vh@nnlo

The program *vh@nnlo* [57] allows the computation of the integrated cross section of WH and ZH production at NNLO. This also includes the diagrams of the WHj NLO calculation,

Scale (GeV)		VBFNLO (pb)		MCFM (pb)		Rel. difference	
μ_R	μ_F	LO	NLO	LO	NLO	LO	NLO
10	10	978.0	1573.5	980.0	1569.9	+0.21%	−0.23%
20	20	975.1	1407.0	976.8	1406.5	+0.17%	−0.03%
500	500	792.3	1111.4	793.2	1111.7	+0.11%	+0.03%
1000	1000	749.0	1076.5	749.8	1077.0	+0.10%	+0.04%
1000	10	460.8	794.8	461.2	795.2	+0.09%	+0.04%
10	1000	1589.7	1500.0	1593.3	1499.3	+0.22%	−0.05%

Table 4.3: The cross sections for W^+j production are compared to MCFM using extreme scales. This tests the scale dependent parts of the NLO calculation.

Process	VBFNLO (fb)		vh@nnlo (fb)		Rel. difference	
	LO	NLO	LO	NLO	LO	NLO
WH (with ckm)	1201.38	1520.77	1201.45	1524.01	−0.01%	−0.21%
WH (no ckm)	1209.88	1528.30	1210.17	1531.11	−0.02%	−0.18%

Table 4.4: The inclusive cross section for WH is compared with the NLO implementation of WH production in vh@nnlo. Agreement on the ‰ level is found.

including box diagrams and top-loops, but the program does not give the cross section for WHj (NLO). For diagrams where the Higgs boson is radiated off a W (Drell-Yan type) it uses the code *zwprod* [58]. The integrated cross section of WH (NLO) was checked in the narrow-width approximation against vh@nnlo. As shown in table 4.4, agreement was found at the level of 2 ‰.

4.5.3. Ji-Juan et al.

The first calculation of the differential cross section of WHj (NLO) with W and H being on-shell was done by Ji-Juan et al. in Ref. [49]. For the comparison the narrow-width approximation was implemented. For the NLO calculation they used phase space slicing instead of the method by Catani and Seymour. Their code is not public so that for a comparison their complete setup had to be reproduced. This includes a non-diagonal CKM matrix. $b\bar{b}$ pairs are included, but only if both are in the final state and they are recombined into one jet.

Cross sections are given for a variation around a fixed scale as well as for two choices of dynamic scales,

$$\mu_0 = \frac{1}{2}\left(m_H + m_W\right), \tag{4.10}$$

$$\mu_1 = \sqrt{\frac{1}{2}\left[\left(p_T^W\right)^2 + \left(p_T^H\right)^2 + m_W^2 + m_H^2\right]}, \tag{4.11}$$

$$\mu_2 = \sqrt{\left(p_T^W\right)^2 + \left(p_T^H\right)^2 + m_W^2 + m_H^2}. \tag{4.12}$$

A comparison of the cross sections calculated in this thesis and those presented in Ref. [49] is shown for the LHC and the Tevatron in tables 4.5 and 4.6 respectively. The comparison shows

Process	m_H (GeV)	Scale	VBFNLO (fb)		Ji-Juan et al. (fb)		Rel. difference	
			LO	NLO	LO	NLO	LO	NLO
W^+Hj	120	μ_0	533.08	574.77	531.37	572.90	−0.32 %	−0.33 %
W^+Hj	120	$0.5\mu_0$	589.40	585.90	589.49	588.00	+0.02 %	+0.36 %
W^+Hj	120	$2\mu_0$	483.13	577.93	483.21	561.00	+0.02 %	−2.93 %
W^+Hj	120	μ_1	503.29	581.59	503.36	561.20	+0.01 %	−3.51 %
W^+Hj	120	μ_2	479.86	577.58	479.93	556.40	+0.01 %	−3.67 %
W^+Hj	150	μ_0	284.49	304.71	284.49	294.20	0.00%	−3.45 %
W^+Hj	180	μ_0	166.21	173.51	166.18	167.90	−0.02 %	−3.23 %
W^-Hj	120	μ_0	322.95	359.38	323.03	360.20	+0.03 %	+0.23 %
W^-Hj	120	$0.5\mu_0$	357.60	366.01	357.58	367.20	−0.01 %	+0.33 %
W^-Hj	120	$2\mu_0$	292.71	362.22	292.76	352.10	+0.02 %	−2.79 %
W^-Hj	120	μ_1	305.99	365.03	306.02	350.90	+0.01 %	−3.87 %
W^-Hj	120	μ_2	297.60	362.60	291.63	347.90	+0.01 %	−4.06 %
W^-Hj	150	μ_0	167.41	185.34	164.96	180.94	−1.46 %	−2.38 %
W^-Hj	180	μ_0	95.02	102.67	93.69	100.26	−1.40 %	−2.35 %

Table 4.5: The cross sections for $W^{\pm}Hj$ (NLO) at the LHC is compared with the result in Ref. [49]. For a variation of the Higgs mass, as well as for the NLO calculations, disagreement is found, which is discussed in the text in more detail.

m_H (GeV)	Scale	VBFNLO (fb)		Ji-Juan et al. (fb)		Rel. difference	
		LO	NLO	LO	NLO	LO	NLO
120	μ_0	17.44	21.38	17.44	20.08	−0.01 %	−6.07 %
120	$0.5\mu_0$	21.94	22.50	21.95	21.01	0.04%	−6.62 %
120	$2\mu_0$	14.16	19.73	14.17	18.61	0.04%	−5.67 %
120	μ_1	16.01	20.53	16.01	19.60	0.04%	−4.53 %
120	μ_2	14.45	19.69	14.46	18.79	0.04%	−4.57 %
150	μ_0	8.38	9.93	8.27	9.31	−1.36 %	−6.29 %
180	μ_0	4.40	5.06	4.27	4.63	−2.81 %	−8.51 %

Table 4.6: The cross section for W^-Hj (NLO) at the Tevatron ($\sqrt{s} = 1960\,\text{GeV}$, initial state $p\bar{p}$) is compared with the result in Ref. [49]. Like in table 4.5, there are deviations for a varied Higgs mass at LO and for all parameter choices at NLO.

agreement at LO for all parameter choices except for variations of the Higgs mass, where deviations of several percent are found. However, at NLO there is a discrepancy of up to 4% for the LHC and up to 8.5% for the Tevatron. For W^-Hj with a large Higgs boson mass the disagreement at LO hints towards an inconsistency in interchanging W^+ and W^-. This interchange was extensively studied in comparison to Sherpa and MCFM and no discrepancies were found there.

Because no code is published and the original data of the plots shown in their publication was not available upon request, it was not possible to perform additional comparisons to locate the differences.

4.5.4. WHj (NLO) check coverage

There was no successful direct check of the WHj NLO production cross section with on-shell production. Nevertheless, the calculation was checked indirectly. Wj (NLO) production was thoroughly checked and good agreement with previous calculations was found. WHj and Wj production share most of the calculation, especially the NLO QCD calculation including subtraction terms and box diagrams. Going from Wj to WHj production changes only a small number of parts in the calculation:

Phase space The phase space for WHj is more complex (especially with the Higgs boson decays), but was fully checked in WHj (LO) and WHjj (LO).

EW part For the Drell-Yan type diagrams in WHj (NLO) coming from Wj (NLO) only the EW part changes which is the same substitution (and code) as in the LO case.

Top-loops The only new diagrams in WHj (NLO) are the top-loops, which were checked in sign and amplitude against the amplitudes generated by MadGraph using the heavy top limit. The heavy top limit is approached smoothly.

Therefore, WHj (NLO) was checked in all parts of the calculation and the results can be trusted. Additionally, the scale dependence of WHj was tested by calculating Wj with a virtual W, that resembled the W^* in $W^* \to WH$. This is discussed in more detail in section 5.3.

CHAPTER 5

PHENOMENOLOGY

In this chapter the phenomenology of Higgsstrahlung with an additional jet is discussed. This discussion focusses on the production of W^+Hj, but the effects are similar for W^-Hj production and to some extent also affect WH production.

In section 5.1 the setup for the analyses is introduced. The general effect of NLO corrections on the cross section and the contribution of top-loops in particular is discussed in section 5.2. Section 5.3 describes the scale dependence of the results. WHj production is compared to Wj production and different scale choices are assessed. In section 5.5 the effect of anomalous couplings is shown. For experimental analyses a special region of phase space, requiring a high-p_T (boosted) Higgs boson, is interesting as it allows the suppression of backgrounds. This phase space region is discussed in section 5.6.

5.1. Event selection/Cuts

To simulate experimental analyses performed at the LHC, as center-of-mass energy $\sqrt{s} = 14\,\text{TeV}$ is used. The EW input parameters are given in appendix A. If not stated otherwise, the cuts and parameters used are

$$\begin{aligned} &R_{jj} = 0.8, k_T\text{-alg.}, \quad R_{jl} = 0.6\,, \quad && m_h = 126\,\text{GeV}\,, \\ &p_{T,j} = 30\,\text{GeV}\,, \quad && p_{T,l} = 20\,\text{GeV}\,, \quad \mu_R = \mu_F = m_Z\,, \\ &|\eta_j| < 4.5\,, && |\eta_l| < 2.5\,. \end{aligned} \tag{5.1}$$

5.2. NLO effects

The cross sections given in this section include the leptonic decay of the W to the first lepton family ($W^+ \to e^+\nu$). They do not include the Higgs boson decay. In a typical experimental VH analysis, in addition the $BR(H \to b\bar{b}) = 57\%$ as well as the decay $W^+ \to \mu^+\nu_\mu$ are used. The latter can be included when considering the same cuts and input parameters by multiplying the total cross section and differential distributions with a factor 2. Other Higgs decays can be included. Their effect on the cross section depends on both the branching ratio and the cuts used for the decay products. The branching ratios are taken from VBFNLO 2.7.0 beta 4. Since the dominating region is on-shell WH production, the process discussed here will be called WH production despite including the leptonic decay.

Process	LO (fb)	NLO (fb)	K-Factor
W^+H	55.724(2)	76.303(7)	1.37
W^-H	31.720(2)	44.732(7)	1.41
W^+Hj	25.316(4)	28.761(14)	1.13
W^-Hj	14.506(3)	16.668(7)	1.15
W^+Hjj	10.715(2)		
W^-Hjj	6.112(2)		

Table 5.1: An overview of LO and NLO cross sections for the production of $W^{\pm}H$ including the decay $W \to e\nu_e$ and up to two jets is given as well as the NLO K-factors. The uncertainty given is the Monte Carlo error estimate. The NLO corrections have a sizeable effect and requiring additional jets within the cuts given in equation (5.1) leads to a reduced, yet sizeable cross section.

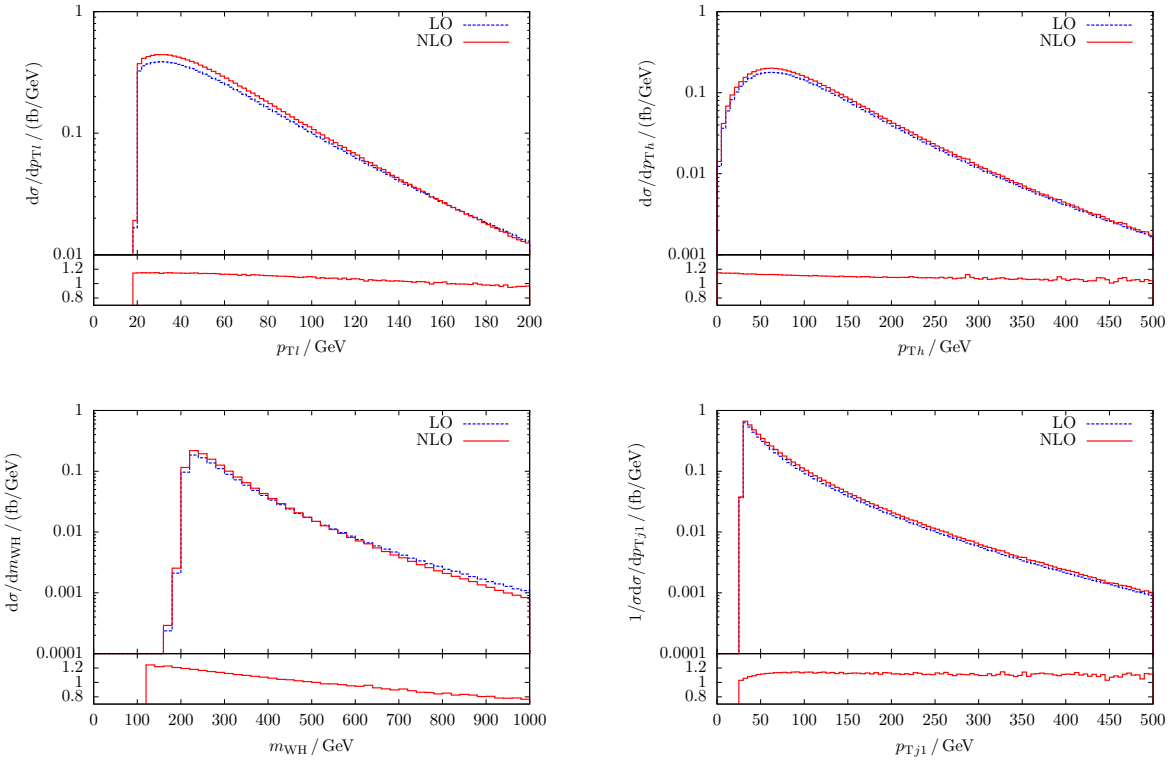

Figure 5.1: The LO and NLO differential cross sections for several variables are compared. The K-factor for $p_{\mathrm{T}h}$ and $p_{\mathrm{T}l}$ is generally larger for small p_{T} and reduces for large p_{T}. The dependence on m_{WH} shows a K-factor in the range between 0.8 and 1.2.

In table 5.1 the cross section at LO and NLO of $W^{\pm}H$ production with up to two jets (the latter only LO) is given. This shows (even before discussing distributions) the importance of NLO effects and also that requiring additional hard jets reduces the cross section. Nonetheless, the production of WH even with one or two jets is well within the reach of the final luminosity stage of the LHC. The NLO corrections change not only the total cross section, but also the shape of distributions. Therefore, it is important to use NLO calculation, as multiplying the LO results with a constant K-factor does not reproduce differential distributions correctly.

cuts used	NLO cross section (fb) with top-loop	without top-loop	rel. difference
standard cuts, $p_{\mathrm{T}j} > 30\,\mathrm{GeV}$	28.74	28.11	+2.2%
$p_{\mathrm{T}j} > 100\,\mathrm{GeV}$	6.38	6.20	+2.8%

Table 5.2: The contribution of top-loop diagrams to the cross section is shown. They add 2-3% and show a small dependence on the phase space region.

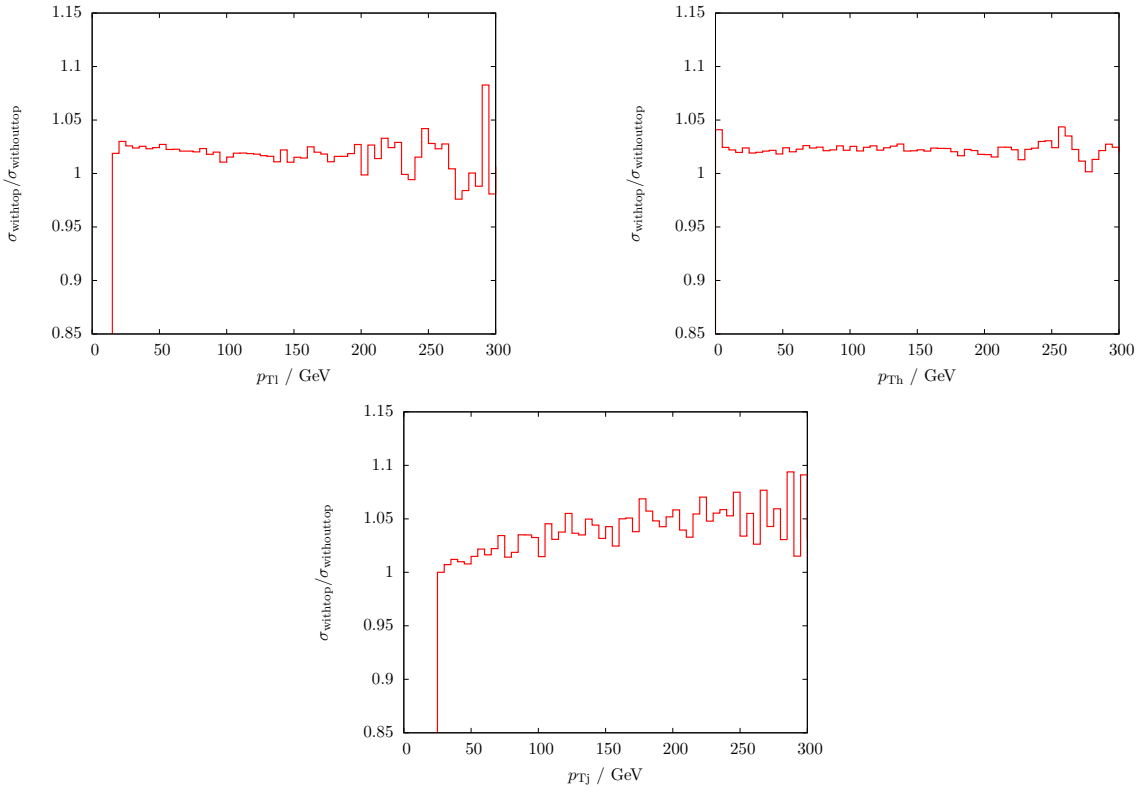

Figure 5.2: The ratio comparing the calculation including top-loops to the one without top-loops is shown. As an example, the dependence on the p_{T} of the lepton, the Higgs boson and the leading jet is given. There is a modest dependence on the jet p_{T}, while the other distributions are essentially flat.

Examples of affected distributions are shown in figure 5.1.

5.2.1. Top-loops

Including the top-loops in the calculation of the virtual amplitude affects both the cross sections and the distributions. The total cross section is changed as shown in table 5.2. The contribution to the cross section is on the level of 2-3%. This is in agreement with the results presented for WH (NNLO) in Ref. [57].

There are no regions in phase space with especially large effects of the top-loops. The differential distributions have an approximately flat behaviour, as shown in figure 5.2. There is a small dependence on the jet cuts. This can be seen in both table 5.2 and the $p_{\mathrm{T}j}$ distribution in figure 5.2. This dependence is less than the total top-loop contribution.

5.3. Scale dependence

In any hadron collider NLO calculation there are two typical unphysical scales involved that are a remnant of the incomplete perturbation theory series: The factorization scale μ_F, which relates to the PDFs, and the renormalization scale μ_R.

Those scales only show up, because the calculation involves a finite number of terms in perturbation theory and their dependence would vanish if all orders were included. Therefore, they provide access to the possible effects of higher orders and thus the theoretical error. While any variation must vanish when higher orders are included, there is no certainty that higher orders can not be larger than the variation. There are quite a few processes where this is the case, e.g. WW or WZ production. In those examples, at leading order, there is only the $q\bar{q}$ initial state, but new partonic subprocesses appear as part of the real corrections, including qq or gluon initial states, which access enhanced PDFs and, therefore, partially compensate the α_s suppression.

A typical choice for estimating the theoretical error is varying both scales separately by a factor 2 (or 3) around a chosen center value. The other common choice is to vary both individually in a certain range and to look for a maximum and minimum in the μ_R, μ_F-plane.

5.3.1. Scale choices

The scale to be used for μ_R and μ_F is mostly arbitrary, as long as it is a representative scale associated with the process. Nevertheless, there are choices preferred to others and discussing scale variation plots will shed light on what a typical process scale could be.

For a fixed scale the obvious choice are the masses of the involved particles. For WHj production those are m_H and m_W. One could use one of those masses or their (arithmetic or geometric) mean. A constant factor $(1/2, 1/\sqrt{2}, 2)$ could also be justified. This incomplete list gives a total of 12 possible scale choices, demonstrating the arbitrariness of the scale choice.

The scale choice has only a small effect on the calculation, as is shown in the next sections, so that this is not a critical issue. However, static scale choices are recently used less, since they are not able to describe the dynamics of the system correctly. This is often reflected in a poor behaviour of the LO differential distributions for those choices.

5.3.1.1. Dynamical Scales

Instead of a fixed scale a dynamical scale can be used, which depends on the phase space point considered. While this approach might be counterintuitive to the way the scales were introduced, it leads to more stable results.

A good example for a well-working dynamical scale is vector boson fusion (VBF), which is shown in figure 2.5b. In this process, there are two quark lines which at NLO can be treated independently in QCD. Using the momentum transfer Q^2, which the parton transfers to the EW part, as a scale leads to a small scale variation uncertainty and a LO cross section close to the NLO result.

For WHj production there is no obvious best choice for a dynamical scale. A typical scale is the q^2 of the EW part, which corresponds to the invariant mass of the WH system. This scale is also used by the LHC Higgs Cross Section Working Group e.g. in Ref. [29]. Another possible scale choice is the transverse Energy $E_t = \sqrt{{p_T}^2 + m^2}$ of final state particles. There

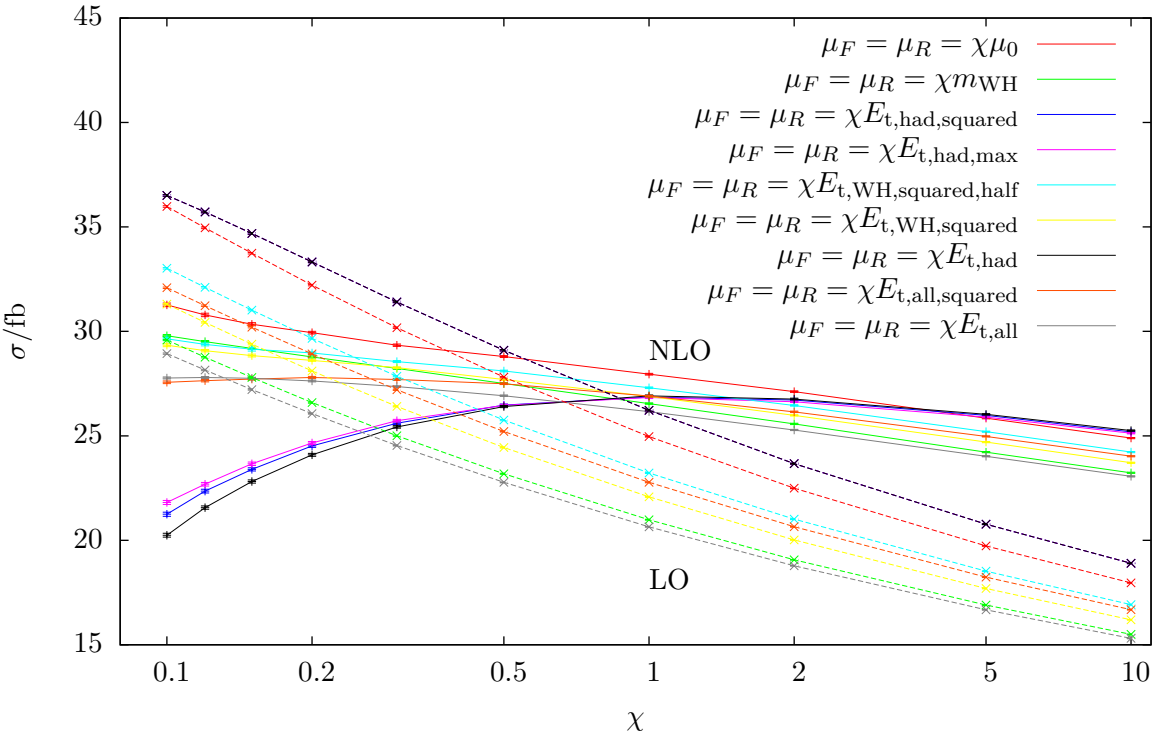

Figure 5.3: The scale variation for W^+Hj and different scale choices is shown, with the LO (NLO) cross section as a dashed (solid) line. A constant scale of m_Z and the dynamical scale of m_{WH} are compared to several other choices defined in equation (5.2). An analysis of the shapes is given in the text.

is an ambiguity which particles to include. Several scales are defined based in transverse momenta or transverse energy of final state particles,

$$\begin{aligned}
E^2_{\mathrm{t,WH,squared}} &\equiv \sum_{i=\mathrm{W,H}} p_{\mathrm{T}i}^2 + m_i^2, & E^2_{\mathrm{t,had,squared}} &\equiv \sum_{\mathrm{partons}} {p_{\mathrm{T}}}^2, \\
E^2_{\mathrm{t,WH,squared,half}} &\equiv \frac{1}{2} \sum_{i=\mathrm{W,H}} p_{\mathrm{T}i}^2 + m_i^2, & E_{\mathrm{t,had,max}} &\equiv \max_{\mathrm{partons}} {p_{\mathrm{T}}}^2, \\
E^2_{\mathrm{t,all,squared}} &\equiv \sum_{\mathrm{partons}} {p_{\mathrm{T}}}^2 + \sum_{i=\mathrm{W,H}} p_{\mathrm{T}i}^2, & E_{\mathrm{t,had}} &\equiv \sum_{\mathrm{partons}} p_{\mathrm{T}}, \\
E_{\mathrm{t,all}} &\equiv \sum_{\mathrm{partons}} p_{\mathrm{T}} + \sum_{i=\mathrm{W,H}} p_{\mathrm{T}i}.
\end{aligned} \tag{5.2}$$

E_t can include either only the EW particles, only hadronic particles or both. While the total E_t is the sum of energies squared, one could also argue that the relevant scale should be the (linear) sum of the energies, or the maximum.

This leads to many possible choices for a dynamical scale. While some of the choices might be backed by better reasons than other, they all are plausible. This spectrum of scales leads to an overall consistent picture of the process. In figure 5.3 the scale variation for W^+Hj with the different possible scales discussed here is shown. The LO and NLO are drawn as dashed and solid lines respectively.

LO

For the LO cross section there is a common behaviour under variation for all scales choices. This can be seen in figure 5.3, where the scales are varied simultaneously, $\mu_F = \mu_R = \chi\mu_0$. The scale variation is dominated by the running of α_s, which depends on μ_R. While the shape is very similar, the different scales have different magnitudes, which leads to a sizeable separation. The smallest scales only include the E_t of the hadronic particles, which (at LO) is only one parton. Adding more particles to the E_t sum increases the value of the scale. It is maximal when the E_t of all particles is combined. Also m_{WH} is one of the largest scales as it also includes non-transverse components. Larger scales lead to smaller cross sections, due to the decrease of the value of α_s.

NLO

At NLO the situation is different as the dependence on μ_R is more complex resulting in two distinct shapes.

The scales that only include the final state partons, shown in the plot as black, blue and pink, have a maximum and decrease for small χ. These hadronic energies are significantly smaller than the other scales which all include either m_W, m_H or an EW particle with a large p_T cut. Therefore, a variation with $\chi = 0.1$ corresponds to a scale of a few GeV. This is too small to trust the perturbation theory of this process.

All other scales have a approximately linear shape and increase for small χ. The slope is smaller than in the LO case. Despite the different shapes at NLO, when considering $\chi = 1$, all scales are within the range of 26 to 28 fb while at LO the range is 20 to 26 fb. Going from LO to NLO, therefore, improves the scale dependence twofold: The choice of scale has a smaller effect on the cross section and varying a chosen scale also has a smaller influence.

5.3.2. Scale variation as error estimate

As discussed before, scale variation gives an estimate of the possible effects of higher orders and, therefore, the uncertainty of the perturbation theory calculation. While scale variation can be thought of as a lower bound on higher orders, it can underestimate the theoretical error as shown for example in the following.

5.3.2.1. WHj

In section 5.3.1.1 dynamical scales were introduced and for figure 5.4 the example of m_{WH} is chosen to illustrate their behaviour.

In figure 5.5 the scale variation for a fixed scale for the process W^+Hj is shown. The central value for the scale is $\mu_0 = m_Z$. The precise choice is arbitrary and m_W, m_H or 100 GeV would also be reasonable. In both cases the scale variation is dominated by the dependence on μ_R.

Following the convention to estimate the theoretical error by varying $\mu_F = \mu_R = \chi\mu_0$, $\chi \in [0.5, 2]$ leads to the uncertainty estimates given in table 5.3. Using the NLO calculation reduces the scale dependence by a factor 3 from 19% to 7%. The remaining uncertainty is on a similar order as other theoretical errors (PDFs, α_s, n_f, ...).

5.3.2.2. Wj

The behaviour of Wj is different than the one of WHj production. Figure 5.6 shows that when both scales are varied simultaneously ($\mu_R = \mu_F = \chi\mu_0$), then at LO, there are cancellations,

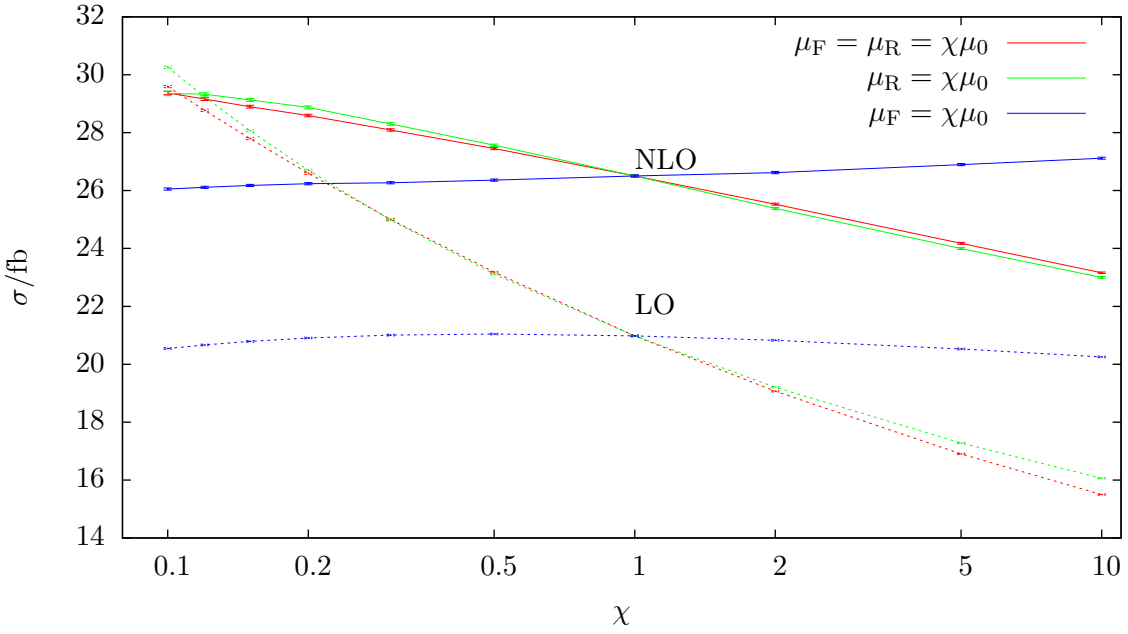

Figure 5.4: The scale variation for W^+Hj with the dynamical scale $\mu_0 = m_{WH}$ is shown. The qualitative behaviour is comparable to the variation of a fixed scale shown in figure 5.5, as is the resulting scale uncertainty in the interval $\chi \in [0.5, 2]$.

	uncertainty	
scale	LO	NLO
fixed ($\mu_0 = m_Z$)	21%	6%
dynamical ($\mu_0 = m_{WH}$)	19%	7%

Table 5.3: The scale uncertainty comparing LO, NLO with a fixed and dynamical scale for WHj is given. Both scale choices show a similar scale dependence.

so that the variation seems to be smaller then the one obtained when both scales are varied separately. Considering just the variation of μ_R leads to a larger (more realistic) uncertainty.

The scale variation for Wj looks quite different in shape compared to WHj. The difference is most obvious in the behaviour for small χ. In WHj the LO diverges, showing the typical α_s dependence. In Wj the LO with both scales varied simultaneously shows a cancellation and is close to flat. The NLO in WHj flattens out for small χ, while it diverges in Wj. As they share a lot of structure, this is rather unexpected.

The major difference is that in WHj the W coupling to the quark line is far off-shell and has a typical invariant mass of above 200 GeV. This is required to allow the final state Higgs boson and W to be close to on-shell.

Calculating Wj and forcing an invariant mass of the W above 200 GeV leads to the scale variation shown in figure 5.7. The shape here resembles the one of WHj more closely. This

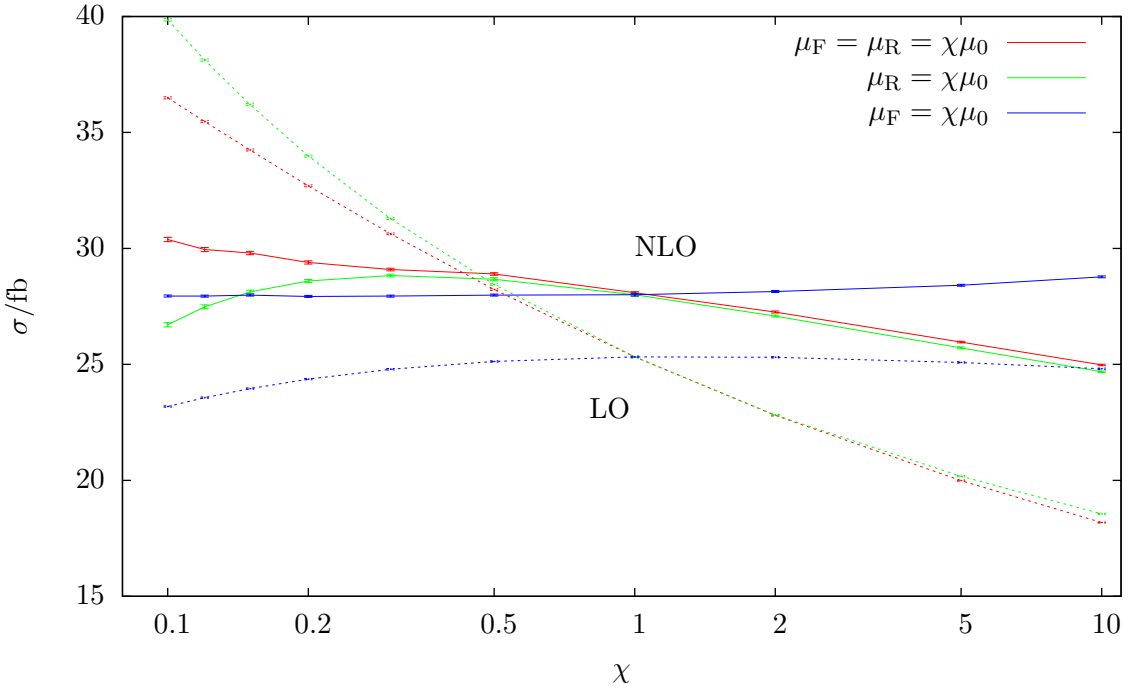

Figure 5.5: The scale variation for W^+Hj with the fixed scale $\mu_0 = m_Z$ is shown. In the interval $\chi \in [0.5, 2]$ the μ_R dependence dominates. The scale dependence of the NLO calculation is reduced by a factor 3 compared to the LO.

	uncertainty	
variation	LO	NLO
$\mu_R = \mu_F = \chi\mu_0$	9%	9%
$\mu_R = \chi\mu_0$, $\mu_F = \mu_0$	23%	14%

Table 5.4: The scale uncertainty for Wj both at LO and NLO is given. The dependence on varying μ_R and μ_F simultaneously is compared to varying only μ_R around the central scale $\mu_0 = m_Z$. For Wj there is a cancellation between the μ_R and μ_F dependence, such that varying both scales simultaneously underestimates the overall scale dependence.

confirms that the behaviour of WHj (or WH) can be mimicked by Wj (or W) in the high-mass tail. This comparison is also an additional check for the scale dependence of the WHj implementation.

This region of Wj phase space also explicitly shows one of the contributions to the order of magnitude difference between WHj and Wj. Forcing the W so far off shell reduces the cross section from $1.2 \cdot 10^3$ pb to 1.6 pb. This factor of roughly 10^3 is related to the off-shell propagator. While in the on-shell case the typical factor is $1/m\Gamma$, in the off-shell case the factor is $1/p^2$. The remaining difference to the WHj case is related to the additional WWH coupling.

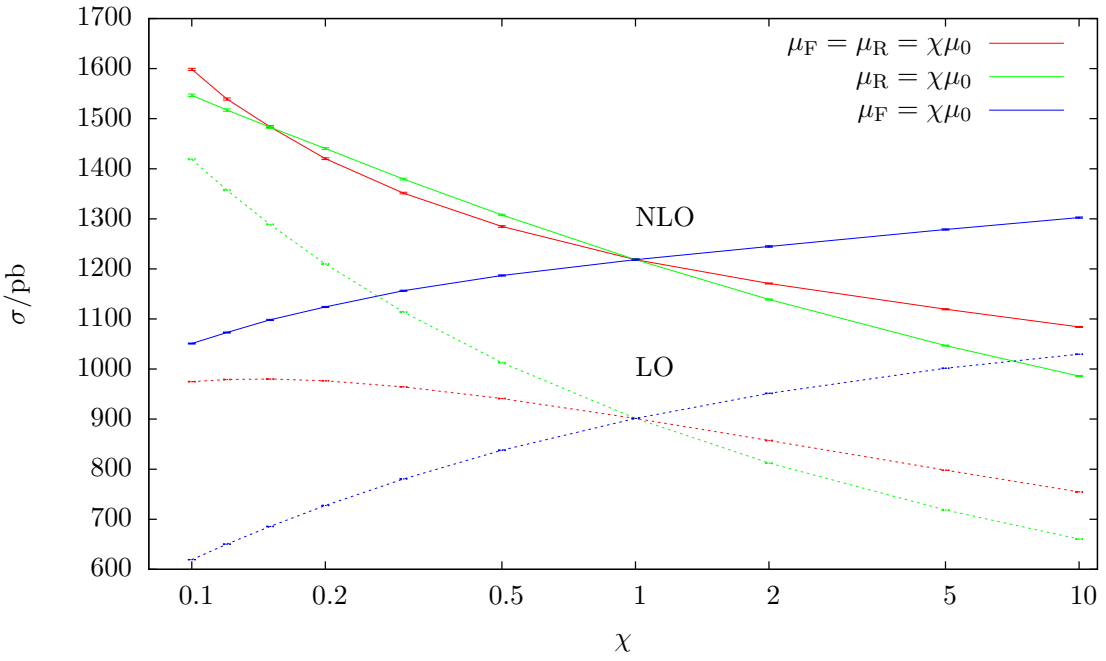

Figure 5.6: The scale variation for W^+j with the fixed scale $\mu_0 = m_Z$ is shown. The cross section is several orders of magnitude larger than for WHj and, therefore, given in pb. The simultaneous variation of μ_R and μ_F shown cancellations between the opposing scale dependences on μ_R and μ_F, such that the overall scale dependence is underestimated when fixing $\mu_R = \mu_F$.

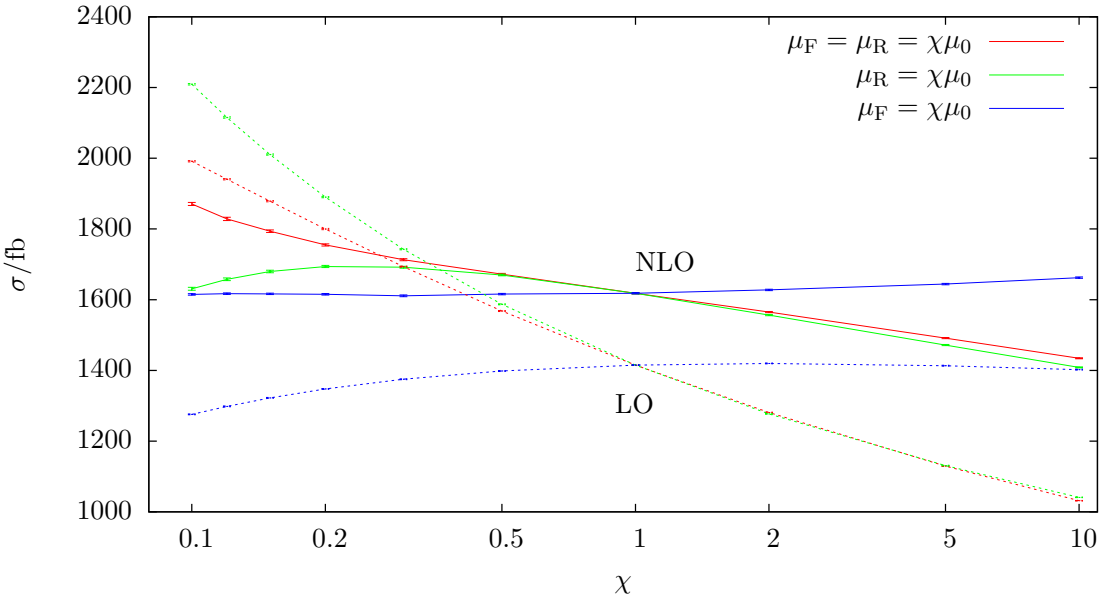

Figure 5.7: The scale variation for W^+j with the fixed scale $\mu_0 = m_Z$ is shown. The invariant mass of the W is required to be above 200 GeV. This cut resembles the production of WHj, where the W attached to the quark line has a typical invariant mass of above 200 GeV.

	uncertainty		
scale	LO	NLO	NLO (jet veto)
$\mu_0 = m_Z$	21%	6%	1.9%
$\mu_0 = m_{WH}$	20%	7%	3.4%

Table 5.5: A jet veto apparently reduces the scale uncertainty, as discussed in the test. The scale uncertainty is shown, varying $\mu_R = \mu_F = \chi\mu_0, \chi \in [0.5, 2]$ for a fixed and dynamical scale. Depending on the scale choice the scale dependence is reduced by a factor 2-3.

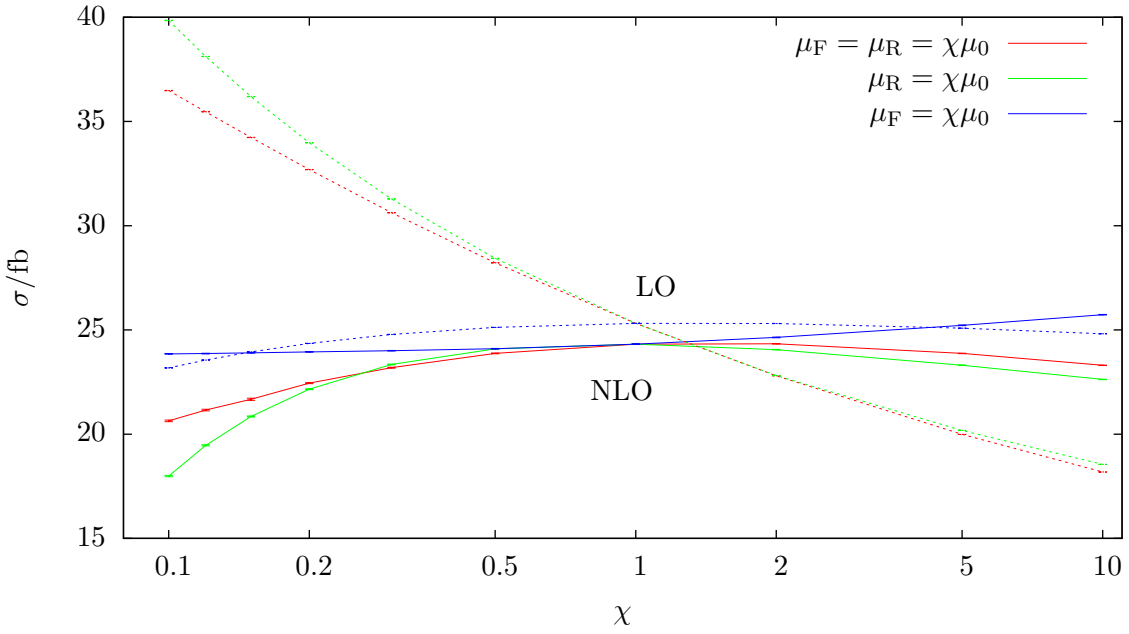

Figure 5.8: Applying a jet veto of $p_{T\,veto} = 50\,\text{GeV}$ changes the shape of the scale dependence. The variation is reduced, but does no longer provide a reliable estimate of the theoretical uncertainties, as shown in the text.

5.4. Jet veto

At NLO the real emission in WHj production leads to two partons in the final state. They can be clustered into one jet if they are close together, yet they may also be identified as two jets. The amount of two jet events can be reduced by introducing a *jet veto*. This means introducing a cut that removes all two jet events where the second jet has a p_T larger than $p_{T\,veto}$. For this discussion a jet veto of $p_{T\,veto} = 50\,\text{GeV}$ is used.

With a jet veto, the scale dependence seems to be reduced. As shown in table 5.5 the uncertainty by varying the scale between 0.5 and 2 times a central scale is reduced by a factor 3 in case of the fixed scale and a factor 2 for the dynamical scale. Considering the scale variation over a larger range in figure 5.8 also shows a flat behaviour of the NLO cross section. This reduced scale uncertainty is an accidental feature of the jet veto. The jet veto removes most of the real emission and while the total cross section appears less scale dependent, there

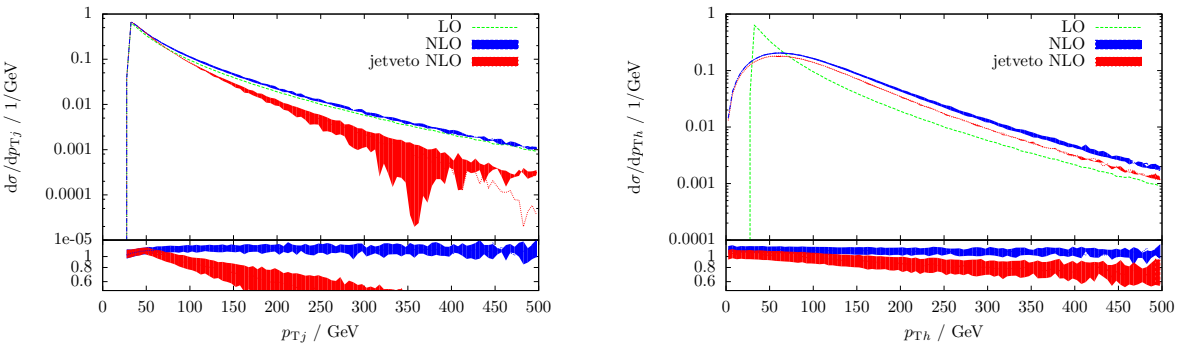

Figure 5.9: The p_{T} distribution of the hardest jet and the Higgs boson are shown, both with and without a jet veto of $p_{\mathrm{T\,veto}} = 50\,\mathrm{GeV}$ on the second jet at NLO. The scale variation is given as coloured bands around the dashed central value. For large p_{T} the jet veto leads to a reduced cross section. The dependence on the p_{T} of the hardest jet (left) shows a large scale dependence for high p_{T}, which grows and is far above the scale uncertainty of the total cross section. At approximately 350 GeV the scale variation spreads several orders of magnitude covering also negative values for the cross section. The absolute value is plotted in that region. On the other hand, the Higgs p_{T} (right) is rather well behaved. As can be seen for the K-factor, the scale dependence is slightly worse, but comparable to the situation without jet veto.

can be large scale dependences on other observables. Therefore, the calculated scale uncertainty can not be used as a theory uncertainty. This behaviour is known and was extensively studied in Higgs boson production in Gluon Fusion, Ref. [59]. The method proposed there should also be used here. Its effect on the calculation of WHj production is, that the scale variation of the inclusive calculation gives a more realistic estimate, but underestimates enhanced uncertainties in some distributions. In Multiboson plus jet production a similar behaviour can be observed, as presented in Ref. [38]. Figure 5.9 shows the p_{T} of the Higgs boson and of the hardest jet for NLO calculations with and without a jet veto. The jet p_{T} shows a large and diverging scale dependence in the high-p_{T} region, while the Higgs boson p_{T} is less affected. This again demonstrates that the errors of exclusive samples must be considered carefully.

f_W (TeV^{-2})	cross section (fb)			$p_{\mathrm{T}h} < 200\,\mathrm{GeV}$		
	LO	NLO	K	LO	NLO	K
0	24.96	28.59	1.14	21.54	24.83	1.15
1	22.93	25.91	1.13	20.45	23.10	1.13
−1	28.05	30.71	1.09	22.70	25.55	1.13
10	52.34	34.61	0.66	13.57	15.47	1.14
−10	103.51	82.68	0.80	36.04	39.96	1.11

Table 5.6: The cross section of $\mathrm{W}^+\mathrm{Hj}$ production with the cuts from equation (5.1) is shown for different couplings of the $\mathcal{O}_W$ operator. Anomalous couplings affect the total cross section as well as the K factor. The normal K-factor can be restored when excluding the high-p_{T} region, but introducing a cut $p_{\mathrm{T}h} < 200\,\mathrm{GeV}$. This is discussed in the text in more detail.

5.5. Anomalous couplings

Anomalous couplings are a general approach to describe physics beyond the Standard Model based on an effective field theory. For WH(j) production only anomalous couplings modifying the WWH vertex are considered. The decay of the Higgs boson is factored, so that both production and decay include anomalous couplings, but an intermediate Higgs boson is required. As discussed in section 2.2, only the operators $\mathcal{O}_W, \mathcal{O}_{WW}, \mathcal{O}_{\widetilde{W}}$ and $\mathcal{O}_{\widetilde{W}W}$ affect this process.

The effect of anomalous couplings is more prominent in the high p_{T} region. To give an example of the typical shape the operator $\mathcal{O}_W$ is chosen and the corresponding coupling f_W varied.

Anomalous couplings have a significant effect on the total cross section, which is shown in table 5.6. Also the K-factor is significantly changed, from 1.14 to 0.8 and 0.66. Responsible for the K-factor is the high-p_{T} region of phase space. Introducing a cut $p_{\mathrm{T}h} < 200\,\mathrm{GeV}$ restores the normal K-factor, but not the normalization of the cross section.

Not only the total cross section is changed, also the shape of distributions change when including anomalous couplings. In figure 5.10 differential cross sections for observables are shown, whose shape is affected by anomalous couplings. For the coupling f_W the values $\pm 1\,\mathrm{TeV}^{-2}$ and $\pm 10\,\mathrm{TeV}^{-2}$ are plotted and compared against the Standard Model without anomalous couplings shown with the scale variation error band.

For $f_W = \pm 1\,\mathrm{TeV}^{-2}$, the deviation from the Standard Model cross section is comparable to the scale variation in η_{h} and p_{Tl}, while for $p_{\mathrm{Th}} \gtrsim 300\,\mathrm{GeV}$ there is a significant difference. Increasing f_W to $\pm 10\,\mathrm{TeV}^{-2}$ gives cross section shapes that are far from the Standard Model and show enhancements in the high-p_{T} and the central region for both Higgs boson and lepton. The behaviour in the large p_{T} region could be suppressed using a form factor.

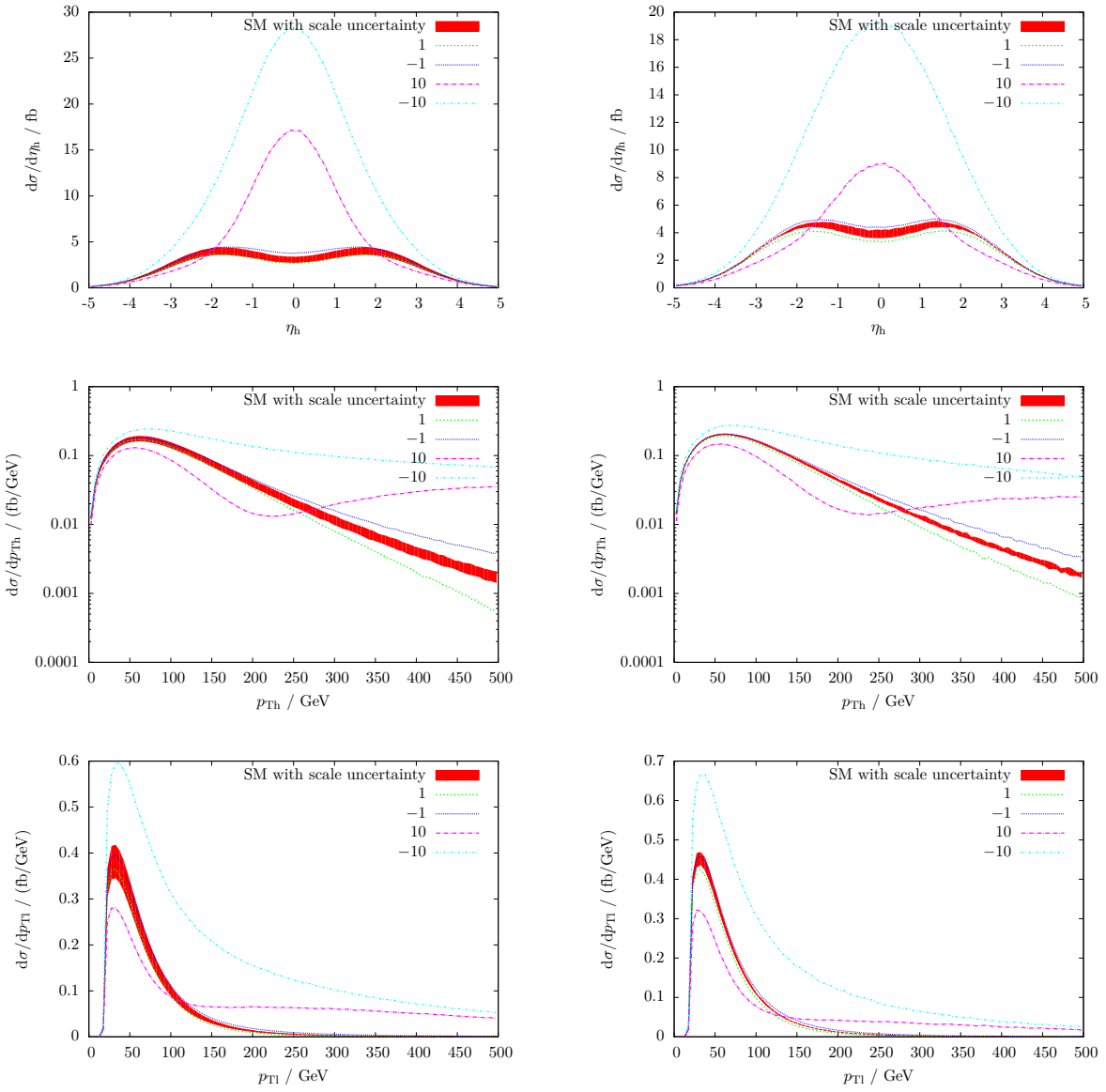

(a) LO **(b)** NLO

Figure 5.10: Anomalous couplings change the shape of differential cross sections. Here, as an example, the effect of the $\mathcal{O}_W$ operator for different couplings in TeV^{-2} on the Higgs p_T, the lepton p_T and the pseudo rapidity of the Higgs boson in WHj production is shown. These effects can be much larger than the SM scale uncertainty, which is shown as a band.

Process	LO (fb)	NLO (fb)	K
normal cuts	25.31	28.11	1.11
$p_{\mathrm{Th}} > 200\,\mathrm{GeV}$	3.49	3.74	1.07

Table 5.7: The cross sections and K-factors for inclusive cuts and a boosted Higgs analysis are compared. The cross section is reduced by an order of magnitude, but the K-factor on the total cross section is unchanged.

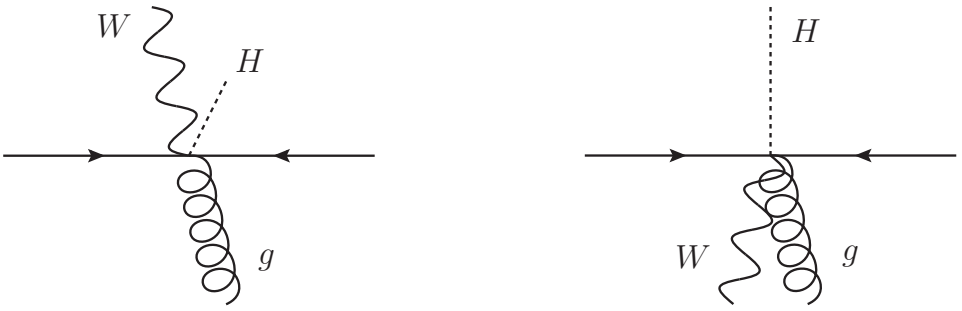

Figure 5.11: This schematic representation illustrates the typical kinematical configuration in the case of normal detector cuts (left) compared to the boosted Higgs configuration (right). The large p_{T} of the Higgs boson in the boosted case is balanced against the other final state particles.

5.6. Boosted Higgs boson

For an experimental search of WH production with $\mathrm{H} \to \mathrm{bb}$ at a hadron collider, the main background is the production of W+jets and $\mathrm{t\bar{t}}$. Because of the large background, WH with inclusive cuts is problematic as a Higgs boson discovery channel or for the study of its properties. The analysis can be crucially improved in a phase space region suggested by Butterworth, Salam et al. in Ref. [31]. They proposed *boosted Higgs* searches, which means a p_{T} cut of about 200 GeV for the Higgs boson candidate. This cuts about 90% of the WH cross section, however, it cuts even more of the W+jets background. This improves the ratio of signal over background to an experimentally interesting value. Nevertheless, currently most major analysis consider less stringent cuts due to the small number of events.

In the case of WH without additional jets, requiring the Higgs boson to have high p_{T} is equal to requiring the W to have high p_{T}, as they can only balance each other. This equivalence vanishes when considering additional jets.

Table 5.7 shows the cross sections and K-factors comparing the boosted Higgs phase space region to the normal cuts used in this section. The cross section is reduced by close to an order of magnitude, but the K-factor on the level of the total cross section stays about the same. Nevertheless, the differential K-factors will be significantly affected by this new cut.

The typical kinematic configurations of normal WHj production compared to the boosted case are shown in figure 5.11. With normal cuts, the p_{T} distributions of the Higgs boson as well as W and jet peak below 100 GeV, so that they favor small p_{T}. W and Higgs boson as well as the jet all balance each other about equally. Requiring high p_{T} for the Higgs boson forces the other final state particles to balance this p_{T}. The W boson and the jet favour small p_{T} and, hence, in the boosted Higgs case both balance p_{TH} equally. This leads to events with the jet closer to the W boson than for normal cuts and both recoiling against the Higgs boson.

The momenta dependence of the cross section is more complex than this depiction of the momenta configuration, but it can be used as illustration and is supported by the differential distributions discussed in the following.

Figure 5.12 shows observables with and without the cut of $p_{\mathrm{TH}} > 200\,\mathrm{GeV}$. The p_{TH} distribution illustrates the large fraction of the cross section, which is affected by this cut. The peak of $\mathrm{d}\sigma/\mathrm{d}p_{\mathrm{TH}}$ is at about 60 GeV and therefore well below the cut. The $p_{\mathrm{T}j1}$ tends to larger transverse momenta with the boosted Higgs cut, so that the small-$p_{\mathrm{T}j1}$ region is reduced corresponding to the cross section, but for $p_{\mathrm{T}j1} \approx 500\,\mathrm{GeV}$ nearly the uncut cross section is restored. The ratio of 1-jet to 2-jet events is shifted from about 2 : 1 with normal cuts, to 1 : 1 in the boosted case. Additionally, the jets are closer together, as is shown by the difference in the azimuthal angle of the jets in two-jet events, $\phi_{j,j}$.

An important distribution for the tagging of WH events is $p_{\mathrm{T}l}$. Meanwhile for normal cuts the K-factor is rather flat, the cut on the Higgs boson p_{T} leads to a large variation of the K-factor. For small transverse momenta of the lepton (and thus to some extent the W boson), the cross section is enhanced at NLO. This might be related to two-jet events, where both jets recoil against the Higgs boson and allow for a softer W boson.

The general picture of the W boson and jets recoiling together against the Higgs boson is also supported by the difference in the azimuthal angle between the hardest jet and the lepton. While these are mostly in opposite directions with normal cuts, the boosted Higgs cut requires them to be closer together.

The invariant mass of the WH system in normal cuts shows a peak slightly above $m_{\mathrm{W}} + m_{\mathrm{H}} \approx 200\,\mathrm{GeV}$ and a non-constant K-factor. Introducing the boosted Higgs cut, the peak is moved to around 500 GeV. An invariant mass of 500 GeV approximately corresponds to W and Higgs boson in opposing directions with both p_{T} close to the boosted Higgs cut.

These distributions show that an analysis using a cut on the p_{T} of the Higgs boson increases the importance of additional jets and has a strong effect on differential K-factors in observables important in Higgs boson searches. They demonstrate that NLO calculations are essential for a precise description of this phase space region.

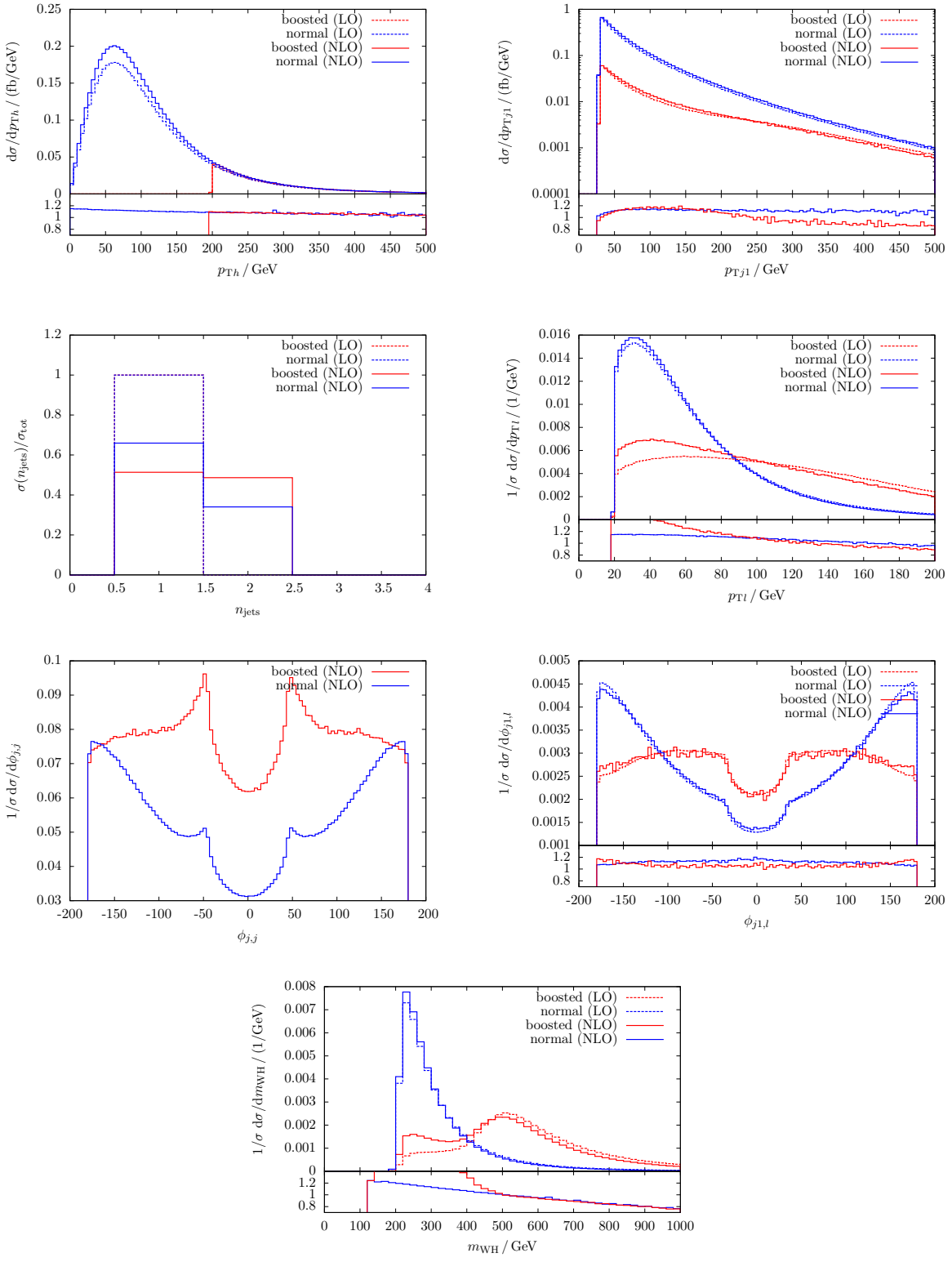

Figure 5.12: Considering a boosted Higgs analysis with $p_{\mathrm{TH}} > 200\,\mathrm{GeV}$, differential distributions for several observables are shown, comparing the boosted analysis to inclusive cuts. The various kinematical effects are discussed in the text.

CHAPTER 6

SUMMARY AND OUTLOOK

In this thesis, the production of WHj was calculated at NLO QCD. It is implemented in the Monte Carlo program VBFNLO together with the processes W, Wj and WH production, which have a similar structure. The subtraction formalism by Catani and Seymour [21] is used to combine virtual corrections and real emission in the NLO calculation. The calculation includes leptonic decays of the W. For the Higgs boson the decays to $b\bar{b}$, $\gamma\gamma$, $\tau\overline{\tau}$, $\mu\overline{\mu}$, $WW \to l\nu\, l\nu$, $ZZ \to ll\, ll$ and $ZZ \to ll\, \nu\nu$ are implemented. They can be factorized and are included using higher order branching ratios for the 2 particle decays and LO matrix elements for the $H \to VV \to 4l$ decay channels.

The virtual contributions of the NLO calculation consist of self-energy and vertex corrections as well as box diagrams. These are calculated using existing routines from Ref. [44]. For WHj (NLO) production there are also diagrams where the Higgs couples to a top-loop, which are calculated with full top quark mass dependence using the routines for massive quark triangles in Ref. [45]. The real emission for WHj production has two types of diagrams. The first involve diagrams with one quark line and two gluons attached to it, which give access to the large gluon PDFs. The other diagram class has two quark lines.

The non-diagonal CKM matrix is taken into account. A general mechanism is presented, which describes how to include the CKM matrix by modifying the PDFs and leaving the matrix elements flavour independent. This allows to include the CKM matrix in calculations, that are implemented without flavour information in the matrix element. The implementation is successfully compared against MCFM and Sherpa for WH at NLO and WHj as well as WHjj at LO. Checks and numerical discussions are based on considering only the mixing of the first two generations. These effects are shown to be less than 1% in all studied processes at the level of the total cross section. Effects of about 2% are seen in extreme phase space regions that have a negligible cross section.

The top-loop diagrams appear in the NLO QCD calculation of WHj production, however they are not present in Wj production. A comparison of the full mass dependent calculation to the implementation in MadGraph using the heavy top limit shows that the heavy-top approximation is not able to describe WHj production well. Nevertheless in several scenarios agreement with MadGraph was found and the contribution of the top-loop diagrams to the total cross section is on the level of 2-3%. There is no strong phase space dependence of these

contributions.

The calculation is implemented in both four and five flavour scheme. The possible choice of flavour scheme is discussed. The focus of this discussion is on the relations of different parts of the calculation and how they require a consistent flavour scheme throughout. It is shown that the choice of flavour scheme leads to changes within the scale uncertainty of a few percent, but inconsistent choices can increase those.

Several cross checks were performed to confirm the correctness of the implementation. The LO matrix element was compared with MadGraph. The LO cross section was checked with Sherpa. For the virtual amplitude internal checks based on Ward identities and known analytical results were performed. The NLO cross section of WH and Wj production was compared with MCFM and agreement for all checks was found within the statistical error at the ‰ level. All parts of the NLO calculation of WHj were successfully checked. In comparison with a previous calculation of WHj production with on-shell W and Higgs boson [49] differences on the level of several percent were found. For this comparison the narrow-width approximation was implemented and used. For several parameter choices there are deviations already at LO and the differences show a scale dependence. The calculation of WHj production differs from Wj production in only a few aspects and was fully checked, such that the result can be trusted. Recently another NLO QCD calculation of VHj production was published in Ref. [60], but the results could not yet be compared.

The cross section of W^+Hj is 25.3 fb at LO and 28.8 fb at NLO. In the case of W^-Hj production the cross section is reduced due to the different combination of PDFs. It is 14.5 fb at LO and 16.7 fb at NLO. This gives a K-factor of 1.13 and 1.15 respectively.

The theoretical error is usually estimated based on the variation of the renormalization scale μ_R and factorization scale μ_F. Several scale choices are discussed and the dependence on the choice of scale is found to be comparable to the variation of the central value for the different scales. While no physical argument for an optimal scale is found, the invariant WH mass is used as a dynamical scale. This scale choice is also used by the LHC Higgs Cross Section Working Group in Ref. [29]. By performing the NLO calculation the scale dependence could be reduced significantly. In the case of W^+Hj the simultaneous variation of both μ_R and μ_F using a dynamical scale of $\mu_0 = m_{WH}$ in the interval $[0.5\mu_0, 2\mu_0]$ leads to a variation of the cross section which is reduced by a factor 3 from 19% at LO to 7% at NLO. For Wj production there is a cancellation between the μ_R and μ_F dependence, so that a simultaneous variation underestimates the scale dependencies. For WHj the renormalization scale dominates and therefore varying $\mu_R = \mu_F$ results in a reasonable estimate of the theoretical error. The scale dependence of WHj can be reproduced using Wj, by requiring the W boson to have an invariant mass above 200 GeV, which corresponds to the invariant mass of the W coupling to the quark line in WHj production.

A jet veto can be used to reduce the apparent scale dependence. However, this introduces large scale dependences in some differential distributions, such that the variation of the total cross section is no longer a reliable estimate of the theoretical error.

In WH production experimental analyses often use a boosted Higgs, this means a cut of $p_{Th} > 200$ GeV. This reduces the cross section, but improves the signal to background ratio. The K-factor of the total cross section is not affected by this cut, but several observables and differential K-factors change their shape significantly. This shows, that NLO calculations can not be approximated by multiplying a constant K-factor.

Anomalous couplings are implemented and their effect on the production of WHj is discussed. Both the total cross section and the shape of typical distributions like $p_{\mathrm{T}l}$ or $p_{\mathrm{T}h}$ are sensitive to modifications of the WWH vertex. The effect is most prominent in the high p_{T} region.

Based on the presented calculation several further analyses could be performed. The implementation of anomalous couplings allows to investigate whether WH and WHj could be used to set experimental limits on operators.

The calculations of WH and WHj production at NLO in QCD could be combined using the Loopsim method [61]. It allows to produce approximate NNLO results ($\bar{n}$NLO) for high-p_{T} observables in WH production. Similar combinations were recently performed for WW [62], WZ [63] and W/Z + jets [64]. This could then be compared to the full NNLO calculation of WH production [65] to study the validity of the merging tools.

CHAPTER 7

ZUSAMMENFASSUNG

Die Teilchenphysik untersucht die fundamentalen Bausteine des Universums und deren Wechselwirkung auf sehr kleinen Skalen. Das Standardmodell der Teilchenphysik (SM) ist eine in den 1960er und 70er Jahren entwickelte relativistische Quantenfeldtheorie. Seitdem wurde das Standardmodell erfolgreich verwendet, um sowohl Ergebnisse von Präzisionsexperimenten als auch die Entdeckung neuer Teilchen vorherzusagen. Solch ein neues Teilchen wurde erst kürzlich entdeckt. Die beobachtete Resonanz entspricht bisher dem SM Higgs Boson, wobei die Eigenschaften noch nicht vollständig gemessen sind. Das Teilchen wurde von ATLAS und CMS entdeckt, zwei Experimenten, die am Large Hadron Collider (LHC) am CERN in Genf angesiedelt sind. Der LHC ist der aktuelle Stand in einer historischen Reihe von Teilchenbeschleunigern. Er wurde gebaut, um neue Teilchen zu suchen und unser Verständnis von Teilchenphysik bei zuvor unerreichten Energien zu überprüfen. Designkriterium war nicht nur die Suche nach dem Higgs Boson, sondern auch die Untersuchung von Theorien jenseits des Standardmodells. Die Entdeckung des Higgs-ähnlichen Teilchens ist der Anfang einer neuen Generation von SM Präzisionsmessungen und möglichen Teilchenentdeckungen an der TeV Skala.

Obwohl das Standardmodell sehr erfolgreich ist, wissen wir heutzutage, dass es nicht in der Lage ist, alle Phänomene zu beschreiben, so beinhaltet das SM keine Neutrinomassen. Jedoch ist durch Messungen der Neutrinooszillation bekannt, dass Neutrinos Masse tragen. Diese lässt sich mit verschiedenen Mechanismen im SM integrieren. Im SM sind nahezu alle Massen freie Parameter deren Werte nicht vorhergesagt werden. Insbesondere den deutlichen Größenunterschied zwischen den verschiedenen Teilchengenerationen und die Spanne von Leptonen und Neutrinos zu den schweren Quarks und den Eichbosonen an der schwachen Skala erklärt das Standardmodell nicht. Des Weiteren gibt es Erkenntnisse der Astronomie, wie die Beobachtung von Dunkler Energie und Dunkler Materie, die nicht durch das SM beschrieben sind. Fundamentaler ist allerdings die Beschreibung von Gravitation durch die Allgemeine Relativitätstheorie. Diese ist sehr gut getestet und erlaubt die Beschreibung von Gravitationsphänomenen in unserem Sonnensystem und darüber hinaus. Bisher gelang jedoch keine erfolgreiche Formulierung einer Theorie, die die Allgemeine Relativitätstheorie mit dem Standardmodell kombiniert.

Das Standardmodell basiert auf der Eichsymmetrie $\mathrm{SU(3)_C} \times \mathrm{SU(2)_L} \times \mathrm{U(1)_Y}$, die sich in zwei Sektoren aufteilen lässt. Diese beiden Teile des SM werden oft anhand ihrer Kopplungen

durch α (elektroschwach) und α_s (stark) unterschieden. Die Gruppe $SU(3)_C$ beschreibt die Quantenchromodynamik (QCD), die Theorie der starken Wechselwirkung. Diese wirkt auf Teilchen mit Farbladung, den Quarks und Gluonen, aus denen Hadronen und somit Atomkerne aufgebaut sind. Die Gruppe $SU(2)_L \times U(1)_Y$ beschreibt den elektroschwachen Sektor. Die zu dieser Gruppe gehörigen Eichbosonen W und Z vermitteln die schwache Wechselwirkung. Diese ist zum Beispiel verantwortlich für den radioaktiven β-Zerfall von Atomkernen. Die Symmetriegruppe $SU(2)_L \times U(1)_Y$ des elektroschwachen Sektors wird durch spontane Symmetriebrechung vom Higgs Mechanismus zur Gruppe $U(1)_{em}$ gebrochen. Diese Gruppe beschreibt die Quantenelektrodynamik (QED) – die Wechselwirkung von geladenen Teilchen, die von Photonen übertragen wird. Der Higgs Mechanismus ist verantwortlich für die Masse der Eichbosonen und Fermionen.

Trotz der Fortschritte in Ansätzen wie Gitter QCD werden die meisten Vorhersagen für das SM in Störungstheorie berechnet. Dabei werden Observablen in den Kopplungskonstanten entwickelt. Der erste Term einer solchen Entwicklung wird als führende Ordnung (engl. leading order, LO) bezeichnet. Die folgenden Terme sind dann die nächst-führende Ordnung (next-to-leading order, NLO) und nächst-nächst-führende Ordnung (NNLO). Da α_s deutlich größer als α ist, wird diese Entwicklung häufig in α_s betrachtet. Eine Rechnung, die zusätzlich zum führenden Term noch einen weiteren in α_s berücksichtigt, nennt man NLO QCD.

Außer der direkten Suche nach neuen Teilchen und Wechselwirkungen, können mögliche Theorien jenseits des Standardmodells auch untersucht werden, indem Vorhersagen des Standardmodells mit experimentellen Daten verglichen werden und dadurch Grenzen an allgemeine Erweiterungen des SM gesetzt werden. Dies bedeutet für das neu gefundene Teilchen, dass die Vorhersagen des SM für das Higgs Boson im Hinblick auf die verschiedenen Produktions- und Zerfallsprozesse untersucht werden müssen.

Der wichtigste Produktionsprozess für das Higgs Boson im SM heißt Gluon Fusion. In diesem Prozess koppeln zwei Gluonen über eine Fermionschleife an das Higgs Boson. Der Prozess mit dem zweitgrößten Wirkungsquerschnitt ist Vektor Boson Fusion. In diesem sind im Endzustand neben dem Higgs Boson noch zwei Jets zu finden, die durch ihre spezielle Kinematik ein Filtern von Hintergrundereignissen erlauben. Darüber hinaus kann das Higgs Boson auch zusammen mit einem Vektor Boson oder schweren Quarks produziert werden. Die Produktion des Higgs Boson mit einem Vektor Boson (VH) heißt Higgsstrahlung. Dieser Name bezieht sich auf das Feynman Diagramm, bei dem das Higgs Boson von einem W oder Z „abgestrahlt“ wird.

Das Higgs Boson ist instabil und zerfällt nahezu sofort. Daher kann es nur durch Zerfallsprodukte beobachtet werden. Die verschiedenen Zerfallskanäle führen zu Endzuständen, die auch durch Prozesse ohne Higgs Beitrag erzeugt werden können. Diese nennt man Untergrund (engl. background) und ihre Wirkungsquerschnitte und Eigenschaften müssen genau bestimmt werden, um ein Filtern des Higgssignals aus dem Untergrund zu erlauben. Hierfür sind NLO QCD Rechnungen sowohl für Signal- als auch Untergrundprozesse erforderlich.

Diese Auswahl an Produktionsmechanismen und Zerfallsprozessen erlaubt die Kopplung des Higgs Boson an verschiedene SM Teilchen zu bestimmen. Da diese Kopplungen nicht frei sind, sondern von einer kleinen Zahl bekannter Parameter festgelegt werden, lassen sich somit mögliche Abweichungen vom SM mit hoher Präzision testen. Die Entdeckung des neuen Teilchens wurde in inklusiver Produktion ohne zusätzliche Teilchen zu fordern und im Zerfall in Photonen und über Z Bosonen in vier Leptonen entdeckt. Beide LHC Experimente untersuchen aber auch die Produktion in VH in Kombination mit dem Zerfall in zwei b Quarks [4, 5] oder

zwei W Bosonen [6]. Diese Kanäle haben bisher noch nicht ausreichend statistische Signifikanz, um eine Entdeckung zu vermelden, zeigen aber einen mit der SM Vorhersage kompatiblen Überschuss an Ereignissen. Higgsstrahlung wurde zudem bereits verwendet, um Modelle jenseits des SM zu testen [7]. Die bekannten NLO Korrekturen zu WH Produktion sind groß und erheblich vom Phasenraum abhängig und sind daher von Bedeutung für experimentelle Analysen. Viele der WH Ereignisse haben zusätzliche Jets, sodass ebenso die Korrekturen zu WHj Produktion wichtig sind.

In dieser Diplomarbeit wurden die NLO QCD Korrekturen zur Produktion von WHj, Higgsstrahlung mit einem zusätzlichen Jet, berechnet und in das flexible Monte Carlo Programm VBFNLO implementiert. Dieses bietet eine Vielzahl von Prozessen mit NLO QCD Korrekturen, unter anderem Vektor Boson Fusion sowie die Produktion von zwei oder drei Vektor Bosonen, in einigen Fällen auch mit einem oder zwei zusätzlichen Jets. VBFNLO nutzt Monte Carlo Integration zur Berechnung des Wirkungsquerschnitts. Um die Konvergenz zu beschleunigen wird der VEGAS Algorithmus verwendet, der die Generierung der Phasenraumpunkte während der Integration anpasst.

Die NLO Rechnung lässt sich in zwei Teile zerlegen, welche sich in der Dimension des zugehörigen Phasenraums unterscheiden. Die virtuellen Beiträge entsprechen dabei in ihrem Endzustand der führenden Ordnung, während die reellen Beiträge ein weiteres Parton aufweisen. Diese beiden Integrale sind getrennt divergent und nur in der Summe endlich, was eine direkte numerische Integration verhindert. Die Divergenzen können jedoch durch Regularisierung parametrisiert werden und es existieren verschiedene Verfahren um endliche Integrale zu konstruieren. In dieser Arbeit wurde das für NLO Monte Carlo Programme häufig verwendete Subtraktionsschema von Catani und Seymour verwendet [21]. Hierbei wird die reelle Emission um Subtraktionsterme erweitert, welche die Divergenzen wegheben. Zugleich sind diese Terme aber analytisch integrierbar, sodass sie in integrierter Form bei den virtuellen Korrekturen addiert werden können.

Neben WHj wurden auch die Produktion von W, WH und Wj mit NLO QCD Korrekturen implementiert. Diese Prozesse besitzen eine ähnliche QCD Struktur wie bereits implementierte Diboson- und Tribosonprozesse, sodass Teile der Rechnung unter anderem analog zu WA [37], WAAj [38] sowie WZj [39] durchgeführt werden konnten.

VBFNLO nutzt effektive Ströme zur Implementierung. Dabei werden zunächst die elektroschwachen Bestandteile eines Diagramms berechnet und als effektiver Polarisationsvektor beziehungsweise leptonischer Tensor geschrieben. Dieser wird an das restliche aus QCD Wechselwirkungen bestehende Diagramm gekoppelt. Diese Trennung ist effizient, da in der NLO Rechnung eine geringe Zahl elektroschwacher Ströme an diverse QCD Diagramme gekoppelt werden und nicht jedes Mal erneut zu berechnen sind. Zudem können Erweiterungen im elektroschwachen Bereich, z.B. der Zerfall des Higgs Boson oder anomale Kopplungen, unabhängig von der QCD Rechnung durchgeführt werden. Andererseits lassen sich auf LO genutzte und überprüfte leptonische Tensoren auch in NLO QCD Rechnungen verwenden.

In der vorliegenden Berechnung von WHj wurden leptonische Zerfälle des W und Zerfälle des Higgs Boson in $b\bar{b}$, $\gamma\gamma$, $\tau\bar{\tau}$, $\mu\bar{\mu}$, WW $\to l\nu\, l\nu$, ZZ $\to ll\, ll$ und $ZZ \to ll\, \nu\nu$ implementiert. Die Higgs Zerfälle lassen sich faktorisieren und wurden aus der Berechnung von Higgsproduktion in VBF übernommen, wobei die Zerfälle in vier Leptonen mit Matrixelementen und somit mit Spinkorrelationen berechnet werden.

Die NLO Rechnung beinhaltet bei den virtuellen Korrekturen Schleifendiagramme, welche neben Vertex- und Selbstenergiekorrekturen auch Box-Diagramme umfassen. Sie wurden mit

der Boxline Routine aus Ref. [44] berechnet und treten auch bei Wj Produktion auf. Bei WHj Produktion gibt es weitere (nicht bei Wj Produktion existierende) Diagramme, bei denen das Higgs Boson nicht an ein W, sondern an eine Top-Quark-Schleife, koppelt. Diese Diagramme wurden mit der vollen m_t Abhängigkeit mit den Routinen aus Ref. [45] berechnet.

Die reellen Emissionen von WHj beinhalten zwei Arten von Diagrammen. Der Typ *ggqq* hat eine Quarklinie mit zwei zusätzlichen Gluonen. Da diese Gluonen beide im Anfangszustand sein können, ergibt sich eine Verstärkung durch die großen Gluon PDFs. Der zweite Diagrammtyp *qqqq* beinhaltet zwei Quarklinien, sodass alle externen Partonen Quarks sind. Die Subtraktionsterme wurden als Teil der reellen Emissionen implementiert.

Im Rahmen der Rechnung wurde die CKM Matrix betrachtet, die bei der Kopplung eines W an Quarks den Übergang zwischen verschiedenen Quarkgenerationen erlaubt. Da die Matrix nahezu diagonal ist, stellen diese generationenändernden Kopplungen nur kleine Korrekturen dar und häufig wird die CKM Matrix als Einheitsmatrix angenähert, so zum Beispiel in den bisher in VBFNLO implementierten Produktionsprozessen. Dies hat den Vorteil, dass für die Berechnung des Matrixelements keine Informationen über den Flavour der Quarks nötig sind. Mit den aktuell experimentell bekannten Werten für die CKM Matrix ist die Mischung zwischen den ersten beiden Generationen deutlich größer als die Mischung mit der dritten Generation. Daher werden nur Effekte der Mischung in den ersten beiden Generationen berücksichtigt.

Nicht-diagonale Matrixelemente lassen sich in eine Berechnung, die von einer diagonalen CKM Matrix ausgeht, integrieren, ohne der eigentlichen Matrixelementberechnung Flavourinformationen zu geben. Stattdessen werden CKM Matrix Einträge in die PDFs gezogen und dort die Quarkbasis rotiert. Der numerische Effekt von Übergängen in den ersten zwei Generationen lässt sich durch die PDFs ausdrücken, sodass die relative Änderung des Wirkungsquerschnitts kleiner ist als $\sin^2\theta_c\,(u-c)\,(\overline{d}-\overline{s})$. Der Vorfaktor $\sin^2\theta_c$ beträgt etwa 5% und stellt ein oberes Limit an den Effekt dar. Für die Produktion von W, WH, Wj und WHj wurden Wirkungsquerschnittsänderungen von etwas unter 1% gefunden, die auch in differentiellen Wirkungsquerschnitten nur in extremen Phasenraumbereichen deutlich größer sind.

Die NLO QCD Rechnung wurde sowohl mit vier als auch fünf aktiven Flavours ausgeführt. Die Zahl der aktiven Flavour wird in verschiedenen Teilen der Rechnung genutzt um zu beschreiben, welche Quark Flavour einbezogen werden. Da die verschiedenen Terme der NLO Rechnung untereinander abhängig sind, muss diese Zahl konsistent gewählt werden. Inbesondere sind virtuelle und reelle Korrekturen miteinander verknüpft. Es gibt bevorzugte Flavour Anzahlen in bestimmten Prozessen. Eine Rechnung mit allen Ordnungen der Störungstheorie sollte zu identischen Ergebnissen führen, sodass Abweichungen hier einem Theoriefehler entsprechen. Diese Abweichungen betragen im Falle von WHj Produktion wenige Prozent.

Die Rechnung wurde auf mehrere Weisen auf ihre Richtigkeit hin überprüft. Die LO Amplitude wurde mit MadGraph verglichen, der LO Wirkungsquerschnitt mit Sherpa. Für die virtuellen Amplituden wurden interne Überprüfungen basierend auf Ward Identitäten sowie anhand bekannter analytischer Ergebnisse durchgeführt. Die Top-Quark-Schleifen liefern in verschiedenen Grenzwerten Übereinstimmung mit effektiven Vertices aus MadGraph. Zum Gesamtwirkungsquerschnitt tragen die Top-Quark-Schleifen 2-3% bei. Der NLO Wirkungsquerschnitt für die Produktion von WH und Wj wurde mit MCFM überprüft. Die Implementierung der CKM Matrix ergibt Übereinstimmung mit den Implementierungen in MCFM und Sherpa.

Der Vergleich mit einer vorherigen Berechnung von Ji-Juan et al. in Ref. [49] von WHj Produktion auf NLO QCD mit W und Higgs Boson auf der Massenschale zeigt Abweichungen

im Bereich einiger Prozent. Für bestimmte Parameterwahlen treten Unterschiede bereits auf LO auf. Des Weiteren zeigen die Abweichungen im Vergleich eine Skalenabhängigkeit. Die Skalenvariation von WHj Produktion wurde zusammen mit Wj Produktion ausführlich diskutiert und bestätigt. Die in dieser Arbeit durchgeführte Berechnung von WHj Produktion differiert nur in wenigen Teilen von Wj Produktion und wurde in diesen Aspekten explizit überprüft, sodass das Ergebnis abgesichert ist. Vor kurzem wurde eine weitere NLO QCD Rechnung von VHj veröffentlicht in Ref. [60], aber die Ergebnisse konnten noch nicht verglichen werden.

Basierend auf dieser Rechnung wurden verschiedene Aspekte der Phänomenologie untersucht. Für den Wirkungsquerschnitt von W^+Hj ergeben sich auf LO 25.3 fb und auf NLO 28.8 fb. Für W^-Hj ist der Wirkungsquerschnitt aufgrund der in einer anderen Kombination auftretenden PDFs geringer mit 14.5 fb auf LO und 16.7 fb auf NLO. Der K-Faktor, das Verhältnis von NLO zu LO, ist damit für den Gesamtwirkungsquerschnitt 1.13 bzw. 1.15. Für die weitere Diskussion wird exemplarisch W^+Hj verwendet. Die Top-Quark-Schleifen auf NLO tragen 2-3% zum Wirkungsquerschnitt bei. Dieser Beitrag hängt nur unwesentlich vom Phasenraum ab.

Der Theoriefehler wird üblicherweise durch die Skalenabhängigkeit abgeschätzt. Hierzu werden die in der Rechnung auftretende Renormierungsskala μ_R und Faktorisierungsskala μ_F um einen zentralen Wert variiert. Diese Skalenabhängigkeit würde bei einer Rechnung mit allen Ordnungen der Störungstheorie verschwinden. Die gewählte Skala sollte repräsentativ für den Prozess sein. Klassisch ist die Nutzung einer konstanten Skala, für WHj zum Beispiel die Masse des Z Boson, welche zwischen der von Masse von W und Higgs Boson liegt. Es ist jedoch besser eine dynamische Skala zu verwenden, die phasenraumabhängig ist. Diverse mögliche Skalen wurden untersucht, wobei sich die Abhängigkeit von der Definition der Skala von der gleichen Größenordnung wie die Skalenvariation ergab. Eine geeignete Wahl in Bezug auf WHj Produktion, die auch von der LHC Higgs Cross Section Working Group in Ref. [29] verwendet wird, ist die invariante Masse m_{WH} des WH Systems. Skalen, die nur auf Partonen basieren, sind tendenziell klein und führen bei zusätzlicher Variation zu starken Abweichungen.

Für W^+Hj Produktion hat eine gemeinsame Skalenvariation von μ_F und μ_R im Bereich $[0.5\mu_0, 2\mu_0]$ um $\mu_0 = m_{WH}$ einen Einfluss auf den Wirkungsquerschnitt von 19% auf LO und 7% auf NLO. Die NLO Korrekturen reduzieren also die Skalenabhängigkeit um einen Faktor 3. Bei Wj Produktion weisen μ_R und μ_F auf LO entgegengesetztes Verhalten auf. Daher unterschätzt eine Skalenvariation, die beide Skalen gemeinsam variiert, die Skalenabhängigkeit deutlich und ist keine geeignete Abschätzung für den Theoriefehler. Bei WHj Produktion dominiert die Abhängigkeit von μ_R, sodass eine gemeinsame Variation adäquat ist. Das Skalenverhalten von WHj Produktion lässt sich mit Wj Produktion reproduzieren, indem die invariante Masse des W zu Werten oberhalb von 200 GeV gezwungen wird. Bei WHj Produktion koppelt ein W Boson an die Quarklinie, dessen invariante Masse der des WH Systems entspricht. Damit ist das W weit von seiner Massenschale entfernt und die Skalenvariation zeigt ein qualitativ ähnliches Verhalten wie für WHj.

Ein *Jet Veto* ist ein Phasenraumschnitt, der auf NLO Ereignisse mit einem zusätzlichen Jet über einer gewissen Grenze $p_{T\,veto}$ verwirft und dabei scheinbar die Skalenabhängigkeit reduziert. Dies senkt den Wirkungsquerschnitt und beeinflusst die Form differentieller Wirkungsquerschnitte. Insbesondere im Bereich hoher Transversalimpulse ist der Wirkungsquerschnitt reduziert. Die Verringerung der Skalenvariation entspricht nicht einem reduzierten Theoriefehler. Im Gegenteil gibt es Verteilungen, die mit Jet Veto eine hohe Skalenabhängigkeit aufweisen, sodass hier eine konservativere Abschätzung der Unsicherheiten basierend auf der

Skalenvariation der inklusiven Rechnung nötig ist.

Experimentelle Analysen der Produktion in Higgsstrahlung suchen häufig nach geboosteten Higgs Kandidaten. Kriterium hierfür ist typischerweise $p_{\mathrm{T}h} > 200\,\mathrm{GeV}$. Obwohl dieser Phasenraumschnitt den Wirkungsquerschnitt des Signals reduziert, hat er einen größeren Effekt auf Untergrundprozesse wie W+Jets und erhöht so den Anteil von Signal- zu Untergrundereignissen. Während der K-Faktor des totalen Wirkungsquerschnitts ähnlich bleibt, ändern sich die differentiellen K-Faktoren mit diesem zusätzlichen Phasenraumschnitt deutlich. Dies zeigt, dass NLO Rechnungen, insbesondere bei der Suche nach einem boosted Higgs, nicht durch die Multiplikation mit einem konstanten K-Faktor approximiert werden können.

Anomale Kopplungen sind eine Erweiterung des Standardmodells, die in Form einer effektiven Feldtheorie allgemeine Kopplungen von Eichbosonen parametrisieren. Diese können als Niederenergie-Grenzwert einer unbekannten Theorie bei einer höheren Energieskala interpretiert werden. In WHj Produktion sind anomale Kopplungen mit ihren Effekten auf den WWH Vertex implementiert. Anomale Kopplungen beeinflussen sowohl den totalen Wirkungsquerschnitt als auch die Form von Verteilungen. Starke Effekte zeigen sich vor allem im Bereich großer Transversalimpulse.

Basierend auf dieser Berechnung ergeben sich weitere Forschungsmöglichkeiten. So können Sensitivitätsanalysen mit anomalen Kopplungen durchgeführt werden, um eine mögliche Einschränkung der Parameterwahl durch die Messungen von WH(j) Produktion zu untersuchen.

Die Berechnungen der Produktion WH und WHj auf NLO können mit der Loopsim Methode [61] kombiniert werden. Dies ermöglicht die Bestimmung angenäherter NNLO Ergebnisse ($\bar{n}$NLO) für Observablen im Bereich hoher Transversalimpulse. Ähnliche Kombinationen wurden bereits für WW [62], WZ [63] und W/Z + Jets [64] durchgeführt. Ein Vergleich mit der vollen NNLO Rechnung [65] kann genutzt werden, um die Kombinationsmethode und ihren möglichen Anwendungsbereich zu untersuchen.

ACKNOWLEDGEMENTS

First and foremost I would like to thank Prof. Zeppenfeld for offering me the chance to work on this interesting and current research topic. His many helpful suggestions constitute an essential part of this thesis. Additionally, I would like to thank for the opportunity to attend the DPG Tagung in Dresden and the MCNet school in Göttingen.

I would also like to thank Prof. Steinhauser for agreeing to be the second referee of my thesis.

My special thanks go to Francisco Campanario (Paco) for his helpful explanations and endurance in discussing all aspects from technical details to the big picture. Without his extraordinary commitment this thesis would not have been possible.

In addition, I would like to thank all members of the institute for their support during the last year, in particular my fellow diploma and master students.

My thanks goes to those who proofread this thesis, especially Hanna Hoffmann and Matthias Kerner.

I would like to thank my mother, sister and girlfriend for their support throughout my studies and this thesis.

APPENDIX

A. Physical Constants

The following values for physical constants are used if not explicitly stated otherwise. Where applicable, they follow the defaults in VBFNLO.

$$\begin{array}{lll} G_\mathrm{F} = 1.16637 \cdot 10^{-5} & m_\mathrm{top} = 172.4\,\mathrm{GeV} & \sin\theta_\mathrm{W} = 0.222646 \\ m_\mathrm{h} = 126\,\mathrm{GeV} & \Gamma_\mathrm{h} = 0.00427651\,\mathrm{GeV} & \sin^2\theta_\mathrm{cabibbo} = 0.22535 \\ m_\mathrm{W} = 80.398\,\mathrm{GeV} & \Gamma_\mathrm{W} = 2.09767297\,\mathrm{GeV} & \mathrm{BR}(\mathrm{H} \to \mathrm{b\bar{b}}) = 57.1\% \\ m_\mathrm{Z} = 91.1876\,\mathrm{GeV} & \Gamma_\mathrm{Z} = 2.50841993\,\mathrm{GeV} & \mathrm{BR}(\mathrm{W} \to l\nu) = 10.84\% \end{array} \tag{7.1}$$

If not stated otherwise, for all LO calculations the PDF set CTEQ6L1 and for NLO calculations CT10 is used [27, 28]. The value of α_s is taken from the corresponding PDF set.

BIBLIOGRAPHY

[1] **ATLAS Collaboration**, G. Aad, *et al.*, "Observation of a new particle in the search for the Standard Model Higgs boson with the ATLAS detector at the LHC," *Physics Letters B* **716** no. 1, (Sept., 2012) 1–29, arXiv:1207.7214.

[2] **CMS Collaboration**, S. Chatrchyan, *et al.*, "Observation of a new boson at a mass of 125 GeV with the CMS experiment at the LHC," *Physics Letters B* **716** no. 1, (Sept., 2012) 30–61, arXiv:1207.7235.

[3] K. Hagiwara, S. Ishihara, R. Szalapski, and D. Zeppenfeld, "Low energy effects of new interactions in the electroweak boson sector.," *Physical Review D* **48** no. 5, (Sept., 1993) 2182–2203.

[4] **CMS Collaboration**, "Search for the standard model Higgs boson produced in association with W or Z bosons, and decaying to bottom quarks for LHCp 2013," Tech. Rep. CMS-PAS-HIG-13-012, CERN, Geneva, 2013.

[5] **ATLAS Collaboration**, "Search for the bb decay of the Standard Model Higgs boson in associated W/ZH production with the ATLAS detector," Tech. Rep. ATLAS-CONF-2013-079, CERN, Geneva, Jul, 2013.

[6] **CMS Collaboration**, "VH with H→WW→ $\ell\nu\ell\nu$ and V→jj," Tech. Rep. CMS-PAS-HIG-13-017, CERN, Geneva, 2013.

[7] **ATLAS Collaboration**, G. Aad, *et al.*, "Search for WH production with a light Higgs boson decaying to prompt electron-jets in proton–proton collisions at $\sqrt{s} = 7\,\text{TeV}$ with the ATLAS detector," *New Journal of Physics* **15** no. 4, (Apr., 2013) 043009, arXiv:arXiv:1302.4403v1.

[8] M. E. Peskin and D. V. Schroeder, *An Introduction To Quantum Field Theory*. Westview Press, 1995.

[9] S. L. Glashow, "Partial-symmetries of weak interactions," *Nuclear Physics* **22** no. 4, (Feb., 1961) 579–588.

[10] S. Weinberg, "A Model of Leptons," *Physical Review Letters* **19** no. 21, (Nov., 1967) 1264–1266.

[11] A. Salam and J. C. Ward, "Weak and electromagnetic interactions," *Il Nuovo Cimento* **11** no. 4, (Feb., 1959) 568–577.

[12] P. Higgs, "Broken Symmetries and the Masses of Gauge Bosons," *Physical Review Letters* **13** no. 16, (Oct., 1964) 508–509.

[13] P. Higgs, "Broken symmetries, massless particles and gauge fields," *Physics Letters* **12** no. 2, (1964) 132–133.

[14] F. Englert and R. Brout, "Broken Symmetry and the Mass of Gauge Vector Mesons," *Physical Review Letters* **13** no. 9, (Aug., 1964) 321–323.

[15] F. L. Wilson, "Fermi's Theory of Beta Decay," *American Journal of Physics* **36** no. 12, (July, 1968) 1150.

[16] D. Chitwood, *et al.*, "Improved Measurement of the Positive-Muon Lifetime and Determination of the Fermi Constant," *Physical Review Letters* **99** no. 3, (July, 2007) 032001.

[17] W. Buchmüller and D. Wyler, "Effective lagrangian analysis of new interactions and flavour conservation," *Nuclear Physics B* **268** no. 3, (1986) 621–653.

[18] O. Schlimpert, *Anomale Kopplungen bei der Streuung schwacher Eichbosonen.* Diplomarbeit, KIT, 2013.

[19] T. D. Lee and M. Nauenberg, "Degenerate systems and mass singularities," *Phys. Rev.* **133** (Mar, 1964) B1549–B1562.

[20] T. Kinoshita, "Mass singularities of feynman amplitudes," *Journal of Mathematical Physics* **3** no. 4, (1962) 650–677.

[21] S. Catani and M. H. Seymour, "A General Algorithm for Calculating Jet Cross Sections in NLO QCD," *Nuclear Physics B* **0357** (May, 1996) 120, `arXiv:9605323 [hep-ph]`.

[22] S. Catani and M. H. Seymour, "Jet cross sections at next-to-leading order," *Acta Phys.Polon.* **B28** (Dec., 1997) 863–881, `arXiv:9612236 [hep-ph]`.

[23] Y. Alexahin, *et al.*, "The Case for a Muon Collider Higgs Factory," `arXiv:1307.6129`.

[24] G. Altarelli and G. Parisi, "Asymptotic Freedom in Parton Language," *Nucl.Phys.* **B126** (1977) 298.

[25] Y. L. Dokshitzer, "Calculation of the Structure Functions for Deep Inelastic Scattering and e+ e- Annihilation by Perturbation Theory in Quantum Chromodynamics.," *Sov.Phys.JETP* **46** (1977) 641–653.

[26] V. Gribov and L. Lipatov, "Deep inelastic e p scattering in perturbation theory," *Sov.J.Nucl.Phys.* **15** (1972) 438–450.

[27] J. Pumplin, *et al.*, "New generation of parton distributions with uncertainties from global QCD analysis," *JHEP* **0207** (2002) 012, `arXiv:hep-ph/0201195`.

[28] H.-L. Lai, *et al.*, "New parton distributions for collider physics," *Phys.Rev.* **D82** (2010) 074024, `arXiv:1007.2241`.

[29] LHC Higgs Cross Section Working Group, S. Heinemeyer, C. Mariotti, G. Passarino, and R. Tanaka (Eds.), "Handbook of LHC Higgs Cross Sections: 3. Higgs Properties," *CERN-2013-004* (CERN, Geneva, 2013) , arXiv:1307.1347 [hep-ph].

[30] LHC Higgs Cross Section Working Group, S. Dittmaier, C. Mariotti, G. Passarino, and R. Tanaka (Eds.), "Handbook of LHC Higgs Cross Sections: 1. Inclusive Observables," *CERN-2011-002* (CERN, Geneva, 2011) , arXiv:1101.0593 [hep-ph].

[31] J. M. Butterworth, A. R. Davison, M. Rubin, and G. P. Salam, "Jet substructure as a new Higgs search channel at the LHC," *Physical Review Letters* **100** no. 24, (Feb., 2008) 4, arXiv:0802.2470.

[32] S. Weinzierl, "Introduction to Monte Carlo methods," arXiv:0006269 [hep-ph].

[33] G. Peter Lepage, "A new algorithm for adaptive multidimensional integration," *Journal of Computational Physics* **27** no. 2, (May, 1978) 192–203.

[34] G. P. C. U. Lepage, "VEGAS: An Adaptive Multi-dimensional Integration Program," *Cornell Preprint* no. CLNS-80/447, (1980) 30.

[35] K. Arnold, *et al.*, "Release Note – Vbfnlo-2.6.0," arXiv:1207.4975.

[36] K. Arnold, *et al.*, "Vbfnlo: A parton level Monte Carlo for processes with electroweak bosons," *Computer Physics Communications* **180** no. 9, (Sept., 2009) 1661–1670.

[37] J. Bellm, *NLO-QCD-Korrekturen zur WZ- und Wγ-Produktion am LHC*. Diplomarbeit, KIT, 2012.

[38] F. Campanario, C. Englert, M. Rauch, and D. Zeppenfeld, "Precise predictions for jet production at hadron colliders," *Physics Letters B* **704** no. 5, (Oct., 2011) 515–519, arXiv:1106.4009.

[39] C. Englert, *Next-to-Leading Order Corrections to W γ + jet and W Z + jet Production at Hadron Colliders*. Phd thesis, KIT, 2010.

[40] K. Hagiwara and D. Zeppenfeld, "Amplitudes for multi-parton processes involving a current at e+e−, e±p, and hadron colliders," *Nuclear Physics B* **313** no. 3, (Feb., 1989) 560–594.

[41] H. Murayama, K. Hagiwara, and I. Watanabe, "HELAS: HELicity amplitude subroutines for Feynman diagram evaluations," *KEK Report* **11** (1992) .

[42] J. Alwall, *et al.*, "MadGraph/MadEvent v4: The New Web Generation," *Journal of High Energy Physics* **2007** no. 09, (June, 2007) 028–028, arXiv:0706.2334.

[43] W. Beenakker, *et al.*, "NLO QCD corrections to t anti-t H production in hadron collisions," *Nuclear Physics B* **653** no. 1-2, (Nov., 2002) 50, arXiv:0211352 [hep-ph].

[44] F. Campanario, "Towards pp → VVjj at NLO QCD: Bosonic contributions to triple vector boson production plus jet," *Journal of High Energy Physics* (May, 2011) 48, arXiv:1105.0920.

[45] F. Campanario, Q. Li, M. Rauch, and M. Spira, "ZZ+jet production via gluon fusion at the LHC," *Journal of High Energy Physics* **2013** no. 6, (Nov., 2012) 13, arXiv:1211.5429.

[46] L. Wolfenstein, "Parametrization of the Kobayashi-Maskawa Matrix," *Physical Review Letters* **51** no. 21, (Nov., 1983) 1945–1947.

[47] K. Nakamura, "Review of Particle Physics," *Journal of Physics G: Nuclear and Particle Physics* **37** no. 7A, (July, 2010) 075021.

[48] S. Dittmaier, S. Kallweit, and P. Uwer, "NLO QCD corrections to pp/$\bar{p}$p→WW+jet+X including leptonic W-boson decays," *Nuclear Physics B* **826** no. 1-2, (Feb., 2010) 18–70, arXiv:0908.4124.

[49] S. Ji-Juan, M. Wen-Gan, Z. Ren-You, and G. Lei, "Next-to-leading order QCD predictions for the hadronic WH+jet production," *Physical Review D* **81** no. 11, (June, 2010) 26, arXiv:1006.0279.

[50] F. Maltoni, G. Ridolfi, and M. Ubiali, "b-Initiated processes at the LHC: a reappraisal," *JHEP* **1207** (Mar., 2012) 022, arXiv:1203.6393.

[51] R. Frederix, E. Re, and P. Torrielli, "Single-top t-channel hadroproduction in the four-flavour scheme with POWHEG and aMC@NLO," *Journal of High Energy Physics* **2012** no. 9, (July, 2012) 130, arXiv:1207.5391.

[52] R. Harlander, M. Kramer, M. Schumacher, and M. Krämer, "Bottom-quark associated Higgs-boson production: reconciling the four- and five-flavour scheme approach," arXiv:1112.3478.

[53] A. Martin, W. Stirling, R. Thorne, and G. Watt, "Parton distributions for the LHC," *Eur.Phys.J.* **C63** (2009) 189–285, arXiv:0901.0002 [hep-ph].

[54] T. Gleisberg, *et al.*, "Event generation with SHERPA 1.1," *Journal of High Energy Physics* **2009** no. 02, (Nov., 2008) 007–007, arXiv:0811.4622.

[55] F. Campanario, M. Kerner, L. D. Ninh, and D. Zeppenfeld, "WZ production in association with two jets at NLO in QCD," *Physical Review Letters* **111** no. 5, (May, 2013) 4, arXiv:1305.1623.

[56] J. Campbell and R. K. Ellis, "Next-to-leading order corrections to W+2 jet and Z+2 jet production at hadron colliders," *Physical Review D* **65** no. 11, (June, 2002) 113007, arXiv:0202176 [hep-ph].

[57] O. Brein, R. V. Harlander, and T. J. E. Zirke, "vh@nnlo - Higgs Strahlung at hadron colliders," *Computer Physics Communications* **184** no. 3, (Oct., 2012) 16, arXiv:1210.5347.

[58] R. Hamberg, W. van Neerven, and T. Matsuura, "A complete calculation of the order α_s^2 correction to the Drell-Yan K-factor," *Nuclear Physics B* **359** no. 2-3, (Aug., 1991) 343–405.

[59] I. W. Stewart and F. J. Tackmann, "Theory uncertainties for Higgs mass and other searches using jet bins," *Physical Review D* **85** no. 3, (Feb., 2012) 034011, arXiv:1107.2117.

[60] G. Luisoni, P. Nason, C. Oleari, and F. Tramontano, "Merging HW/HZ + 0 and 1 jet at NLO with no merging scale using the POWHEG BOX interfaced to GoSam," arXiv:1306.2542.

[61] M. Rubin, G. P. Salam, and S. Sapeta, "Giant QCD K-factors beyond NLO," *Journal of High Energy Physics* **2010** no. 9, (June, 2010) 38, arXiv:1006.2144.

[62] F. Campanario, M. Rauch, and S. Sapeta, "WW production at high transverse momenta beyond NLO," arXiv:1309.7293.

[63] S. Sapeta, "WZ and W+jets production at large transverse momenta beyond NLO," arXiv:1305.6531.

[64] D. Maître and S. Sapeta, "Simulated NNLO for high-pT observables in vector boson + jets production at the LHC," arXiv:1307.2252.

[65] G. Ferrera, M. Grazzini, and F. Tramontano, "Associated Higgs-W-Boson Production at Hadron Colliders: A Fully Exclusive QCD Calculation at NNLO," *Physical review letters* **107** no. July, (July, 2011) 7, arXiv:1107.1164.